

Polarization Observables in Virtual Compton Scattering

DISSERTATION

zur Erlangung des Grades “Doktor der Naturwissenschaften”

am Fachbereich Physik, Mathematik und Informatik
der Johannes Gutenberg-Universität Mainz

vorgelegt von

Luca Doria
geboren in Bolzano (Bozen), Italien

Institut für Kernphysik
Johannes Gutenberg-Universität Mainz
October 2007

In the memory of my father.

Zusammenfassung

Virtuelle Compton-Streuung (VCS) ist ein wichtiger Prozess, um die Struktur des Nukleons bei niedrigen Energien zu untersuchen. Über diesen Zugang können die Generalisierten Polarisierbarkeiten gemessen werden. Diese Observablen sind die Verallgemeinerung der schon bekannten Polarisierbarkeiten des Nukleons und stellen eine Herausforderung an theoretische Modelle auf bislang unerreichter Ebene dar. Genauer gesagt gibt es sechs Generalisierte Polarisierbarkeiten. Um sie alle separat zu bestimmen, benötigt man ein Doppelpolarisationsexperiment.

Im Rahmen dieser Arbeit wurde die VCS-Reaktion $p(e,e'p)\gamma$ am MAMI mit der Dreispektrometeranlage bei $Q^2 = 0.33 \text{ (GeV}/c)^2$ gemessen. Mit einem hochpolarisierten Strahl und dem Rückstossprotonen-Polarimeter war es möglich, sowohl den Wirkungsquerschnitt der Virtuellen Compton-Streuung als auch die Doppelpolarisationsobservablen zu bestimmen. Bereits im Jahre 2000 wurde der unpolarisierte VCS-Wirkungsquerschnitt am MAMI vermessen. Diese Daten konnten mit dem neuen Experiment bestätigt werden. Die Doppelpolarisationsobservablen hingegen wurden hier zum ersten Mal gemessen.

Die Datennahme fand in fünf Strahlzeiten in den Jahren 2005 und 2006 statt. In der hier vorliegenden Arbeit wurden diese Daten ausgewertet, um den Wirkungsquerschnitt und die Doppelpolarisationsobservablen zu bestimmen.

Für die Analyse wurde ein Maximum-Likelihood-Algorithmus entwickelt, ebenso eine Simulation der gesamten Analyseschritte. Das Experiment ist wegen der geringen Effizienz des Protonpolarimeters von der Statistik begrenzt. Um über dieses Problem hinwegzukommen, wurde eine neue Messung und Parametrisierung der Analysierstärke von Kohlenstoff durchgeführt. Das Hauptergebnis dieses Experiments ist eine neue Linearkombination der Generalisierten Polarisierbarkeiten.

Abstract

Virtual Compton Scattering (VCS) is an important reaction for understanding nucleon structure at low energies. By studying this process, the generalized polarizabilities of the nucleon can be measured. These observables are a generalization of the already known polarizabilities and will permit theoretical models to be challenged on a new level. More specifically, there exist six generalized polarizabilities and in order to disentangle them all, a double polarization experiment must be performed.

Within this work, the VCS reaction $p(e,e'p)\gamma$ was measured at MAMI using the A1 Collaboration three spectrometer setup with $Q^2 = 0.33 \text{ (GeV/c)}^2$. Using the highly polarized MAMI beam and a recoil proton polarimeter, it was possible to measure both the VCS cross section and the double polarization observables.

Already in 2000, the unpolarized VCS cross section was measured at MAMI. In this new experiment, we could confirm the old data and furthermore the double polarization observables were measured for the first time.

The data were taken in five periods between 2005 and 2006. In this work, the data were analyzed to extract the cross section and the proton polarization. For the analysis, a maximum likelihood algorithm was developed together with the full simulation of all the analysis steps.

The experiment is limited by the low statistics due mainly to the focal plane proton polarimeter efficiency. To overcome this problem, a new determination and parameterization of the carbon analyzing power was performed. The main result of the experiment is the extraction of a new combination of the generalized polarizabilities using the double polarization observables.

Contents

1. Introduction	1
2. Theoretical Foundations	5
2.1 Motivation	5
2.2 Classical Polarizability	6
2.3 Quantum Polarizability	7
2.4 Real Compton Scattering	8
2.5 Virtual Compton Scattering	10
2.5.1 Definition of the Kinematics	11
2.5.2 Contributions to the Photon Electroproduction Process	12
2.6 Low Energy Expansion	14
2.7 Generalized Polarizabilities	16
2.8 Observables in Virtual Compton Scattering	18
2.8.1 Structure Functions	18
2.8.2 Observables	19
3. Theoretical and Experimental Status	23
3.1 Theoretical Models and Predictions	23
3.1.1 Non Relativistic Quark Model	23
3.1.2 Linear σ -Model	24
3.1.3 Heavy Baryon Chiral Perturbation Theory	25
3.1.4 Effective Lagrangian Model	25
3.1.5 Dispersion Relation Model	26
3.2 Summary on the Theoretical Predictions	28
3.3 Present Experimental Status	29
3.3.1 Unpolarized Virtual Compton Scattering	29
3.3.2 Single Spin Asymmetry	32
3.4 Summary on the Experimental Status	35
4. Accelerator and Experimental Setup	37
4.1 Accelerator	37
4.2 Experimental Setup	39
4.2.1 Magnetic Spectrometers	39
4.2.2 Target	42
4.2.3 Proton Polarimeter	43
4.2.4 Møller Polarimeter	46
4.2.5 Trigger and Data Acquisition	48
5. Measurement of the Proton Polarization	49
5.1 Spin Precession in a Magnetic Spectrometer	49
5.2 Spin Backtracking in Spectrometer A	52
5.3 Calculation of the Polarization	54
5.3.1 Maximum Likelihood algorithm: Introduction	54
5.3.2 Maximum Likelihood algorithm: Implementation	56

5.4	Extension to the Generalized Polarizabilities	58
5.5	Summary	58
6.	Simulation	59
6.1	Overview of the Simulation	59
6.2	Simulation of the Proton Polarization	60
6.2.1	Analyzing power sampling	61
6.2.2	Statistical Errors and Correlations	61
6.3	Simulation of Virtual Compton Scattering Polarizations	63
6.4	Correction of the P_y Polarization Component	65
6.5	Summary	70
7.	Data Analysis: Unpolarized Cross Section	71
7.1	Introduction	71
7.2	Kinematical Setups	71
7.3	Cross Section Determination	72
7.4	Particle Identification	74
7.5	Reaction Identification	75
7.6	Target Walls	75
7.7	Background Estimation	76
7.8	VCS Cross Section	77
7.9	Results	80
7.10	Systematic Errors	82
7.11	Summary	85
8.	Data Analysis: Double Polarization Observables	87
8.1	Introduction	87
8.2	Measurement of the Carbon Analyzing Power	87
8.3	Analysis of the Polarimeter Events	92
8.4	False Asymmetries	94
8.5	Polarization of the Background	95
8.6	Beam Polarization	96
8.7	Influence of the Beam Polarization on the Proton Polarization	96
8.8	Proton Polarization	98
8.9	Extraction of the Generalized Polarizabilities	104
8.10	Extraction of the Structure Functions	105
8.11	Extraction of the Structure Function P_{LT}^\perp	107
8.12	Systematical Errors	107
8.13	Separation of P_{LL} and P_{TT}	108
8.14	Summary	109
9.	Conclusions	111

Appendices

A.	Nucleon Form Factors	113
A.1	Bethe-Heitler + Born Cross Section and Form Factors Dependence	115

B. Maximum Likelihood Method	117
B.1 Definition of the Method	117
B.2 Properties of the Estimators	118
B.3 Asymptotic Properties	118
B.4 Covariance Matrix	119
C. Kinematics	121
C.1 Kinematical Coefficients for the Unpolarized Cross Section	121
C.2 Kinematical Coefficients for the Double Polarization Observable	122
C.3 Lorentz Transformations	122
D. Tables	125
D.1 Cross Section Data	125
D.2 Rosenbluth Separation Data	126
List of Figures	127
List of Tables	129
Bibliography	130

Chapter 1

Introduction

Fatti non foste a viver come bruti ,
ma per seguir virtute e canoscenza.

Dante , Inferno XXVI

Since the discovery of the laws of electromagnetism by Maxwell, physicists have maintained a high level of interest in the interaction between radiation and matter. One of the first successfully described processes was the scattering of light from molecules in the atmosphere by Lord Rayleigh (1842 - 1919), now known as Rayleigh scattering. Rayleigh scattering is applicable when the radius of the scattering particle is much smaller than the wavelength of the incident light and explains why light from the sky is blue (and red during twilight): the intensity of the scattered light varies with the inverse of the fourth power of the wavelength.

Increasing the frequency of the radiation permits matter to be probed at smaller and smaller scales, and in accordance with this, the next notable discovery was that of X-ray radiation by W.C. Röntgen in 1895 and its application by M. von Laue, W.H. and W.L. Bragg to diffraction experiments which directly probed the lattice structure of crystals.

With the discovery of the photoelectric effect, theoretically explained by A. Einstein, and the scattering of light off electrons by A.H. Compton, experiments with light entered the domain of quantum mechanics.

It was only in the 70s, mainly thanks to the work of J. Schwinger, R. P. Feynman and H. Tomonaga that a consistent quantum field theory of electromagnetic phenomena (quantum electrodynamics, or QED) was finally achieved.

The existence of a reliable theory of electromagnetic interactions permits them to be used for investigating matter at nuclear and subnuclear scales where the strong interaction becomes important.

A quantum field theory of strong interactions is also known: Quantum Chromodynamics (QCD). The discovery of asymptotic freedom by D. Gross, D. Politzer and F. Wilczek (2004 Nobel Prize) allowed precise calculations to be made using the techniques of perturbation theory in high energy experiments, but QCD also has another side, called confinement: the force between color charges increases with distance which leads to the combination of colored quarks and gluons into uncolored hadrons. In the low energy region, where confinement dominates, the QCD coupling constant is large and hence perturbation theory is not applicable.

Confinement is verified within lattice QCD computations, but it is still not mathematically proven and predictions are difficult, thus experimental efforts are required in order to have more insight into these complex strongly interacting systems.

Due to its success, QED allows electromagnetic probes (leptons and photons) to be used to investigate strongly interacting systems like nuclei and hadrons, in this way only the strongly interacting part of the induced quantum transitions is unknown. Since the pioneering experiments of R. Hofstadter [1] (1961 Nobel Prize) in which electron scattering off nuclei and nucleons was performed for the first time, the experimental techniques have evolved until the present day with the advent of the modern continuous wave electron accelerators with high currents and duty cycles, which make very precise coincidence experiments possible.

An example is Compton scattering off the nucleon, which allows for the measurement of the nucleon's electric and magnetic polarizabilities. A photon beam is used and the events are sought in which a photon and a nucleon appear in the final state. A generalization of this process is virtual Compton scattering (VCS), where an electron scatters off a proton exchanging a virtual photon (first order in perturbation theory). The excited proton decays then in its ground state emitting a photon as in Compton scattering. The advantage of VCS over Compton scattering is that the energy and momentum of the virtual photon can be varied independently, whilst for a real photon a fixed relation between them exists. Fixing the energy of the virtual photon, the momentum q can be varied and six new observables as a function of q can be measured: the Generalized Polarizabilities (GPs).

As the form factors represent the distribution of charges and magnetic moments inside the nucleon, the generalized polarizabilities represent the distribution of the electric and magnetic polarizability.

Two of them reduce in the limit $q \rightarrow 0$ to the electric and magnetic polarizabilities of Compton scattering, the other four are new observables.

Measuring the GPs is very important for extending our knowledge of the electromagnetic structure of the nucleon by testing the existing theoretical models on a new ground. Two combinations of the GPs have already been measured at MAMI, but the disentanglement of the single GP contributions has still not been achieved. The disentanglement of five GPs requires a double polarization experiment. A polarized beam and the measurement of the recoil proton polarization are needed. The sixth GP can only be measured if out-of-plane acceptance is also provided.

The three spectrometer setup at MAMI has all the characteristics needed for this measurement: a continuous wave electron accelerator with a highly polarized beam ($\sim 80\%$), high resolution coincidence spectrometers and a proton polarimeter.

The content of this thesis is summarized below by chapter:

- **Chapter 2:**

A theoretical introduction to real and virtual Compton scattering is given, the kinematics is defined together with the experimental observables.

- **Chapter 3:**

The actual theoretical and experimental status of VCS is reviewed. Many theoretical models are available for the calculation of the generalized polarizabilities and they are briefly discussed and their results presented.

Three unpolarized experiments have already been performed, while one single spin asymmetry experiment exists. At MAMI the first double polarization VCS

experiment was performed and it is also the subject of this work.

- **Chapter 4:**

The experimental setup of the A1 Collaboration at MAMI is described: it consists of three high resolution magnetic spectrometers placed around a target which can consist of solid state materials or cryogenic liquids as hydrogen or helium. The standard detector package consists in two scintillator planes, four planes of vertical drift chambers and Čerenkov detectors. In one spectrometer also a proton polarimeter can be installed.

The main properties of the MAMI electron accelerator are described and the functioning principle of the Møller polarimeter and of the trigger electronics are explained.

- **Chapter 5:**

A method for reconstructing the proton polarization, based on a maximum likelihood procedure is developed and extended to the direct fit of the generalized polarizabilities to the data.

- **Chapter 6:**

The standard A1 simulation software is extended in order to simulate the whole procedure for the extraction of the proton polarization. The procedure is further extended for the simulation of the generalized polarizabilities.

- **Chapter 7:**

In this chapter the results for the unpolarized cross section measurement for the VCS process are presented. For one particular setup the Rosenbluth separation method was used for the extraction of two combinations of generalized polarizabilities.

- **Chapter 8:**

The analysis of the double polarization observable is presented. The recoil proton polarization is measured with the focal plane polarimeter and this data are then used for extracting a new structure function.

Chapter 2

Theoretical Foundations

The sciences do not try to explain, they hardly even try to interpret, they mainly make models. By a model is meant a mathematical construct which, with the addition of certain verbal interpretations, describes observed phenomena. The justification of such a mathematical construct is solely and precisely that it is expected to work.

Johann von Neumann

2.1 Motivation

As the lightest baryons, protons and neutrons are the basic constituents of atomic nuclei and are summarized under the name of “nucleons”. In the constituent quark picture, baryons are made of three quarks with flavour content (uud) for the proton and (udd) for the neutron, but over years of intense research, their structure has presented many surprises. Nowadays hadrons are considered as complex systems where different degrees of freedom play a role in building the final structure. This complexity comes from the underlying theory of strong interactions, quantum chromodynamics (QCD), which acts between the elementary constituents of the baryons: the quarks. Quarks interact exchanging gluons and gluons can interact amongst themselves directly, giving rise to complicated dynamics, one of the most striking consequences is that of the mass of the nucleon (~ 940 MeV): only a few percent is carried by the quarks and the large remaining part is generated by the interaction. Understanding the internal structure of the baryons is still a central problem of QCD.

As quarks are charged particles, the response of the nucleon to external electromagnetic fields can be studied to aid our understanding of the internal distribution of electric charges and currents.

Historically the first scattering experiment using electromagnetic probes was elastic electron scattering off the proton, from which the electric and magnetic form factors were determined. This confirmed that the proton is not a pointlike particle, but has a spatial extension and also that the charges within it are not homogeneously distributed. The Fourier transformation of the form factors directly gives the spatial distribution of the electric charge and magnetic moments.

With real Compton scattering experiments, where a photon is used to probe the nucleon, the electromagnetic “rigidity” of the nucleon can also be measured in the form of electric and magnetic polarizabilities.

The polarizabilities provide a direct way to measure how tightly the constituents

of the nucleon are bound together. In systems like atoms, where only the electromagnetic force acts, the polarizability is approximately equal to the volume, but for nucleons it is much smaller (the volume is $\sim 1\text{fm}^3$, whereas the polarizabilities are $\sim 10^{-4}\text{fm}^3$); this is a direct sign that a stronger force is acting to keep the constituents together.

In analogy to the form factors, which give information about the spatial distribution of the charge and magnetic moments, we can raise the question about how the polarizations are distributed inside the nucleon. The answer to this question can be given by virtual Compton scattering (or photon electroproduction) experiments, where a virtual photon is used instead of a real one to probe the nucleon structure. VCS gives the possibility to measure six new observables, the so called *generalized polarizabilities*, and two of them are the direct generalization of the electric and magnetic polarizabilities in real Compton scattering. As stated in [4], measuring all the generalized polarizabilities amounts to the maximal information which can be extracted about the nucleon at low energy using electromagnetic probes. In this chapter an introduction to the theoretical description of VCS will be given, starting from a brief discussion about the basic physical concept of polarizability.

2.2 Classical Polarizability

Materials under the influence of electromagnetic fields exhibit interesting behavior. Let us start with the simplest case of a material in a constant electric field \vec{E} . The atoms and molecules that form it respond to this field giving rise to a macroscopic electric polarization. To a first approximation the polarization \vec{P} is proportional to the external field \vec{E} :¹

$$\vec{P} = \chi \vec{E}. \quad (2.1)$$

The polarization vector \vec{P} can vary within the material and this can be treated in different ways depending on the direction of the field, so the last equation should be generalized as:

$$P_i = \sum_j \alpha_{ij} E_j, \quad (2.2)$$

where the polarization tensor α_{ij} has been introduced.

The action of magnetic fields on matter is more complicated, giving rise to a distinction between three classes: the *diamagnets* are repulsed by magnetic fields, the *paramagnets* and the *ferromagnets* are attracted (more strongly in the latter case). The case of time-varying electromagnetic fields introduces physical concepts which are described by Maxwell's equations for the fields

$$\nabla \times \vec{E} + \frac{\partial \vec{B}}{\partial t} = 0 \quad \nabla \cdot \vec{B} = 0, \quad (2.3)$$

$$\nabla \times \vec{B} - \frac{\partial \vec{E}}{\partial t} = 4\pi \vec{j} \quad \nabla \cdot \vec{E} = 4\pi \rho. \quad (2.4)$$

¹In the following, units of measure with $c=1$ are used.

and equations describing the material, like Eq. (2.1).

Such a variety of behaviors is connected to the microscopic nature of matter. If we have a model for the structure of matter, one way to test it is to expose some material under the influence of an electromagnetic field and looking at the induced effects. This basic concepts remain very useful also when one tries to understand matter at very small scales, where quantum effects are determinant.

2.3 Quantum Polarizability

Consider now a quantum system like an atom and supposing a linear response, one can relate the induced electric and magnetic dipole moments to the fields in the following way

$$\vec{d} = \alpha \vec{E} \quad \vec{\mu} = \beta \vec{B}. \quad (2.5)$$

Introducing the four-vector potential $A_\mu^{ext} = (A_0, \vec{A})$ for the external fields, the density current (in the linear response approximation) inside the system rearranges itself as

$$\delta J^\mu(x) = \int d^4y P^{\mu\nu}(x, y) A_\nu^{ext}(y), \quad (2.6)$$

where the polarizability tensor $P^{\mu\nu}$ is used. The induced electric (magnetic) dipole momentum is $\delta \vec{d}$ ($\delta \vec{\mu}$). We can expand the density current in powers of the electric charge

$$J^\mu = e j^\mu + e^2 S^{\mu\nu} A_\nu^{ext}, \quad (2.7)$$

where the contact (or ‘‘Seagull’’) term $S^{\mu\nu}$ appears. In the following, two simplified cases will be discussed in more detail.

Electric Field

In case of an external electric field the potential can be defined as

$$A^0 = -\vec{r} \cdot \vec{E} \quad \text{and} \quad \vec{A} = 0, \quad (2.8)$$

Defining the electric dipole moment as

$$\vec{d} = \int d\vec{r} \vec{r} j^0(\vec{r}), \quad (2.9)$$

the dipole moment induced by a purely electric external field is, using Eq. 2.5 and Eq .2.7

$$\delta \vec{d} = \int d\vec{r} \vec{r} \delta J^0(\vec{r}) = \alpha \vec{E}. \quad (2.10)$$

Evaluating the last equation with perturbation theory one obtains the following expression for the electric polarizability:

$$\alpha = \frac{e^2}{3} \sum_{N' \neq N} \frac{|\langle N | \vec{d} | N' \rangle|^2}{E_{N'} - E_N}. \quad (2.11)$$

The electric polarizability α has always a positive value.

Magnetic Field

In case of an external magnetic field the potential can be defined as

$$A^0 = 0 \quad \vec{A} = \frac{1}{2} \vec{r} \times \vec{B}. \quad (2.12)$$

The definition of the dipole magnetic moment is given by

$$\vec{\mu} = \frac{1}{2} \int d\vec{r} \vec{r} \times \vec{j}(\vec{r}), \quad (2.13)$$

and then the induced dipole magnetic moment is

$$\delta\vec{\mu} = \frac{1}{2} \int d\vec{r} \vec{r} \times \delta\vec{J}(\vec{r}) = \underbrace{(\beta_{dia} + \beta_{para})}_{\beta} \vec{B}. \quad (2.14)$$

The magnetic polarizability has two different components reflecting a different kind of response of the system to a purely magnetic field. The *diamagnetic* polarizability

$$\beta_{dia} = -\frac{e^2}{6} \langle N | \int dr' r'^2 j_0(\vec{r}') | N \rangle, \quad (2.15)$$

is negative while the *paramagnetic* polarizability

$$\beta_{para} = \frac{e^2}{3} \sum_{N' \neq N} \frac{|\langle N | \vec{\mu} | N' \rangle|^2}{E_{N'} - E_N}, \quad (2.16)$$

is positive. The total response of the system can be described by the magnetic polarizability $\beta = \beta_{dia} + \beta_{para}$.

2.4 Real Compton Scattering

Coherent elastic scattering of photons on the nucleon is equivalent to probing it with an external quasi-static electromagnetic field. With Real Compton Scattering (RCS) off the proton one refers to the reaction $\gamma p \rightarrow \gamma p$ where a real photon scatters on a target nucleon. This process is completely described by the amplitude

$$T = \sum_{i=1}^6 \mathcal{A}_i(\omega, \theta) \mathcal{F}_i(\vec{\epsilon}, \vec{\epsilon}', \hat{k}, \hat{k}', \vec{\sigma}), \quad (2.17)$$

where the kinematical functions \mathcal{F}_i depend on the polarization ϵ (ϵ') and momentum direction \hat{k} (\hat{k}') of the incident (outgoing) photon. The Pauli matrices $\vec{\sigma}$ describe the spin state of the proton. The six structure functions (which encode the nucleon structure information) \mathcal{A}_i are dependent on the energy of the photon ω and the scattering angle θ .

The structure functions can be expanded in powers of the photon energy ω

$$\mathcal{A}_i(\omega, \theta) = a_{0i} + a_{1i}\omega + a_{2i}\omega^2 + a_{3i}\omega^3 + \dots \quad (2.18)$$

The first two terms, a_{0i} and a_{1i} are fixed in case of a spin $\frac{1}{2}$ system by the low energy theorem of Low, Gell-Mann and Goldberger [2], [3] which states under very general assumptions of quantum field theory that they are dependent only from known quantities: the electric charge e , the proton mass M and anomalous magnetic moment κ . The term a_{2i} is the first containing information on the proton structure in the form of the quantities $\bar{\alpha}$, $\bar{\beta}$, γ_0 and γ_π . The first two are called respectively *electric* and *magnetic polarizabilities* and differ from α and β of Sec. 2.3 by corrections due to recoil and relativistic effects. The remaining two quantities γ_0 and γ_π are the *forward* and *backward polarizabilities*.

The differential cross section of RCS in the laboratory frame is

$$\frac{d\sigma}{d\Omega} = \frac{1}{8\pi M} \frac{\omega'}{\omega} |T_{fi}|^2, \quad (2.19)$$

with outgoing photon energy $\omega' = \omega/(1 + \frac{2\omega}{M})$.

In the two cases of forward ($\theta = 0$) and backward ($\theta = \pi$) directions one has

$$\frac{1}{8\pi M} [T_{fi}]_{\theta=0} = f_0(\omega) \vec{\epsilon}^* \cdot \epsilon + g_0(\omega) i\vec{\sigma} \cdot (\vec{\epsilon}^* \times \epsilon), \quad (2.20)$$

$$\frac{1}{8\pi M} [T_{fi}]_{\theta=\pi} = f_\pi(\omega) \vec{\epsilon}^* \cdot \epsilon + g_\pi(\omega) i\vec{\sigma} \cdot (\vec{\epsilon}^* \times \epsilon). \quad (2.21)$$

These amplitudes are expanded like in Eq. (2.18) in powers of the photon energy

$$f_0(\omega) = -(e^2/4\pi M)q^2 + \omega^2(\alpha + \beta) + \dots, \quad (2.22)$$

$$g_0(\omega) = \omega[-(e^2/8\pi M^2)\kappa^2 + \omega^2\gamma_0 + \dots], \quad (2.23)$$

$$f_\pi(\omega) = (1 + (\omega'\omega/M^2))^{1/2}[-(e^2/4\pi M)q^2 + \omega'\omega(\alpha - \beta) + \dots], \quad (2.24)$$

$$g_\pi(\omega) = \sqrt{\omega'\omega}[(e^2/8\pi M^2)(\kappa^2 + 4q\kappa + 2q^2) + \omega'\omega\gamma_\pi + \dots]. \quad (2.25)$$

In an unpolarized experiment, the cross section reduces to

$$\begin{aligned} \frac{d\sigma}{d\Omega} &= \left(\frac{d\sigma}{d\Omega} \right)^{Born} \\ &- \frac{e^2}{4\pi M} \left(\frac{\omega'}{\omega} \right) \omega\omega' \left[\frac{\alpha + \beta}{2} (1 + \cos\theta)^2 + \frac{\alpha - \beta}{2} (1 - \cos\theta)^2 \right] + O(\omega^4). \end{aligned} \quad (2.26)$$

In the last equation the effect of the polarizabilities is clearly visible, in addition to the Born cross section for light scattering on a point-like particle with anomalous magnetic moment. Experimental efforts in measuring the unpolarized nucleon polarizabilities can be summarized in the following results based on the global available data [8]:

	α (10^{-4}fm^3)	β (10^{-4}fm^3)	γ_π (10^{-4}fm^4)
Proton	12.0 ± 0.6	1.9 ∓ 0.6	-38.7 ± 1.8
Neutron	12.5 ± 1.7	2.7 ∓ 1.8	-58.6 ± 4.0

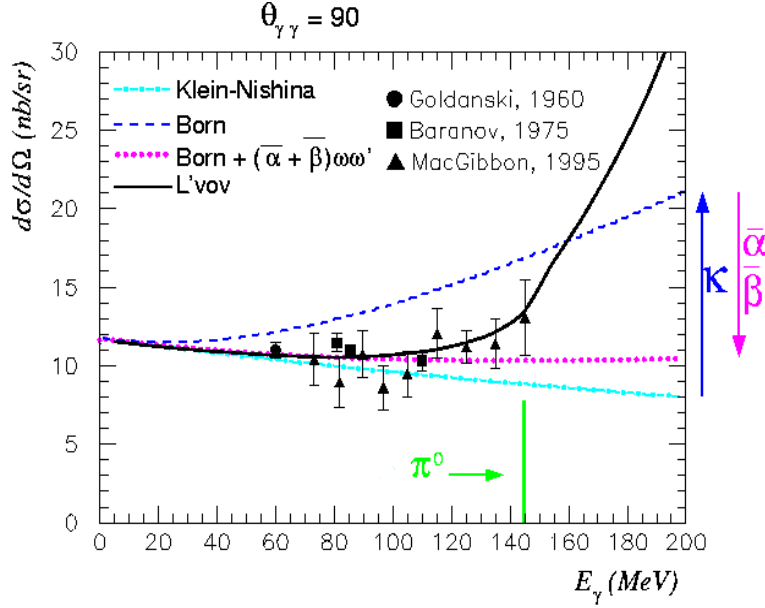


Figure 2.1: Compton scattering cross section as a function of the initial photon in the laboratory frame (from [7]): theoretical models and experiments. The π^0 production threshold is also indicated.

The errors on α and β are anticorrelated, because these quantities are extracted experimentally from Eq. 2.26 as sum and difference of them.

The term a_{3i} contains informations about the nucleon structure in the form of four observables $\gamma_1, \gamma_2, \gamma_3$ and γ_4 , the so-called *third order spin polarizabilities* [9]. The name comes from the fact that the functions \mathcal{F}_i depend from the Pauli matrices $\vec{\sigma}$, and they show up for the first time in the power expansion at the third order. The spin polarizabilities are accessible only with polarized experiments.

2.5 Virtual Compton Scattering

Virtual Compton Scattering (VCS) is defined by the reaction: $\gamma^* + p \rightarrow p' + \gamma$ where γ^* is a virtual photon. Experimentally it is accessed via electron scattering off the proton (photon electroproduction)

$$e + p \rightarrow e' + p' + \gamma. \quad (2.27)$$

VCS permits to vary independently energy q^0 and momentum \vec{q} of the incoming virtual photon, in contrast to RCS where the use of a real photon implies a fixed relation between them ($q^0 = |\vec{q}|$).

The consequence of having more degrees of freedom is the emergence of six new observables, while in the case of RCS we had only two. This observables are called *generalized polarizabilities* and they will be defined later in this chapter. The concept of generalized polarizabilities was introduced originally by H.Arenhövel and D.Drechsel within the study of the electromagnetic response of nuclei [28]. The first paper concerning the generalized polarizabilities of the nucleon was published by P.

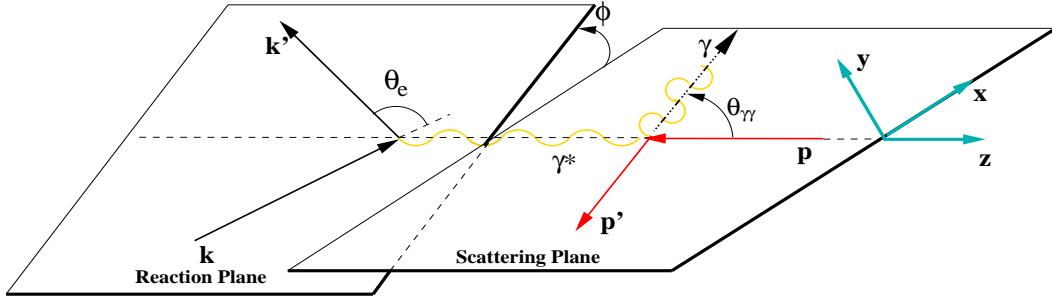


Figure 2.2: Kinematics of the VCS reaction in the center of mass reference frame.

A. M. Guichon, G.Q. Liu and A. W. Thomas [10] and in the following we will use the kinematical conventions of that work.

2.5.1 Definition of the Kinematics

For describing completely the photon electroproduction reaction, five variables are needed. In a fixed target experiment, where the final state proton and electron are detected in coincidence, it is suitable to describe the reaction with the following variables: k_{lab} (k'_{lab}) is the fourvector of the incoming (outgoing) electron, θ_e^{lab} is the electron scattering angle, p'_{lab} is the fourvector of the scattered proton and φ the angle between the reaction and scattering planes. In the center of mass frame (CM) the description is more convenient from the point of view of the theoretical calculations. The situation is depicted in Fig. 2.2: in the CM frame the real photon and the scattered proton are emitted back-to-back while the incoming virtual photon and the proton (at rest in the laboratory) collide along the same axis. We define then the angle $\theta_{\gamma\gamma}$ as the angle between the two photons in the CM frame.

Using the laboratory frame variables, the following relativistic invariants can be calculated: Q^2 (the exchanged virtual photon invariant mass) and $s = -Q^2 + M^2 + 2M\nu_{lab}$ (the square of the total center of mass energy for the γp system). Using this invariants, energy and momentum of each particle can be calculated:

	Energy	Momentum
Virtual Photon	$q^0 = \frac{s-Q^2-M^2}{2\sqrt{s}}$	$q = \sqrt{Q^2 + q^{0^2}}$
Real Photon	$q'^0 = \frac{s-M^2}{2\sqrt{s}}$	$q' = q^0$
Initial Proton	$p^0 = \frac{s+Q^2+M^2}{2\sqrt{s}}$	$p = q$
Final Proton	$p'^0 = \frac{s+M^2}{2\sqrt{s}}$	$p' = q'$

In [10] the calculations were done choosing $(q, q', \epsilon, \theta_{\gamma\gamma}, \varphi)$ as set of variables defining the reaction together with the reference system shown in Fig. 2.2 and defined by

$$\begin{aligned}\hat{z} &= \vec{q}_{cm}/q_{cm} \ , \\ \hat{y} &= \frac{\vec{q}_{cm} \times \vec{q}'_{cm}}{q_{cm}q'_{cm} \sin \theta_{\gamma\gamma}} \ , \\ \hat{x} &= \hat{y} \times \hat{z} \ .\end{aligned}$$

The variable $\epsilon = \left[1 + 2\frac{q_{lab}^2}{Q^2} \tan^2\left(\frac{\theta_e}{2}\right)\right]^{-1}$ is the degree of linear polarization of the virtual photon on the plane orthogonal to its momentum in the approximation of $m_e = 0$. The Lorentz boost from the CM frame to the laboratory frame (see App. C) implies that the proton is scattered in a narrow cone around the boost direction (the direction of the virtual photon). The effect of the boost on the real photon, being a non massive particle, is much less pronounced and the phase space of it is less focused. The result is that with a magnetic spectrometer with a limited acceptance for the proton, a correspondingly larger phase space for the photon can be measured.

2.5.2 Contributions to the Photon Electroproduction Process

For the calculation of the photon electroproduction amplitude $T^{ee'\gamma}$, all the contributing processes have to be considered: in Fig. 2.3 they are depicted as Feynman diagrams. In Fig. 2.3(a) the full amplitude is shown, followed (Fig. 2.3(b) and (c)) by the Bethe-Heitler process, where the final real photon is radiated by the incoming or outgoing electron. The Born process is depicted in Fig. 2.3(d) and (e), where the final photon is radiated by the proton without excitation of the internal degrees of freedom. In Fig. 2.3(f) the VCS (*non-Born*) contribution is shown: the proton is excited by the incident virtual photon and the de-excitation mechanism proceeds via the emission of a real photon. The BH process gives the main contribution to photon electroproduction: between it and the Born process a difference of about six orders of magnitude can be found. The contribution of the non-Born amplitude on the total cross section is about 10-15%: this means that in order to measure the effect of it, a phase space region where the BH process gives a small contribution has to be chosen. In the following, the various processes will be discussed separately.

Bethe-Heitler Amplitude T^{BH}

This process constitutes the main contribution to the VCS reaction: the final real photons are emitted from the incoming or outgoing electrons. The BH process cannot be experimentally separated from the VCS amplitude. Fortunately, with the knowledge of the nucleon form factors, the amplitude is exactly calculable within QED

$$T^{BH} = \frac{-e^3}{t} \epsilon_\mu'^* L^{\mu\nu} \bar{u}(p') \Gamma_\nu(p', p) u(p) \ . \quad (2.28)$$

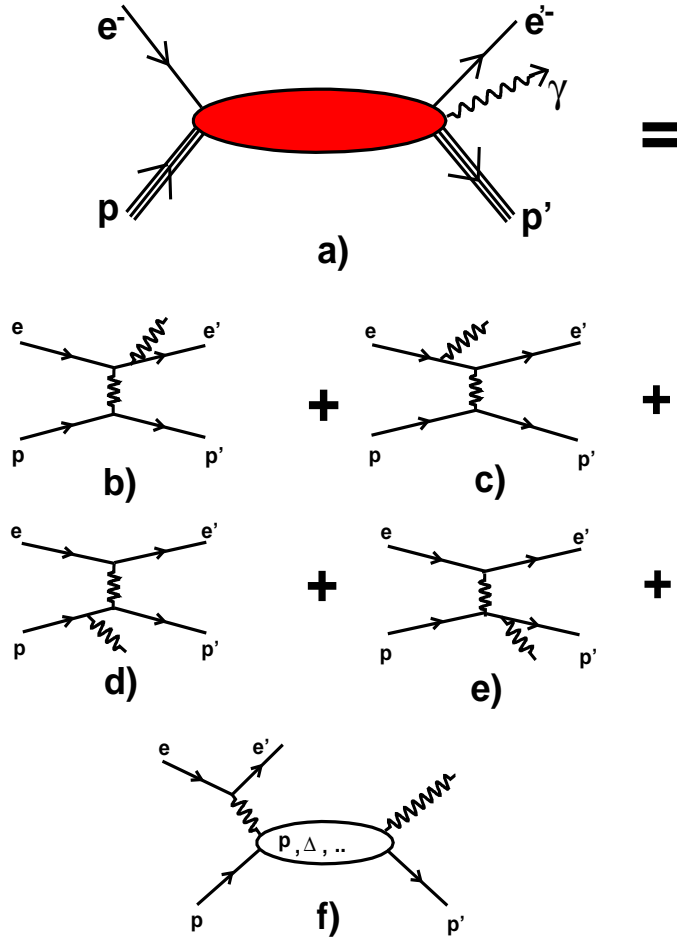


Figure 2.3: Main processes in photon electroproduction a): in b) and c) the Bethe-Heitler process is represented, where the photon is radiated by the incoming or outgoing electron; d) and e) are the Born diagrams, where the photon is radiated by the incoming or outgoing proton, but without excitation of internal degrees of freedom. The diagram f) is the *non-Born* VCS contribution, where the photon emission follows the proton excitation.

The interaction vertex $L^{\mu\nu}(p', p) = F_1((p' - p)^2)\gamma^\nu + iF_2((p' - p)^2)\sigma^{\nu\rho}(p' - p)$ is a function of the form factors and ϵ'^* is the final photon polarization. The lepton tensor is also exactly known from QED

$$L^{\mu\nu} = \bar{u}(k') \left(\gamma^\mu \frac{1}{\gamma(k' + q') - m_e + i\epsilon} \gamma^\nu + \gamma^\nu \frac{1}{\gamma(k' - q') - m_e + i\epsilon} \gamma^\mu \right) u(k). \quad (2.29)$$

In Fig. 2.4, the cross section of the BH process is shown as a function of the $\theta_{\gamma\gamma}$ angle: two spikes are clearly visible and correspond to the directions of the incoming and outgoing electron: the photon is mainly emitted along this two directions. The only possibility to measure the VCS effect is to move away from this peaks, otherwise a difference of about six orders of magnitude will be present between the two processes (note the logarithmic scale of Fig. 2.4).

This is the reason why the measurements are done in the angular region of about $\theta_{\gamma\gamma} \in [-180^\circ, 0^\circ]$ and still the BH background represents a challenge for the experiments.

Full Virtual Compton Scattering Amplitude $T^B + T^{nB}$

The amplitude corresponding to the case where the photon is emitted from the proton is called *full VCS* amplitude and it can be further divided in a Born contribution, where the nucleon is not excited and the VCS amplitude (or non-Born), where the internal nucleon structure plays a role. Also for the Born amplitude, like in the case of the BH one, only the knowledge of the form factors is needed for calculating it. The full VCS amplitude has the following expression

$$T^{FVCS} = \frac{e^3}{q^2} \epsilon_\mu^{\prime*} H^{\mu\nu} \bar{u}(k') \gamma_\nu u(k). \quad (2.30)$$

The hadronic tensor $H^{\mu\nu}$ contains the information about the nucleon structure. The hadronic tensor can be further decomposed in a Born and in a non-Born part: $H_{FVCS} = H_B + H_{nB}$ The Born term can be written as

$$\begin{aligned} H_B^{\mu\nu} = & \bar{u}(p') \Gamma^\mu(p', p' + q') \frac{\gamma(p' + q') + m}{(p' + q')^2 - m^2} \Gamma^\nu(p' + q', p) u(p) + \\ & \bar{u}(p') \Gamma^\nu(p', p - q') \frac{\gamma(p - q') + m}{(p - q')^2 - m^2} \Gamma^\mu(p - q', p) u(p). \end{aligned} \quad (2.31)$$

The non-Born part is a regular function of the outgoing real photon fourvector q'^μ and it has then a polynomial expansion around $q'^\mu = 0$

$$H_{nB}^{\mu\nu} = a^{\mu\nu} + b_\alpha^{\mu\nu} q'_\alpha + O(q'^2). \quad (2.32)$$

As proven in [10], the gauge invariance condition for this amplitude requires $a^{\mu\nu} = 0$, so $H_{nB}^{\mu\nu}$ is at least of order q' .

The non-Born amplitude will be treated in the next sections introducing a parameterization based on the generalized polarizabilities.

2.6 Low Energy Expansion

Considering the expressions obtained for the Bethe-Heitler and Born amplitudes one can expand them for a low energy outgoing photon ($q'^\mu \approx 0$)

$$T^{BH} = \frac{a_{-1}^{BH}}{q'} + a_0^{BH} + a_1^{BH} q' + O(q'^2), \quad (2.33)$$

$$T^{Born} = \frac{a_{-1}^{Born}}{q'} + a_0^{Born} + a_1^{Born} q' + O(q'^2). \quad (2.34)$$

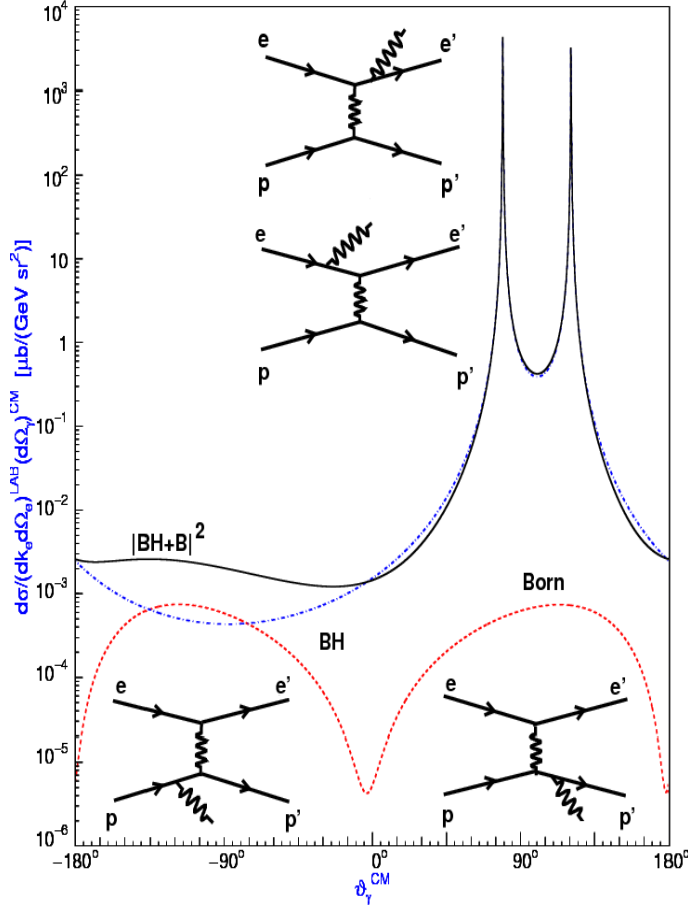


Figure 2.4: Unpolarized fivefold differential cross section for the following electron photoproduction processes in the CM frame: dashed (red) curve is the Born term contribution; dash-dotted (blue) curve is the Bethe-Heitler contribution while the full (black) curve is the coherent sum of the two.

Combining the last two equations with Eq. (2.32) where $b_{\alpha}^{\mu\nu} \equiv a_1^{nBorn}$ we find

$$T^{ee'\gamma} = \frac{a_{-1}^{BH} + a_{-1}^{Born}}{q'} + (a_0^{BH} + a_0^{Born}) + [(a_1^{BH} + a_1^{Born}) + a_1^{nBorn}] q' \equiv \quad (2.35)$$

$$\frac{a_{-1}}{q'} + a_0 + (a_1 + a_1^{nBorn}) q' + O(q'^2).$$

In the last line, the coefficients are renamed grouping the terms accordingly with their order in q' .

The last result is the famous Low Energy Theorem [2], [3] which states that the first two terms, a_{-1} and a_0 , are exactly calculable (knowing the electromagnetic form factors of the nucleon).

In analogy with the real Compton scattering case, the first non trivial term, dependent from the internal nucleon structure, is found in a low energy expansion at first order in q' .

2.7 Generalized Polarizabilities

The BH and Born amplitudes are completely calculable for given nucleon form factors. What is needed is a parameterization for the non-Born amplitude which is on the contrary a priori unknown.

As already noted, the non-Born amplitude is regular in q^μ , therefore it can be expanded on an orthonormal basis of angular momentum eigenstates. Following [10], the amplitude is expanded in vectorial spherical harmonics. The resulting multipole amplitudes $H_{nB}^{(\rho'L',\rho L)S}(q, q')$ characterize the type of electromagnetic transition induced.

In the notation introduced for the multipoles, L (L') is the initial (final) photon angular momentum; S=0,1 is the orientation of the spin of the final proton (S=0 \rightarrow no spin flip, S=1 \rightarrow spin flip). The index ρ (ρ') indicates the type of multipole for the initial (final) photon: $\rho = 0$ for the charge multipoles, $\rho = 1$ for the magnetic and $\rho = 2$ for the electric ones. Not all the transitions are allowed but are constrained by selection rules. The possible transitions are constrained by angular momentum and parity conservation:

$$\begin{aligned} \text{Total Angular Momentum } (\gamma p \text{ system}) &\Rightarrow J = (L \pm \frac{1}{2}) = (L' \pm \frac{1}{2}) \\ \text{Parity} &\Rightarrow (-1)^{\rho+L} = (-1)^{\rho'+L'} \end{aligned}$$

Other constraints must be fulfilled:

- $|L - L'| \leq S \leq L + L'$
- The final photon is real, so $\rho' \neq 0$
- Since we expand the amplitude to order q' and the multipoles are expanded in powers of q and q' , the lowest order is $q^L q'^{L'}$ and this implies $L' = 1$.

Using all the above constraints, at order q' , the only allowed multipoles are

$$\begin{array}{cccccc} H_{nB}^{(11,00)1}, & H_{nB}^{(11,02)1}, & H_{nB}^{(11,22)1}, & H_{nB}^{(11,11)0}, & H_{nB}^{(11,11)1} \\ H_{nB}^{(21,01)0}, & H_{nB}^{(21,01)1}, & H_{nB}^{(21,21)0}, & H_{nB}^{(21,21)1}, & H_{nB}^{(21,12)1} \end{array}$$

From the selected multipoles, it is possible to define the *Generalized Polarizabilities* (GPs). The GPs describe the low energy behavior of the non Born amplitude at an arbitrary q :

$$P^{(\rho'1,\rho L)S}(q', q) = \text{Limit of } \frac{1}{q'} \frac{1}{q^L} H_{nB}^{(\rho'1,\rho L)S}(q', q) \quad \text{with } q' \rightarrow 0 \quad (2.36)$$

10 multipoles are allowed, but after the work of Drechsel *et al.* [14],[15] it was recognized that only 6 GPs are independent. The reduction to six independent quantities is possible taking into account the nucleon crossing symmetry and charge conjugation, two fundamental symmetries of a relativistic quantum field theory.

The definition of the GPs has moreover a problem in the limit $(q_{CM}, q'_{CM}) \rightarrow (0, 0)$ which is the RCS point. This limit is physically interesting for making contact between the RCS and VCS processes. Referring to Fig. 2.5, in the RCS case the (0,0)

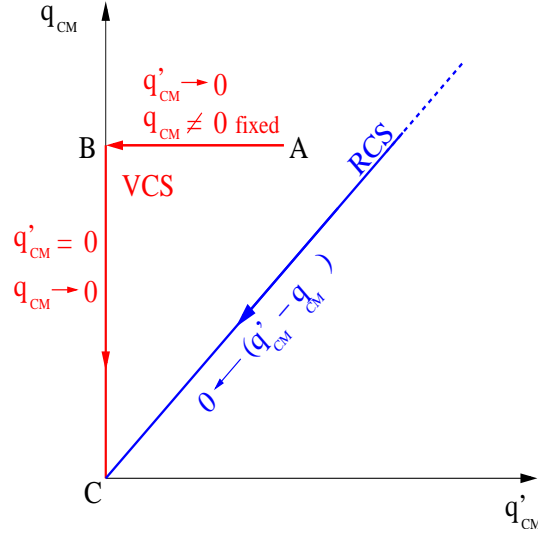


Figure 2.5: In the case of RCS, the point (0,0) is reached along the line $q_{CM} = q'_{CM}$, while in the VCS case a different path is used.

point is reached along the line $q_{CM} = q'_{CM}$. In the VCS case the limit $q'_{CM} \rightarrow 0$ is taken before (line AB) and then the limit $q_{CM} \rightarrow 0$ is performed (line BC).

A meaningful comparison between RCS polarizabilities and VCS generalized polarizabilities requires that the two limits will be independent from the path and it was shown to be the case for the $\rho(\rho') = 0, 1$ case to be true. In the case of $\rho(\rho') = 2$ the results are not independent from the path. A way to overcome this problem is to apply the Siegert theorem [29]. The theorem states that in the low energy limit the transverse electric multipoles are proportional to the longitudinal ones. This means that one can use charge multipoles instead of the transversal ones. The theorem is derived making use of the continuity equation, so charge and gauge invariance are maintained. The expression for the $\rho(\rho') = 2$ multipoles is then

$$H_{nB}^{(2L', \rho L)S}(q_{CM}, q'_{CM}) = -\sqrt{\frac{L'+1}{L'}} \frac{q^0}{q'} H_{nB}^{(0L', \rho L)S}(q, q') + O(q'^{L'+1}). \quad (2.37)$$

Finally, after the application of all the symmetry constraints and the use of the Siegert theorem, six independent generalized polarizabilities can be defined, with a consistent limit to the RCS case [12]:

$$P^{(01,01)0}(q) = \left[\frac{1}{q'q} H_{nB}^{(01,01)0}(q, q') \right]_{q'=0} \quad P^{(01,01)1}(q) = \left[\frac{1}{q'q} H_{nB}^{(01,01)1}(q, q') \right]_{q'=0}$$

$$P^{(11,11)0}(q) = \left[\frac{1}{q'q} H_{nB}^{(11,11)0}(q, q') \right]_{q'=0} \quad P^{(11,11)1}(q) = \left[\frac{1}{q'q} H_{nB}^{(11,11)1}(q, q') \right]_{q'=0}$$

$$P^{(11,02)1}(q) = \left[\frac{1}{q'^2} H_{nB}^{(11,02)1}(q, q') \right]_{q'=0} \quad P^{(01,12)1}(q) = \left[\frac{1}{q'^2} H_{nB}^{(01,12)1}(q, q') \right]_{q'=0}$$

Note that the GPs are functions of the transferred 3-momentum q (in the CM frame) only. If $q = 0$, the RCS case is recovered. In table 2.1 a summary of the generalized polarizabilities together with the main contributing resonances is given.

Generalized Polarizability	Transition (γ, γ^*)	RCS Polarizability	Excited State
$P^{(01,01)0}$	(E1,E1)	$P^{(01,01)0}(0) = -\frac{4\pi}{e^2} \sqrt{\frac{2}{3}} \bar{\alpha}$	$\frac{1}{2}^- ; \frac{3}{2}^-$
$P^{(01,01)1}$	(E1,E1)	$P^{(01,01)1}(0) = 0$	$\frac{1}{2}^- ; \frac{3}{2}^-$
$P^{(11,11)0}$	(M1,M1)	$P^{(11,11)0}(0) = -\frac{4\pi}{e^2} \sqrt{\frac{8}{3}} \bar{\beta}$	$\frac{1}{2}^+ ; \frac{3}{2}^+$
$P^{(11,11)1}$	(M1,M1)	$P^{(11,11)1}(0) = 0$	$\frac{1}{2}^+ ; \frac{3}{2}^+$
$P^{(01,12)1}$	(E1,M2)	$P^{(01,12)1}(0) = -\frac{4\pi}{e^2} \frac{\sqrt{2}}{3} \gamma_3$	$\frac{3}{2}^-$
$P^{(11,02)1}$	(M1,E2)	$P^{(11,02)1}(0) = -\frac{4\pi}{e^2} \sqrt{\frac{8}{27}} (\gamma_2 + \gamma_4)$	$\frac{3}{2}^+$
Resonances	I(J ^p)	Spectroscopic Notation	Polarizabilities
$\Delta(1232)$	$\frac{3}{2}(\frac{3}{2}^+)$	P_{33}	$P^{(11,11)0}, P^{(11,11)1}, P^{(11,02)1}$
$N(1440)$	$\frac{1}{2}(\frac{1}{2}^+)$	P_{11} (Roper)	$P^{(11,11)0}, P^{(11,11)1}$
$N(1520)$	$\frac{1}{2}(\frac{3}{2}^-)$	D_{13}	$P^{(01,01)0}, P^{(01,01)1}, P^{(01,12)1}$
$N(1535)$	$\frac{1}{2}(\frac{1}{2}^-)$	S_{11}	$P^{(01,01)0}, P^{(01,01)1}$

Table 2.1: Generalized Polarizabilities with the corresponding multipole transitions and RCS limit. The resonances mainly contributing to the GPs are summarized in the lower part of the table.

2.8 Observables in Virtual Compton Scattering

Having calculated the amplitudes, or in the case of T^{nB} , introduced the parameterization with the generalized polarizabilities, experimental observables can be calculated, like cross sections or asymmetries.

Asymmetries, which permit to measure polarization observables are important for mapping out all the components of the amplitudes, while an unpolarized measurement averages some of them out. The full formalism comprehending also the polarization observables was developed by P.A.M. Guichon and M. Vanderhaeghen in [12].

2.8.1 Structure Functions

Starting from the generalized polarizabilities, six independent structure functions can be defined. The observables will be constructed as a function of them. Following [12] we have

$$P_{LL}(q) = -2\sqrt{6}MG_E P^{(01,01)0}(q), \quad (2.38)$$

$$P_{TT}(q) = -3G_M \frac{q^2}{\tilde{q}_0} \left(P^{(11,11)1}(q) - \sqrt{2}\tilde{q}_0 P^{(01,12)1}(q) \right) \quad (2.39)$$

$$P_{LT}(q) = \sqrt{\frac{3}{2}} \frac{Mq}{\tilde{Q}} G_E P^{(11,11)0}(q) + \frac{3}{2} \frac{\tilde{Q}q}{\tilde{q}_0} G_M P^{(01,01)1} \quad (2.40)$$

$$P_{LT}^z(q) = \frac{3\tilde{Q}q}{2\tilde{q}_0} G_M P^{(01,01)1}(q) - \frac{3Mq}{\tilde{Q}} G_E P^{(11,11)1} \quad (2.41)$$

$$P'_{LT}{}^z(q) = -\frac{3}{2}\tilde{Q}G_M P^{(01,01)1}(q) + \frac{3Mq^2}{\tilde{Q}\tilde{q}_0}G_E P^{(11,11)1} \quad (2.42)$$

$$P'_{LT}{}^\perp(q) = \frac{3q\tilde{Q}}{2\tilde{q}_0}G_M \left(P^{(01,01)1}(q) - \sqrt{\frac{3}{2}}\tilde{q}_0 P^{(11,02)1}(q) \right). \quad (2.43)$$

For convenience the following combinations are also introduced

$$\begin{aligned} P_{LT}^\perp(q) &= \frac{RG_E}{2G_M}P_{TT} - \frac{G_M}{2RG_E}P_{LL} \\ P_{TT}^\perp(q) &= \frac{G_M}{RG_E}(P_{LT}^z - P_{LT}) = -\frac{q}{2}G_M \left(3P^{(11,11)1} + \sqrt{\frac{3}{2}}P^{(11,11)0}(q) \right) \\ P'_{TT}{}^\perp(q) &= \frac{G_M}{RG_E} \left(P'_{LT}{}^z + \frac{\tilde{q}_0}{q}P_{LT} \right) = \frac{q}{2}G_M \left(3\frac{q}{\tilde{q}_0}P^{(11,11)1} + \sqrt{\frac{3}{2}}\frac{\tilde{q}_0}{q}P^{(11,11)0}(q) \right). \end{aligned}$$

The kinematical coefficients used in the above expressions are reported in App. C.

2.8.2 Observables

With the aid of the defined structure functions, which are combinations of the generalized polarizabilities, various experimental observables can be constructed.

Unpolarized Cross Section

In the case of an unpolarized experiment, where neither the target nor the beam are polarized, in order to calculate \mathcal{M} , one has to average over all the initial state spins and sum over all final state spins. The unpolarized interaction probability is

$$\mathcal{M} = \frac{1}{4} \sum_{\sigma\sigma'h'\lambda'} |T^{ee'\gamma}|^2. \quad (2.44)$$

The general expression for the photon electroproduction cross section in the laboratory frame is [10]

$$\frac{d^5\sigma^{exp}}{dk'_{lab}d\Omega_{k'_{lab}}d\Omega_{p'}} = \underbrace{\frac{(2\pi)^{-5}k'_{lab}s - M^2}{64Mk_{lab}s}}_{\phi} \mathcal{M} = \underbrace{\frac{(2\pi)^{-5}k'_{lab}2q'}{64Mk_{lab}\sqrt{s}}}_{\phi} \mathcal{M}, \quad (2.45)$$

where ϕ is the phase space factor. Using the expansion given in Eq. 2.35, Eq. 2.45 can be written as

$$\begin{aligned} \frac{d^5\sigma^{exp}}{dk'_{lab}d\Omega_{k'_{lab}}d\Omega_{p'}} &= \phi q' \left| T^{ee'\gamma} \right|^2 \\ &= \phi q' \left| \frac{a_{-1}^{BH} + a_{-1}^{Born}}{q'} + (a_0^{BH} + a_0^{Born}) + (a_1^{BH} + a_1^{Born} + a_1^{nBorn})q' + \dots \right|^2 \\ &= \phi q' (\mathcal{M}_{-2}^{BH+Born} q'^{-2} + \mathcal{M}_{-1}^{BH+Born} q'^{-1} + (\mathcal{M}_0^{BH+Born} + \mathcal{M}_0^{nBorn}) + \dots) \\ &= \phi q' (\mathcal{M}_{-2} q'^{-2} + \mathcal{M}_{-1} q'^{-1} + \mathcal{M}_0 + \dots), \end{aligned} \quad (2.46)$$

where the coherent sum is calculated. The term \mathcal{M}_0^{nBorn} is an interference term between the BH+Born and the nBorn amplitudes. If we define the Bethe-Heitler+Born fivefold differential ² cross section as

$$d^5\sigma^{BH+B} = \phi q' \left(\mathcal{M}_{-2}^{BH+Born} q'^{-2} + \mathcal{M}_{-1}^{BH+Born} q'^{-1} + \mathcal{M}_0^{BH+Born} + \dots \right), \quad (2.47)$$

the interference term can be re-expressed as

$$\mathcal{M}_0^{nBorn} = (\mathcal{M} - \mathcal{M}^{BH+Born})|_{q'=0}. \quad (2.48)$$

Using the above formulas, the experimental cross section can be written as

$$d^5\sigma^{Exp} = d^5\sigma^{BH+B} + \phi q' \underbrace{\left[(\mathcal{M}_0 - \mathcal{M}^{BH+Born}) \right]}_{\text{Structure effects: GPs}} + \mathcal{O}(q'). \quad (2.49)$$

The term $d^5\sigma^{BH+B}$ is exactly calculable within QED while the term $(\mathcal{M}_0 - \mathcal{M}^{BH+Born})$ is the VCS contribution to the cross section in the low energy limit and it can be written using the structure functions as

$$\Psi_0 = \mathcal{M}_0 - \mathcal{M}^{BH+Born} = v_{LL} \left[P_{LL}(q) - \frac{1}{\epsilon} P_{TT} \right] + v_{LT} P_{LT}(q), \quad (2.50)$$

where v_{LL} and v_{LT} are kinematical coefficients (see App. C). From Eq. 2.49 it can be seen that subtracting $d^5\sigma^{BH+B}$ to the experimentally measured cross section $d^5\sigma^{Exp}$, the effect of the generalized polarizabilities can be extracted as the combination given by Eq. 2.50.

Single Spin Asymmetry

Measuring the VCS process using a beam of polarized electrons permits to access the single spin asymmetry observable

$$\mathcal{A} = \frac{\mathcal{M}(\xi^e) - \mathcal{M}(-\xi^e)}{\mathcal{M}(\xi^e) + \mathcal{M}(-\xi^e)}, \quad (2.51)$$

where ξ^e is the electron helicity.

Because of time reversal invariance and up to α_{QED} corrections, \mathcal{A} is different from zero only above pion threshold and also if the reaction and the hadronic planes do not coincide ($\varphi \neq 0$).

This observable is sensitive to the imaginary part of the VCS amplitude, since the numerator of Eq. 2.51 is proportional to $Im(T^{VCS}) \cdot Re(T^{VCS} + T^{BH})$: as can be seen also an interference term with the Bethe-Heitler amplitude is present, which has the effect of enhancing the asymmetry. Below pion threshold the VCS amplitude is purely real, but above it acquires an imaginary part due to the coupling to the πN channel. In this case it is not possible to use the low energy expansion formalism and a model which takes into account also the pion production has to be used. At the time of writing, the only existing model is based on dispersion relations [26].

Measuring this observable can be of help in understanding how well the VCS amplitude is known.

²Starting from here we will use the notation $\frac{d^5\sigma^{exp}}{dk'_{lab} d\Omega_{k'_{lab}} d\Omega_{p'}} \equiv d^5\sigma$

Double Polarization Observable

As previously seen, in an unpolarized experiment, only three combinations of the GPs appear. In order to have the possibility to separate all the six GPs, a double polarization experiment (where both the electron and proton polarizations are known) is required. It is possible to define a double polarization observable in virtual Compton scattering: keeping fixed the electron polarization, the average recoil polarization of the proton \mathcal{P} can be measured (or in alternative, a polarized proton target can be used). The polarization component along the direction \hat{i} is

$$\mathcal{P}_i = \frac{\mathcal{M}(\xi^e, \hat{i}) - \mathcal{M}(\xi^e, -\hat{i})}{\mathcal{M}(\xi^e, \hat{i}) + \mathcal{M}(\xi^e, -\hat{i})} = \frac{\Delta d^5\sigma}{2d^5\sigma} = \frac{\Delta d^5\sigma^{BH+B} + \phi q' \Delta \mathcal{M}^{nBorn}(h, \hat{i}) + \mathcal{O}(q'^2)}{2d^5\sigma}, \quad (2.52)$$

introducing the directions $\hat{i} = \{\hat{x}, \hat{y}, \hat{z}\}$ defined in Fig. 2.2. In the last part of Eq. 2.52 the double spin asymmetry is rewritten as a function of the cross sections and using the low energy theorem: in the denominator we find the unpolarized VCS cross section $d^5\sigma$, while in the numerator appear the functions $\Delta \mathcal{M}^{nBorn}(h, \hat{i})$ with the following expressions for each component [12]

$$\Delta \mathcal{M}^{nBorn}(h, \hat{x}) = 4K_2(2h) \left\{ \begin{array}{ll} v_1^x \sqrt{2\epsilon(1-\epsilon)} P_{LT}^\perp(q) & + v_2^x \sqrt{1-\epsilon^2} P_{TT}^\perp(q) + \\ v_3^x \sqrt{1-\epsilon^2} P_{TT}'^\perp(q) & + v_4^x \sqrt{2\epsilon(1-\epsilon)} P_{LT}'^\perp(q) \end{array} \right\}, \quad (2.53)$$

$$\Delta \mathcal{M}^{nBorn}(h, \hat{y}) = 4K_2(2h) \left\{ \begin{array}{ll} v_1^y \sqrt{2\epsilon(1-\epsilon)} P_{LT}^\perp(q) & + v_2^y \sqrt{1-\epsilon^2} P_{TT}^\perp(q) + \\ v_3^y \sqrt{1-\epsilon^2} P_{TT}'^\perp(q) & + v_4^y \sqrt{2\epsilon(1-\epsilon)} P_{LT}'^\perp(q) \end{array} \right\}, \quad (2.54)$$

$$\Delta \mathcal{M}^{nBorn}(h, \hat{z}) = 4K_2(2h) \left\{ \begin{array}{ll} -v_1 \sqrt{1-\epsilon^2} P_{TT}(q) & + v_2 \sqrt{2\epsilon(1-\epsilon)} P_{LT}^z(q) + \\ v_3 \sqrt{2\epsilon(1-\epsilon)} P_{LT}'^z(q) & \end{array} \right\}. \quad (2.55)$$

If the recoil proton polarization is measured using a polarized electron beam, $\Delta \mathcal{M}^{nBorn}(h, \hat{i})$ can be extracted. Together with the unpolarized cross section, all the information for extracting the GPs is available. The range in $\theta_{\gamma\gamma}$ and ϕ is important for the measurement: for example, if $\phi = 0$ (in-plane measurement), the coefficients v_i^y are equal to zero (see App. C): this implies $\Delta \mathcal{M}^{nBorn}(h, \hat{y}) = 0$ and only five GPs can in this case be extracted.

Measuring also out-of-plane ($\phi \neq 0$) all the six independent GPs are accessible.

Chapter 3

Theoretical and Experimental Status

All truths are easy to understand once they are discovered;
the point is to discover them.

Galileo Galilei

In this chapter we describe the actual status of the theoretical and experimental knowledge of virtual Compton scattering and the generalized polarizabilities. Quite a few models of the nucleon were able to predict the GPs and a short review of them with their results will be given.

At the time of writing three experiments have measured the unpolarized VCS cross section, while one experiment for the measurement of the single spin asymmetry was performed.

As shown in the last chapter, only a double polarization experiment has the potential to disentangle all the generalized polarizabilities: the first experiment of this kind is the subject of this work.

3.1 Theoretical Models and Predictions

In the following we give a summary of the various models used to predict the GPs. As a check for the validity of the model, we cite also the results obtained for the electromagnetic polarizabilities α and β while the results for the GPs are summarized later.

3.1.1 Non Relativistic Quark Model

In [10] the first attempt to calculate the generalized polarizabilities was carried out within the framework of a non relativistic quark model and in [11] the calculation was further improved. The constituent quark dynamics is described by the Schrödinger equation with Hamiltonian

$$H_{nRQM} = \sum_{i=1}^{i=3} -\frac{\nabla_i^2}{2m_q} + V(r) \quad (3.1)$$

The interaction with the photon field is fixed by requiring the gauge invariance of the Schrödinger equation and the potential $V(r)$ is harmonic for assuring confinement.

The constituent quark masses $m_q = m_u = m_d$ are chosen in order to reproduce the proton magnetic moment and the harmonic oscillator energy $\hbar\omega$ is tuned for reproducing the hadron spectrum. In the constituent quark model exists a relation between the harmonic oscillator frequency and the proton mean square radius: $\langle r^2 \rangle = \hbar/(m_q\omega)$. The problem, which reflects the approximation of this description of the nucleon, is that with the chosen ω , the mean square radius comes out about two times smaller than the experimental value of $\langle r^2 \rangle_{exp} \approx 0.86$ fm. In order to better comprehend the results of this model, it is worth to look at the predictions about the electric and magnetic polarizabilities.

$$\bar{\alpha} = 2\frac{e^2 \langle r^2 \rangle}{4\pi 3\hbar\omega} + \frac{e^2 \langle r^2 \rangle}{4\pi 3m_p} \simeq 6.6 \cdot 10^{-4} \text{fm}^3 \quad (3.2)$$

$$\bar{\beta} = 2\frac{e^2 \left| \frac{2\sqrt{2}}{3}\mu_p \right|^2}{m_\Delta - m_p} - \left(\frac{e^2 \langle r^2 \rangle}{4\pi 6m_p} + \frac{e^2 \langle d^2 \rangle}{4\pi 2m_p} \right) \simeq 4.0 \cdot 10^{-4} \text{fm}^3. \quad (3.3)$$

The electric polarizability is dominated by the first negative parity resonance in the transition E1; the magnetic polarizability is dominated by the $N \rightarrow \Delta$ transition M1. These values are either too small ($\bar{\alpha}$) or too big ($\bar{\beta}$) when compared with the experimental results.

This model does not consider the pion as a fundamental degree of freedom in the nucleon at low energy. The presence of the pion cloud implies, with a classical analogy, induced currents in opposition to the applied field and this translates in a strong diamagnetic effect that should be added to the paramagnetic effect given by the Δ transition.

In fact this model does not take into account other important physical aspects, like relativity and chiral symmetry.

3.1.2 Linear σ -Model

The linear sigma model (LSM) contains all the relevant symmetries in the non perturbative regime of hadron physics, namely Lorentz invariance, gauge invariance, chiral invariance and also the PCAC¹ relation is satisfied. The fundamental fields of the LSM lagrangian are the nucleon, the pion and the σ fields. The coupling constant between pions and nucleons $g_{\pi N}$ is given through the Treiman-Goldberger relation [18] [19]

$$g_{\pi N} = g_A \frac{m_N}{F_\pi} \simeq 12.7 \pm 0.1, \quad (3.4)$$

where $g_A \simeq 1.26$ and $F_\pi \simeq 93.3 \text{MeV}$ are respectively the axial coupling constant and the pion decay constant.

In [16] the generalized polarizabilities were calculated using the linear sigma model and here we report the result for the polarizabilities:

¹Partially Conserved Axial-Vector Current [17]

$$\bar{\alpha} = \frac{e^2 g_{\pi N}}{192\pi^3 m_N^3} \left[\frac{5\pi}{2\mu} + 18 \ln \mu + \frac{33}{2} + \mathcal{O}(\mu) \right] \simeq 7.5 \cdot 10^{-4} \text{fm}^3 \quad (3.5)$$

$$\bar{\beta} = \frac{e^2 g_{\pi N}}{192\pi^3 m_N^3} \left[\frac{\pi}{4\mu} + 18 \ln \mu + \frac{63}{2} + \mathcal{O}(\mu) \right] \simeq -2.0 \cdot 10^{-4} \text{fm}^3. \quad (3.6)$$

Within this model, an excess of paramagnetic contribution due to the pion cloud is present, because the $N \rightarrow \Delta$ transition is not considered.

3.1.3 Heavy Baryon Chiral Perturbation Theory

Heavy Baryon Chiral Perturbation Theory (HB χ PT) is an effective field theory of QCD which provides a systematic way in order to make predictions at low energies [21]. The effective lagrangian of HB χ PT is constructed using the chiral symmetry $SU(3)_L \times SU(3)_R$. This symmetry is then spontaneously broken down to $SU(3)_V$, giving rise to eight Goldstone bosons interpreted as the eight pseudoscalar mesons known from phenomenology. The mass of the Goldstone bosons is generated by introducing an explicit symmetry breaking term due to the non zero quark masses. In principle, the lagrangian of an effective theory can have infinite terms: it is sufficient that they are consistent with the symmetries considered. As an example, the lagrangian (in the purely pionic sector) can be organized as

$$\mathcal{L} = \mathcal{L}_2 + \mathcal{L}_4 + \mathcal{L}_6 + \dots, \quad (3.7)$$

where the index indicates the number of derivatives and quark mass terms. This translates, using the power counting language, in a specific order of a small quantity p , where p can be a mass or a momentum ($\mathcal{O}(p^2)$, $\mathcal{O}(p^4)$, ..). In a lagrangian containing also baryon fields, odd orders are allowed (like \mathcal{L}_3). Like in other perturbative calculations, the order of the expansion for a certain observable is always indicated. The six GPs were calculated for the first time to order $\mathcal{O}(p^3)$ in [22]. In [23], the 4 spin-GPs were calculated at $\mathcal{O}(p^4)$. Regarding the electromagnetic polarizabilities, the results of HB χ PT at $\mathcal{O}(p^4)$ [24] comprehending the treatment of the Δ resonance are

$$\bar{\alpha} = 10.5 \pm 2 \cdot 10^{-4} \text{fm}^3, \quad (3.8)$$

$$\bar{\beta} = 3.5 \pm 1.5 \cdot 10^{-4} \text{fm}^3. \quad (3.9)$$

At $\mathcal{O}(p^3)$ the result [25] is the same as for the linear σ -model up to the terms $1/\mu$.

3.1.4 Effective Lagrangian Model

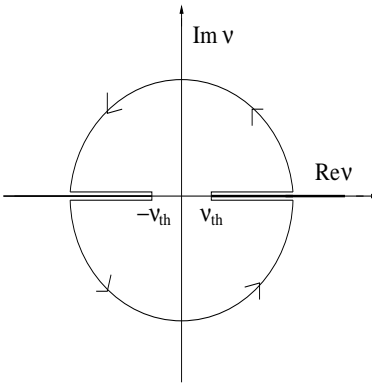
The Effective Lagrangian Model (ELM) is a phenomenological approach developed in [20] using a relativistic formalism. The calculation considers the main intermediate states that contribute to the non-Born term summing all the corresponding Feynman diagrams. The considered resonances are $\Delta(1232)$, $P_{11}(1440)$, $D_{13}(1520)$,

$S_{11}(1535)$, $S_{13}(1620)$, $S_{11}(1650)$ and $D_{33}(1700)$. The coupling of the resonances is adjusted on the experimental results of $N\gamma$ reactions. The predicted values for the polarizabilities are

$$\begin{aligned}\bar{\alpha} &= 7.3 \cdot 10^{-4} \text{fm}^3, \\ \bar{\beta} &= 1.6 \cdot 10^{-4} \text{fm}^3.\end{aligned}\quad (3.10)$$

3.1.5 Dispersion Relation Model

In analogy with what was already done in the case of real Compton scattering, in [26] the dispersion relation (DR) formalism is developed in the case of VCS, deriving predictions for the GPs. The DR formalism uses the Cauchy's integral formula for connecting the real and the imaginary part of the scattering amplitudes:

$$\text{Re}F_i^{nB}(Q^2, \nu, t) = \frac{2}{\pi} \int_{\nu_{th}}^{+\infty} d\nu' \frac{\nu' \text{Im}F_i(Q^2, \nu', t)}{\nu'^2 - \nu^2}$$


Introducing the Mandelstam invariant variables as

$$s = (q + p)^2 \quad t = (q - q')^2 \quad u = (q - p')^2 \quad \text{with} \quad s + t + u = 2M^2 - Q^2,$$

the integration variable $\nu = \frac{s-u}{4M}$ is defined to symmetrize the crossing $s \leftrightarrow u$. The cut on the real axis starts from a value that corresponds to the pion production threshold.

The imaginary part contains informations about the resonance spectrum of the nucleon; in particular the amplitudes of the MAID model [27] for $\gamma^{(*)}N \rightarrow N\pi$ are used.

The GPs are connected to the scattering amplitudes, so using the DR integrals, predictions can be made. Not all the GPs can be extracted from this calculation: for example, the Q^2 evolution of the electric and magnetic polarizabilities should be parameterized. The authors in [26] choose arbitrarily a dipole parameterization

$$\alpha(Q^2) - \alpha^{\pi N}(Q^2) = \frac{\alpha(0) - \alpha^{\pi N}(0)}{(1 + Q^2/\Lambda_\alpha^2)^2}, \quad (3.11)$$

where $\alpha^{\pi N}(Q^2)$ comes from dispersion integrals of πN states (an analogue form is valid in the case of β). The parameter Λ_α (and Λ_β for β) should be fitted to the experimental data. An advantage of this method is its capability to derive predictions also above pion threshold and to make no use of the low energy expansion: in principle, all the orders are taken into account.

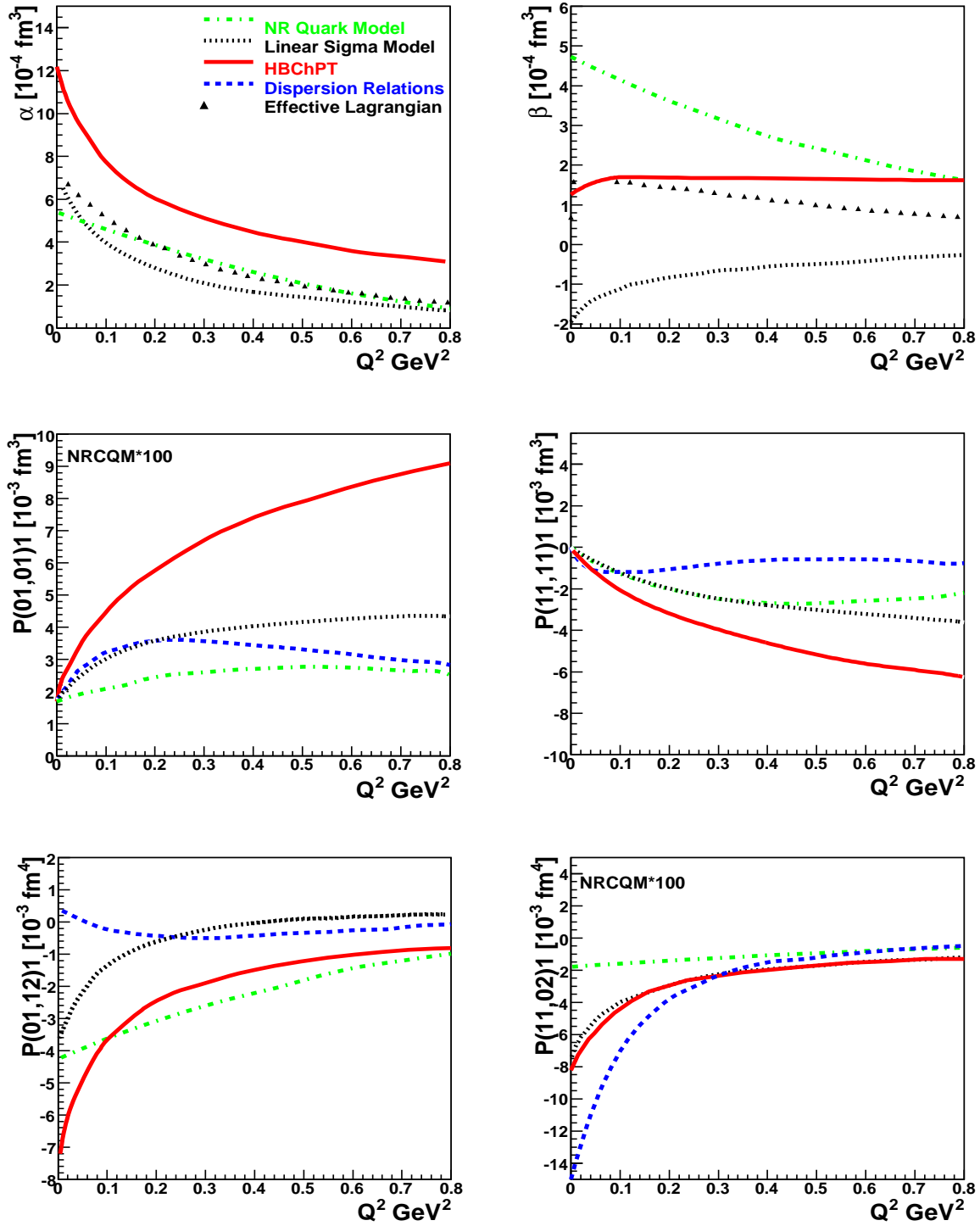


Figure 3.1: Theoretical models for the Generalized Polarizabilities. For the generalized electric (α) and magnetic (β) polarizabilities also the result of the effective lagrangian model is present, while the dispersion relation model is shown only for the “spin” GPs. Note that in two figures, the quark model predictions have been rescaled by a factor 100 for better comparison.

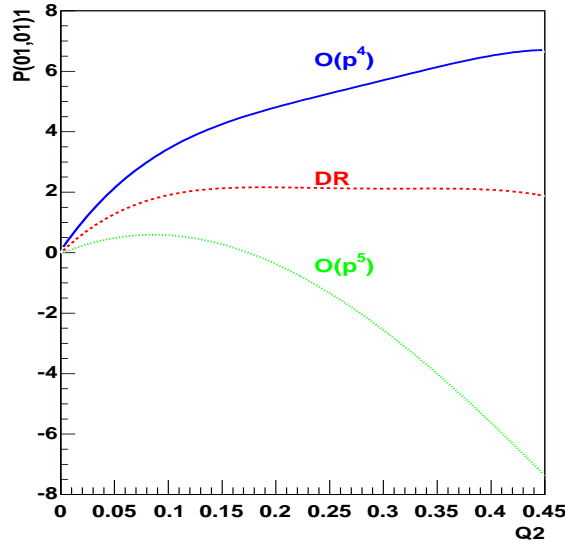


Figure 3.2: Calculation of $P^{(01,01)1}$ with HB χ PT at $\mathcal{O}(p^4)$ and $\mathcal{O}(p^5)$ compared with the DR model [35].

3.2 Summary on the Theoretical Predictions

Many theoretical models predict the behavior of the GPs as a function of Q^2 . All the available predictions are summarized in Fig. 3.1 for the chosen six independent GPs. As it is clear from the figure, the models of the nucleon give in some cases very different results: an experiment for clarifying the situation is then needed. The measurement of the generalized polarizabilities can give a better insight into the nucleon structure and the physical content of the models describing it. The models emphasize different aspects and degrees of freedom of the nucleon. For example, constituent quark models totally ignore pion cloud effects, while other models do not take into account the resonance spectrum. In particular the behavior of the generalized magnetic polarizability points towards two regions of the nucleon with diamagnetic and paramagnetic character. The diamagnetic response is explained by the pion cloud surrounding a core with paramagnetic character, given by the resonance structure of the nucleon. In the next chapter also experimental details will be given supporting this interpretation. The need of an experiment for measuring separately the GPs is also evident in the results of HB χ PT [35] where three spin GPs are calculated at $\mathcal{O}(p^4)$ and the fourth ($P^{(01,01)1}$) at $\mathcal{O}(p^5)$. The calculation needs no new low energy constants and thus it is an absolute prediction for these quantities. In Fig. 3.2 the calculations at $\mathcal{O}(p^4)$ and $\mathcal{O}(p^5)$ for $P^{(01,01)1}$ are shown in comparison with the dispersion relation model: the convergence of the perturbative expansion of this observable is still not reached. In the case of the other three spin GPs, the effect is not so dramatic: in fact the $\mathcal{O}(p^4)$ calculation is closer to the phenomenological estimation of the DR model in respect to the $\mathcal{O}(p^3)$ results [22], but a discrepancy still remains. Concerning theoretical improvements, calculations at $\mathcal{O}(p^4)$ of all the generalized polarizabilities in covariant χ PT are in progress [36].

3.3 Present Experimental Status

At the time of writing, three unpolarized VCS experiments in three different laboratories were performed: MAMI [6] ($Q^2 = 0.33\text{GeV}^2$) and MIT Bates [34] ($Q^2 = 0.06\text{GeV}^2$) below pion threshold and also above pion threshold at JLab [31] ($Q^2 = 0.92, 1.76\text{GeV}^2$). Only one experiment done at MAMI exists concerning the low energy single spin asymmetry. The first double polarization measurement under pion threshold, also performed at MAMI, is the subject of this work.

3.3.1 Unpolarized Virtual Compton Scattering

The measurement of the unpolarized cross section gives access to the combination $\Psi_0 = v_{LL} [P_{LL}(q) - \frac{1}{\epsilon}P_{TT}] + v_{LT}P_{LT}(q)$ of structure functions. Furthermore, if the angular range in $\theta_{\gamma\gamma}$ is large enough the two different contributions ($P_{LL} - \frac{1}{\epsilon}P_{TT}$) and P_{LT} can be separated with a Rosenbluth technique [62]. Subtracting the known Bethe-Heitler and Born contributions to the experimental cross section, under the validity of the low energy theorem, Ψ_0 can be measured: plotting Ψ_0/v_{LT} against v_{LL}/v_{LT} for each bin in $\theta_{\gamma\gamma}$, the resulting points should lie on a line. With a linear fit ($P_{LL} - \frac{1}{\epsilon}P_{TT}$) and P_{LT} are extracted.

Another way for analyzing the unpolarized cross section is to use the dispersion relation formalism which, above the pion production threshold, is at the moment the unique existing theoretical tool that can be used. The parameters of the dispersion relation model are fitted to the experimental cross sections and a prediction for the four spin GPs is given.

MAMI Experiment

The first unpolarized VCS experiment under pion threshold was performed at MAMI between 1996 and 1997 [6]. In this experiment, $d\sigma^5$ was measured for five values of the photon momentum q' : 33.6, 45.0, 67.5, 90.0, 111.5 MeV/c. Two kinematical variables were fixed: the virtual photon momentum ($q = 600 \text{ MeV}/c$, $\tilde{Q}^2 = 0.33 \text{ GeV}^2$) and the polarization ($\epsilon = 0.62$). The scattered electron and the recoiling proton are detected in coincidence by two high-resolution spectrometers. In Fig. 3.3 the results for the cross section are presented and the deviation from the BH+B calculation with increasing q' is clearly visible. In the same figure, also the Rosenbluth separation based on the low energy theorem ansatz is shown. In the analysis, the form factor parameterization of Höhler *et al.* was used [42]. A direct check for the validity of the LEX was performed in this experiment for the first time: in Fig. 3.4 the quantity Ψ_0 is plotted as a function of q' for each bin in $\theta_{\gamma\gamma}$ showing no appreciable dependence. This result permits the application of the LEX approach and Ψ_0 can then be averaged over q' without the use of extrapolations. The final results for ($P_{LL} - \frac{1}{\epsilon}P_{TT}$) and P_{LT} are reported in table 3.1 and Fig. 3.5. The results are found in good agreement with the predictions of HB χ PT at order $\mathcal{O}(p^3)$ [22].

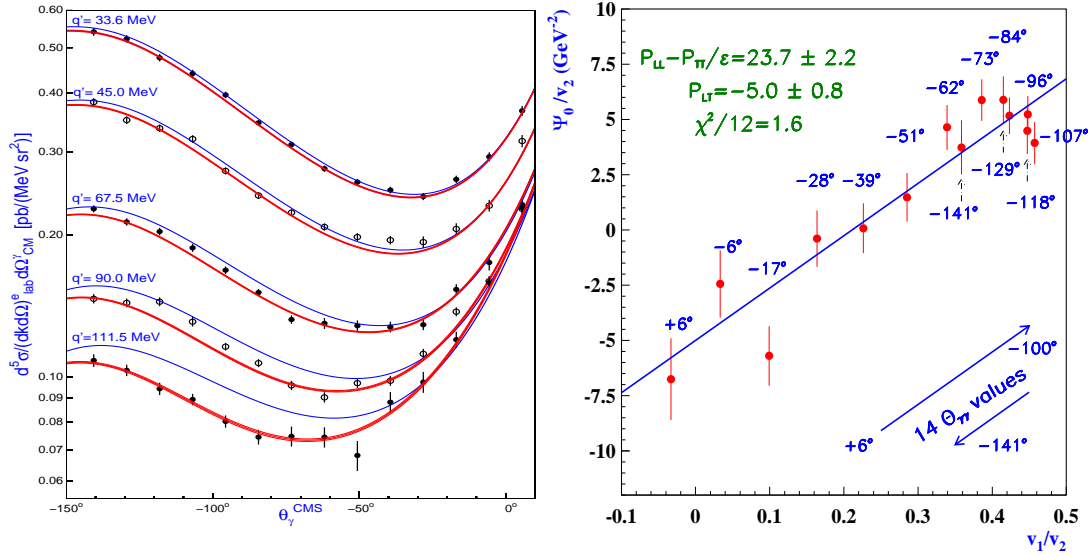


Figure 3.3: (Left) Cross sections measured at MAMI and published in [6]. Measurements at five different q' values are shown. (Right) Rosenbluth separation of the structure functions based on the LEX approach.

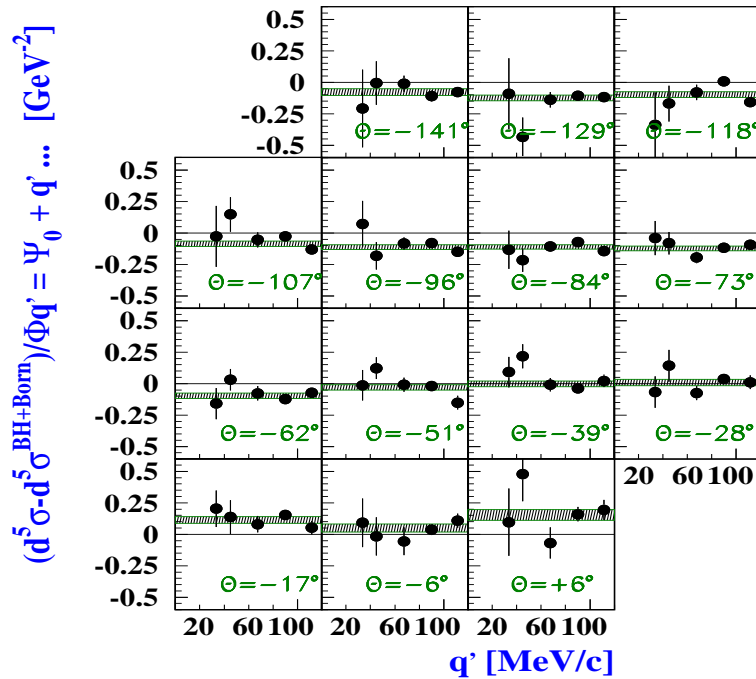


Figure 3.4: Evolution of Ψ_0 as a function of q' which proves the validity of the LEX approach for the considered kinematics.

Jefferson Lab Experiment

In 1998 at the Jefferson Laboratory² (JLab) the Hall A Collaboration has measured with a 4.030 GeV² electron beam the VCS cross section [31].

Two high-resolution spectrometers are used to detect in coincidence the scattered

²Thomas Jefferson National Accelerator Facility, Newport News, VA 23606

Experiment	Q^2 (GeV ²)	ϵ	$(P_{LL} - \frac{1}{\epsilon}P_{TT})$ (GeV ²)	P_{LT} (GeV ²)
TAPS [30]	0		$81.3 \pm 2.0 \pm 3.4$	$-5.4 \pm 1.3 \pm 1.9$
Low Energy Th. Analyses				
MIT-Bates [34]	0.06	0.90	$54.5 \pm 4.8 \pm 2.0$	-
MAMI [6]	0.33	0.62	$23.7 \pm 2.2 \pm 4.3$	$-5.0 \pm 0.8 \pm 1.8$
JLab I-a [31]	0.92	0.95	$1.77 \pm 0.24 \pm 0.70$	$-0.56 \pm 0.12 \pm 0.17$
JLab II [31]	1.76	0.88	$0.54 \pm 0.09 \pm 0.20$	$-0.04 \pm 0.05 \pm 0.06$
Dispersion Relation Analyses				
MIT-Bates	0.06	0.90	$46.7 \pm 4.9 \pm 2.0$	$-8.9 \pm 4.2 \pm 0.8$
JLab I-a [31]	0.92	0.95	$1.70 \pm 0.21 \pm 0.89$	$-0.36 \pm 0.10 \pm 0.27$
JLab I-b [31]	0.92	0.95	$1.50 \pm 0.18 \pm 0.19$	$-0.71 \pm 0.07 \pm 0.05$
JLab II [31]	1.76	0.88	$0.40 \pm 0.05 \pm 0.16$	$-0.09 \pm 0.02 \pm 0.03$

Table 3.1: Experimental results from the available unpolarized cross section measurements. In the first line, the TAPS experiment on real Compton scattering is also reported. The other results are from MIT-Bates, MAMI and JLab experiments.

electron and the recoiled proton. The two kinematics used have as fixed parameters $Q^2 = 0.92, 1.76$ GeV² and $\epsilon = 0.95, 0.88$ respectively. The used form factor parameterization is that of Brash et al. [33].

In this experiment both the LEX and dispersion relation formalism are used for extracting the structure functions: the dispersion relation approach can also make use of the events above pion threshold. The results of the experiment are reported in table 3.1 while in Fig. 3.5 they are confronted with the other experiments. The LEX and dispersion analyses are found to be consistent within error bars.

MIT-Bates Experiment

Between 2000 and 2001 an unpolarized VCS experiment [34] was done at the Bates Linear Accelerator Center using the OOPS (Out Of Plane Spectrometer) system. The used kinematics implied a final photon impulse of 43, 65, 84, 100 and 115 MeV/c.

The data were taken simultaneously at different out-of-plane angles: 90°, 180° and 270° at fixed $\theta = 90^\circ$. For the setups with out-of-plane angles 90° and 270° only the structure function $P_{LL} - (1/\epsilon)P_{TT}$ is measurable (due to the kinematical coefficients involved, see App. C).

The data are analyzed with two methods: the low energy expansion and the dispersion relation model. For the first time, a difference in the two methods is evidenced, at least in the in-plane measurement, in the extraction of the structure function P_{LT} (Fig. 3.5). The disagreement comes from the near cancellation of the electric and magnetic polarizabilities at order $\mathcal{O}(q')$ for the in-plane kinematics. The polarizability effect is then predominantly quadratic in q' and the LEX analysis is valid only in the case of a linear effect. On the contrary, in principle the dispersion relation

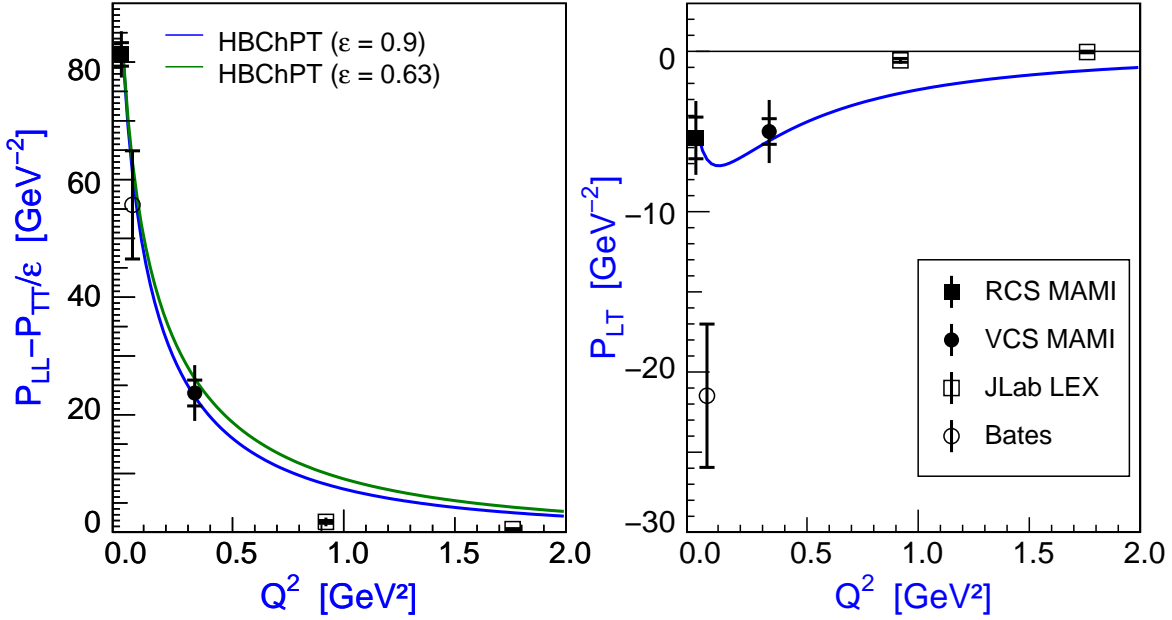


Figure 3.5: Experimental results for the structure functions extraction from the unpolarized cross section. The experimental points are confronted with the $\text{HB}\chi\text{PT}$ predictions. The square indicates the real photon point, the open circle the MIT-Bates result, the full circle the MAMI result. The other points at higher Q^2 are the JLab measurements.

approach contains all the orders up to the $\pi\pi N$ threshold.

Due to the very low Q^2 , it was also possible to measure the mean square electric polarizability radius using a dipole fit to the real Compton scattering point and the Bates result. The measured values are $\langle r_\alpha^2 \rangle = 1.95 \pm 0.33 \text{fm}^2$ and $\langle r_\beta^2 \rangle = -1.91 \pm 2.12 \text{fm}^2$, in good agreement with the $\text{HB}\chi\text{PT}$ prediction of $\langle r_\alpha^2 \rangle = 1.7 \text{fm}^2$ and $\langle r_\beta^2 \rangle = -2.4 \text{fm}^2$.

3.3.2 Single Spin Asymmetry

Another interesting observable which can be measured with the VCS reaction is the so called Single Spin Asymmetry (SSA), defined as

$$\mathcal{A} = \frac{\mathcal{M}(\xi^e) - \mathcal{M}(-\xi^e)}{\mathcal{M}(\xi^e) + \mathcal{M}(-\xi^e)} \quad (3.12)$$

It is possible to measure this observable exploiting the high degree of beam polarization available at modern electron scattering facilities.

Because of time reversal invariance and up to α_{QED} corrections, \mathcal{A} is different from zero only above pion threshold and also if the reaction and the hadronic plane do not coincide ($\varphi \neq 0$).

This observable is sensitive to the imaginary part of the VCS amplitude, since the numerator of 3.12 is proportional to $\text{Im}(T^{VCS}) \cdot \text{Re}(T^{VCS} + T^{BH})$: as can be seen also an interference term with the Bethe-Heitler amplitude is present, which has the effect of enhancing the asymmetry. Below pion threshold the VCS amplitude is

purely real, but above it acquires an imaginary part due to the coupling to the πN channel.

The measurement of this quantity was performed at MAMI in 2002/03 [39] at $Q^2 = 0.35 \text{ (GeV/c)}^2$ in the $\Delta(1232)$ resonance region and at a center of mass energy $W \sim 1.2 \text{ GeV}$.

In this experiment the VCS reaction $ep \rightarrow ep\gamma$ was detected simultaneously with the pion electroproduction reaction $ep \rightarrow ep\pi^0$: in this way the single spin asymmetry can be extracted for both reactions. In Fig. 3.7 and 3.8 the results with the theoretical prediction of the dispersion relation model are shown. The DR model uses the MAID2003 parameterization for the multipoles and also the sensitivity to the free parameters Λ_a and Λ_b is shown

In Fig. 3.9 the results regarding the SSA for the pion electroproduction channel are shown. They complement other analogous measurements already performed at MAMI at different kinematical points [37], [38]. The agreement with the MAID and DTM models is good up to 20° , then the data suggest the presence of a structure which is not reproduced by any model, but it can indicate some effect of other high-order multipoles; in any case, the signal of such a structure has a very low statistical significance. The SSA amounts to few percents and there is a qualitative agreement with the models.

The dispersion relation model calculates the real amplitude starting from the imaginary one. The imaginary amplitude is obtained through its unitary relation to the pion photo- and electroproduction amplitudes which are given by the MAID model [27]. MAID is a phenomenological model fitted to the pion production data where a large experimental dataset for $Q^2 = 0$ is available. For $Q^2 > 0$, which is the case of VCS, there is only few experimental data available. The experiment represents then an important check for MAID and the dispersion relation model, because the imaginary part of the amplitude is in this case directly measured.

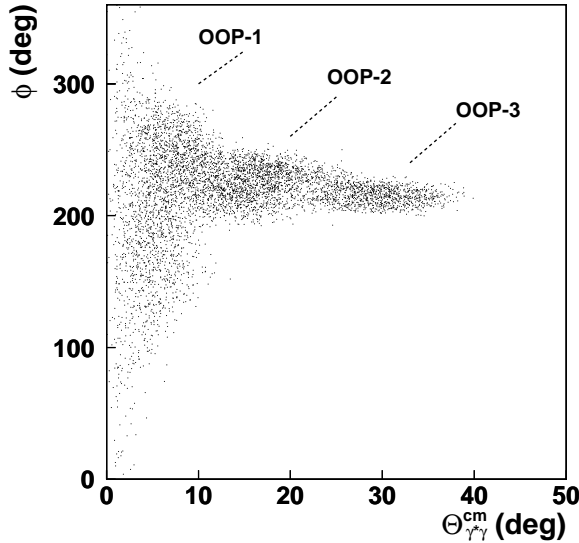


Figure 3.6: The measured phase space as a function of the azimuthal and polar angles.

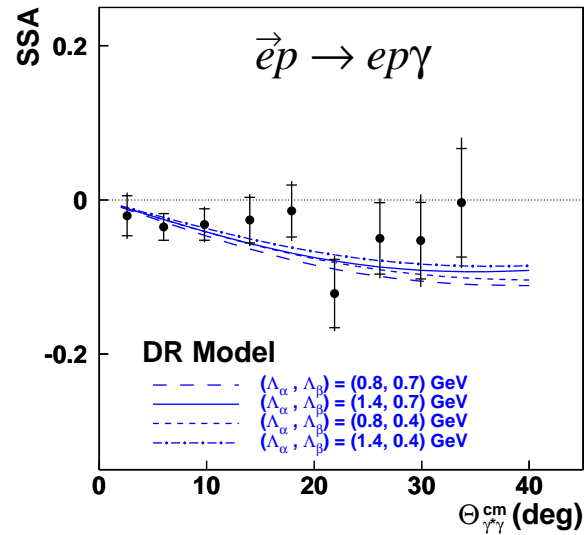


Figure 3.7: Dispersion relation model (DR) predictions for the VCS reaction above threshold.

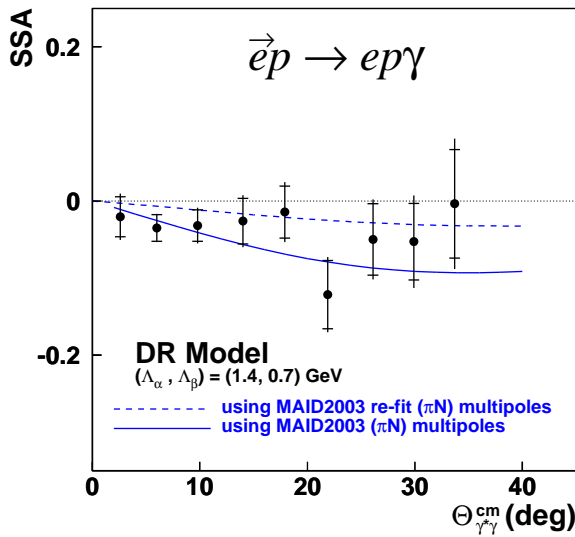


Figure 3.8: Sensitivity of the DR model to the MAID πN multipoles

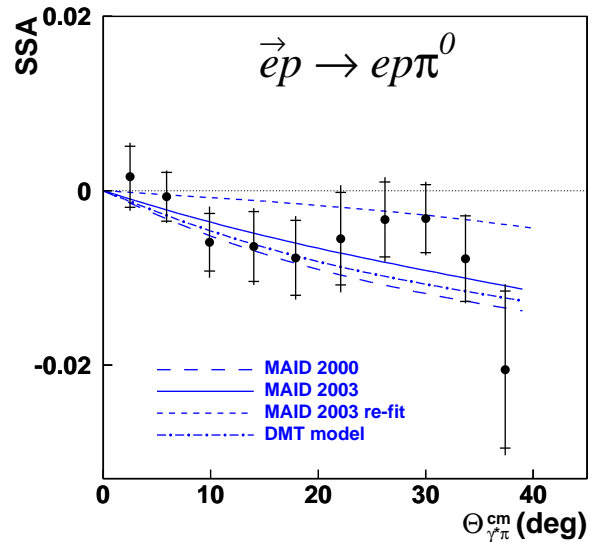


Figure 3.9: SSA π^0 electroproduction compared to the MAID and DMT models

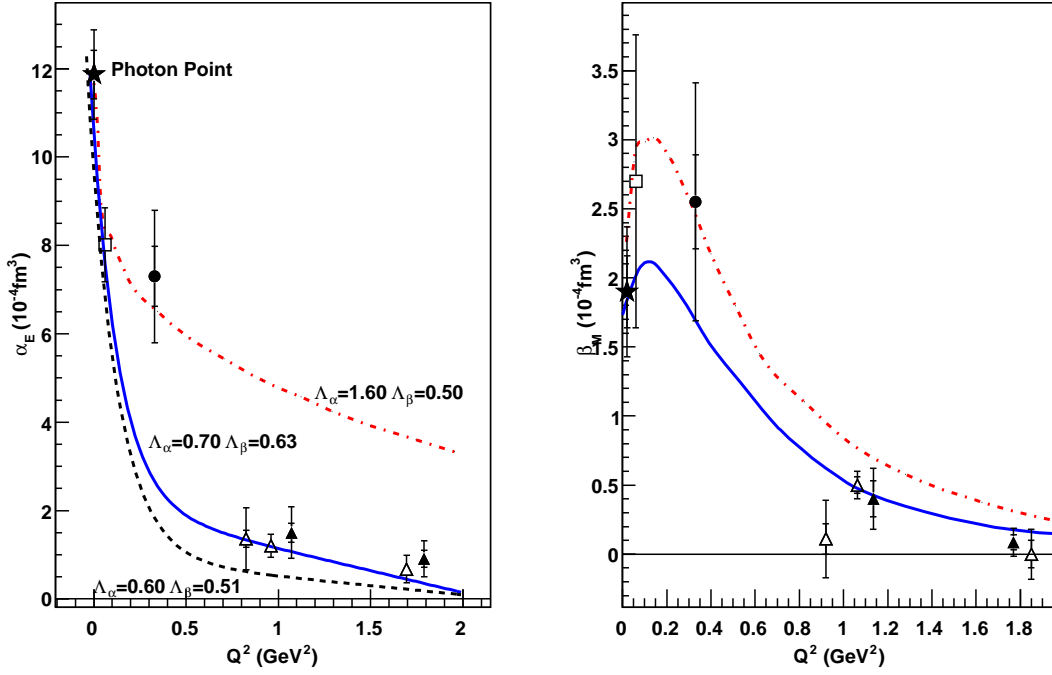


Figure 3.10: World dataset for the electric and magnetic generalized polarizabilities extracted using the dispersion relation model. The real photon point is indicated with a star. The square point corresponds to the MIT-Bates analysis, while the circle and the triangles are from MAMI and JLab respectively. Full markers indicate the use of LEX in the structure function extraction, while open markers indicate the use of dispersion relations.

3.4 Summary on the Experimental Status

The experimental situation up to now (2007) is the following: two unpolarized experiments were done below pion threshold, while some measurements by JLab above threshold are available. The results below pion threshold were analyzed using both the LEX and the dispersion relations approach, while above threshold only the dispersion relation approach can be used.

For the single spin asymmetry only one experiment is available from MAMI: this measurement gives direct access to the imaginary part of the VCS amplitude which is not zero only above pion threshold.

The actual status of the measurements permits the extraction of two combinations of the generalized polarizabilities: $(P_{LL} - \frac{1}{\epsilon} P_{TT})$ and P_{LT} .

These combinations are dominated from the electric $\alpha_E(Q^2)$ and magnetic $\beta_M(Q^2)$ polarizabilities which can be extracted in a model dependent way with the dispersion relation model. This model predicts the spin polarizabilities while the electric and magnetic GPs are modeled by a dipole-like shape and the dipole parameters Λ_α and Λ_β are fitted to the data. Having fitted Λ_α and Λ_β all the spin GPs are fixed and the prediction can be used for calculating $\alpha_E(Q^2)$ and $\beta_M(Q^2)$. The available world experimental results are shown in Fig. 3.10 together with different fits of the

dispersion relation model. There is no combination of Λ_α and Λ_β which can reproduce all the available experimental data. The effect is more visible in the case of $\alpha_E(Q^2)$.

The magnetic polarizability shows a more complex behavior as a function of Q^2 suggested also by the data which indicates the existence of two different regions inside the nucleon: an internal one (larger momenta) with paramagnetic character, arising mainly from the nucleon resonances contribution, and a diamagnetic one at larger distances (lower momenta) which is interpreted as the action of the pion cloud.

The pion cloud interpretation is also strengthened by the mean square electric polarizability result which is larger than the mean square electric radius of $0.757 \pm 0.014 \text{fm}^2$. The result is also consistent with the uncertainty principle estimate of 2fm^2 for the pion cloud extension.

The difficulty of the dispersion relation model to describe the data can be ascribed to a not optimal parameterization of the electric and magnetic GPs because the single dipole shape is totally arbitrary: in the contributions to $\alpha_E(Q^2)$ there are also the ηN and $\pi\pi N$ channels which have resonances like $S_{11}(1535)$ and $D_{13}(1520)$ with transition form factors without a dipole shape [40] [41].

The behavior of $\beta_M(Q^2)$ is in any case remarkable and shows explicitly the interplay between different degrees of freedom inside the nucleon, making the generalized polarizabilities very interesting observables for testing theoretical models.

An explicit measurement of the single generalized polarizabilities will be of great interest to further clarify the validity of the theoretical models and thus our understanding of the nucleon structure: a double polarization experiment is an important step towards this direction.

Chapter 4

Accelerator and Experimental Setup

You see, but you do not observe.

Sir Arthur Conan Doyle
Sherlock Holmes,
A Scandal in Bohemia, 1892

4.1 Accelerator

The Mainz Institute for Nuclear Physics operates a continuous wave electron accelerator (**MAMI: MA**inz **MI**crotron) for experiments in nuclear and hadronic physics [43]. The accelerator consists of a cascade of three *Race Track Microtrons* (RTM). The microtrons are built with normal conducting accelerating cavities¹ placed between two high precision and homogeneity magnets allowing for multiple recirculation of the beam.

Electrons are produced by a thermoionic source with an energy of 100 kV. Alternatively, a polarized source can be used: polarized electrons are produced by photoelectric effect using polarized laser light on a GaAs crystal. Polarizations up to 80% can be achieved. After the source, a linac injects in the first microtron a beam with energy of 3.5 MeV which is then raised to 14.9 MeV. The second and the third microtrons rise the energy to 180 MeV and 855 MeV respectively (see Fig. 4.1). The final beam has an energy spread of 30 keV (FWHM).

In Fig 4.2, the floor plan of the experimental and accelerator areas can be seen; a beam transport system delivers the MAMI beam to four experimental halls: A1 (electron scattering), A2 (experiments with real photons), A4 (parity violating electron scattering), X1 (experiments with X-rays).

A fourth stage [45], called MAMI C, was completed in 2007. For this stage, with a final energy of 1.5 GeV, a harmonic double sided microtron (HDSM) was designed: again, normal conducting cavities are used, but they are arranged in two antiparallel linacs and the recirculation is guaranteed by four combined function magnets with 45° bending. For longitudinal stability reasons, one of the two linacs is operated at double frequency in respect to the other. In the experiment described in this work, the polarized beam delivered by the third MAMI stage (MAMI B) was used with final energy of 855 MeV.

¹with frequency $\nu = 2449.53$ MHz

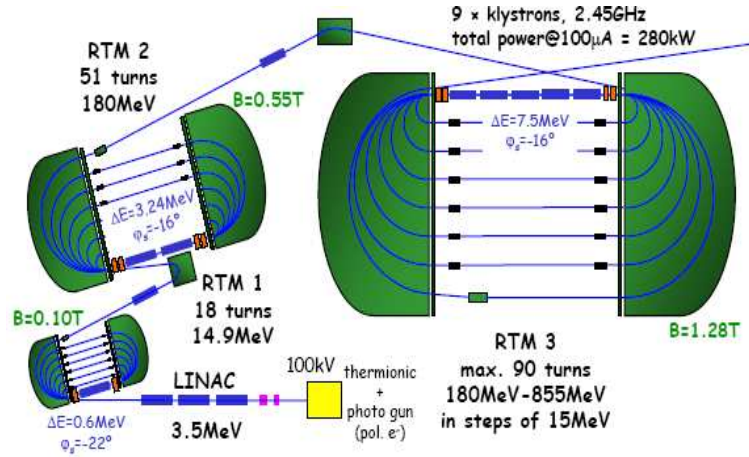


Figure 4.1: The MAMI accelerator complex. The fourth stage (MAMI C) is not shown. (Figure by A. Jankowiak).

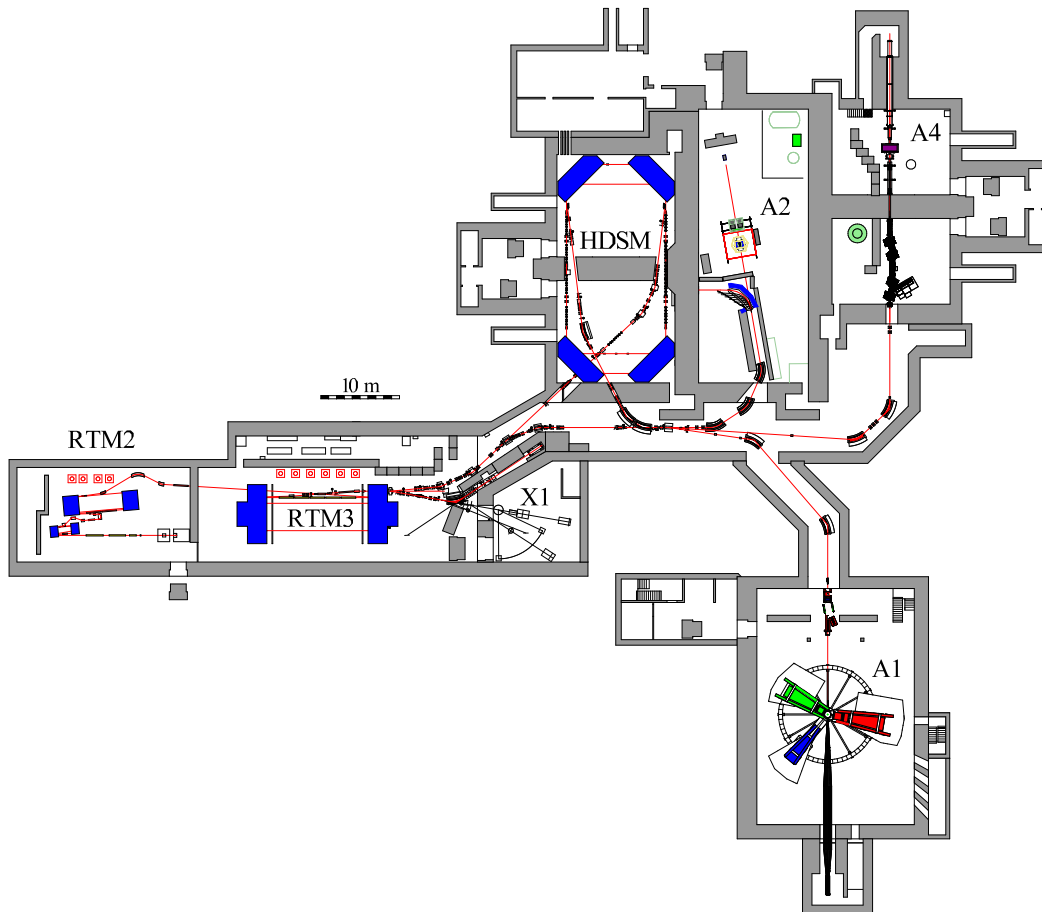


Figure 4.2: MAMI floor plan with the experimental areas of the A1, A2, A4, and X1 collaborations



Figure 4.3: The three Spectrometer Setup at MAMI

4.2 Experimental Setup

The A1 Collaboration runs at the Mainz Institute for Nuclear Physics a three spectrometer setup [44] for electron scattering experiments in nuclear and hadronic physics. In the following, an overview on the experimental setup is given.

4.2.1 Magnetic Spectrometers

In the A1 experimental hall, three high resolution spectrometers (called A, B, and C) are arranged around a target. The spectrometers are used for detection of charged particles escaping the target: particles scattered within the spectrometer acceptance are guided by the magnetic fields to the detection area which consists of different kinds of detectors: drift chambers, scintillators and Čerenkov detectors. Additionally in spectrometer A the Čerenkov detector can be substituted by a recoil proton polarimeter. The main spectrometer parameters are summarized in table 4.1.

Spectrometers A and C employ a Quadrupole-Sextupole-Dipole-Dipole magnetic op-

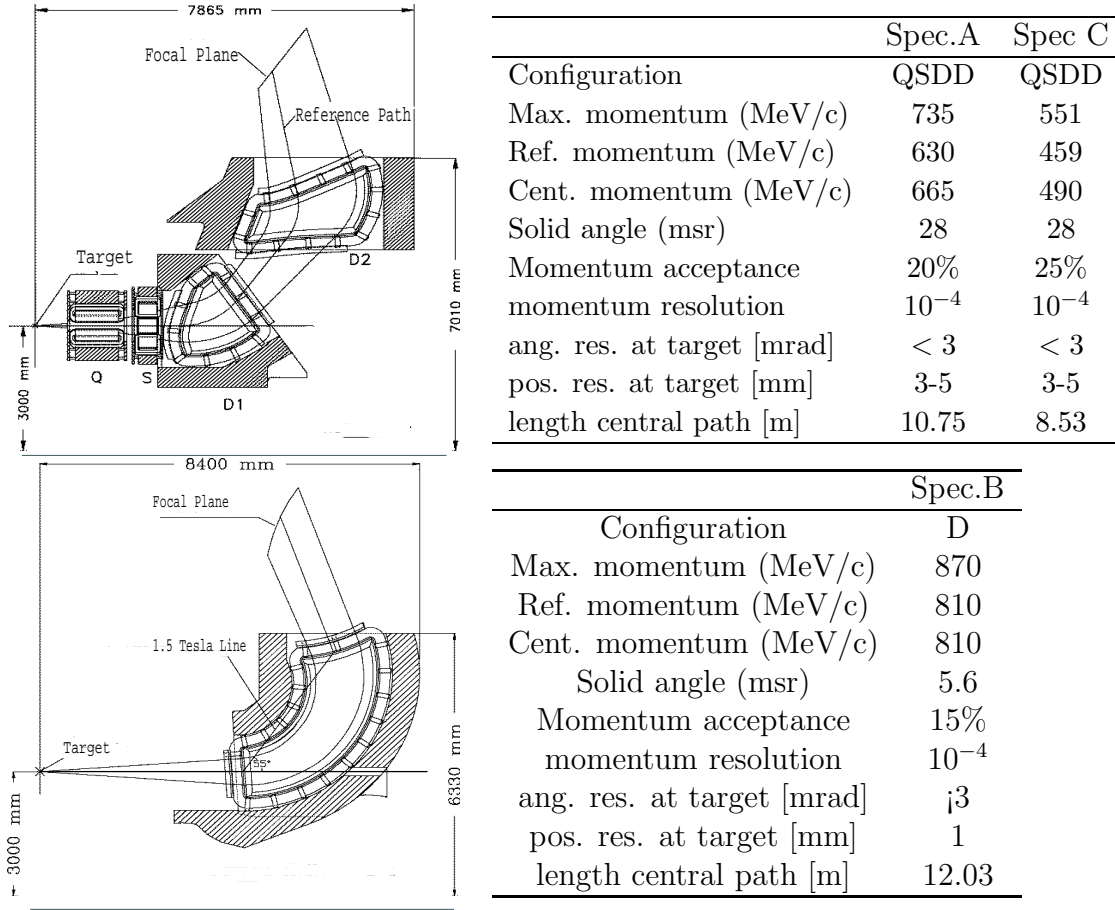


Table 4.1: Main parameters for the spectrometers A, B, and C

tics, in order to achieve a large acceptance. Spectrometer B uses a single clamshell dipole magnet. The optics of spectrometers A and C has point-to-point focusing in the dispersive plane ($(x_{fp}|\theta_0) = 0$): this ensures the independence of the x_{fp} coordinate at focal plane from the initial angle at target θ_0 , resulting in a high momentum resolution. In the non-dispersive direction the optics is parallel-to-point ($(y_{fp}|y_0) = 0$): this means that the y_{fp} coordinate at focal plane is insensitive to the initial y_0 position. The last property assures good angular resolution, but reduces the position resolution.

Spectrometer B optics is made by an unique dipole magnet (“clam-shell”) with point-to-point focusing in both planes. This construction permits to have a narrower spectrometer which can reach small scattering angles (down to 7°). This spectrometer can be also tilted for reaching out of plane angles up to 10° .

Drift Chambers and Coordinate Reconstruction

The standard detector package of each spectrometer (Fig. 4.4) consists of four vertical drift chambers (VDCs) triggered by a double layer of plastic scintillators. Two planes have wires in the non-dispersive direction, while the other two, in a diagonal

direction with 40° in respect to y_{fp} . The wires (200 up to 300 depending on the plane considered), with 5mm spacing between each other, are at ground potential, while the foils are set at negative potential (~ 5000 V). A gas mixture of argon/isobuthan is used.

The particles hit the VCDs with an average 45° angle to the normal of the plane, producing 5 average hits for each plane. The VDCs measure the particles coordinates in the focal plane which are then used for determining the target coordinates and the particle momentum. The focal plane coordinates (X, Θ, Y, Φ) measured by the drift chambers are connected to the target coordinates $(X_0, \Theta_0, Y_0, \Phi_0, Z_0, \delta)$ by the following parameterization

$$q = \sum_{ijklmn} \langle q | X_0^i \Theta_0^j Y_0^k \Phi_0^l Z_0^m \delta^n \rangle X_0^i \Theta_0^j Y_0^k \Phi_0^l Z_0^m \delta^n, \quad (4.1)$$

where $q \in (X, \Theta, Y, \Phi)$, $\delta = (p - p_{ref})/p_{ref}$ and p_{ref} is the reference momentum of the spectrometer.

The coefficients of the expansion are obtained with a measurement done with a special sieve-slit collimator placed at the spectrometer entrance [46]. The position of the holes in the collimator is known together with the corresponding target coordinates: in this way it is possible to reconstruct the coefficients which match the target coordinates with the coordinates measured in the focal plane. The final resolutions reported in table 4.1 are obtained with a spatial resolution in the drift chambers of $\leq 200\mu\text{m}$ in the dispersive plane and $\leq 400\mu\text{m}$ in the non dispersive plane.

Scintillators

Two segmented plastic scintillator planes serve as trigger for the whole acquisition system and for the drift chambers time determination. The scintillator signal is also used for realizing the coincidence between the spectrometers. Each plane has 15 segments (for each segment: 15×16 cm² for spectrometers A, C and 14×16 cm² for spectrometer B). The segmentation enhances the time resolution and gives also a rough information about the particle's position. The segments are coupled at each of the two sides to photomultipliers which are read in coincidence. The first plane (called dE) in respect to the particle's path is 3mm thick and is used for the energy loss determination, while the second plane with 10mm thickness (called ToF) is used for the time of flight measurement. Using the correlation of the energy losses in the two planes, particle identification can be done and minimum ionizing particles can be distinguished from protons.

Pions cannot be separated from electrons or positrons, and for this purpose, a Čerenkov detector is used.

Čerenkov Detector

Every spectrometer is equipped with a Čerenkov detector for particle identification. They are placed after the VDCs and the scintillator planes. The electrons (or

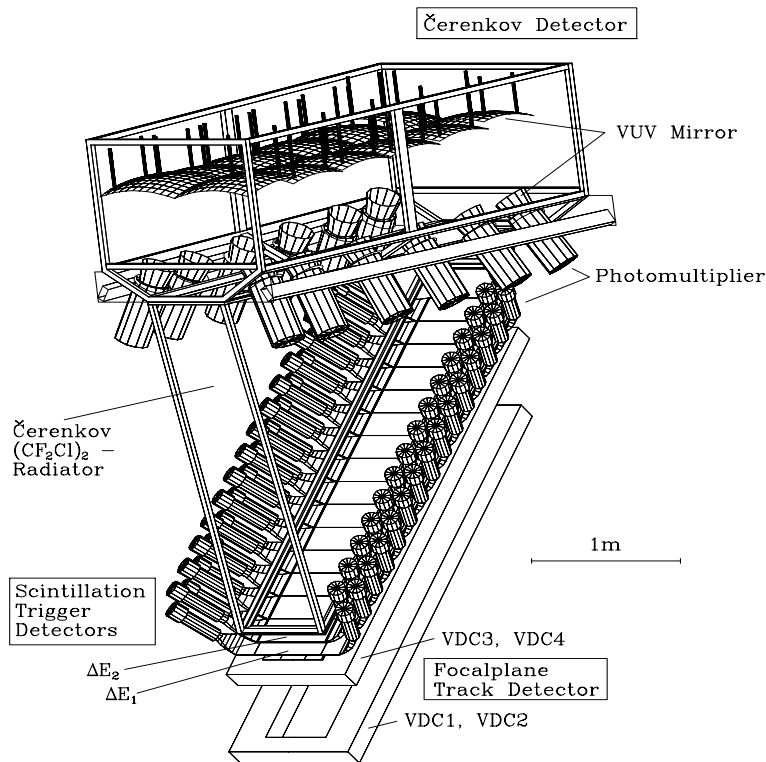


Figure 4.4: Detectors equipping each spectrometer: vertical drift chambers, two planes of segmented scintillators and a gas Čerenkov detector.

positrons) have a momentum threshold for Čerenkov radiation of about 10 MeV/c, pions have a threshold about 2.4 GeV/c. In the typical energy ranges of the experiments, only electrons entering the volume of the detector give rise to a signal². The produced Čerenkov radiation is reflected by mirrors back to photomultipliers generating the signal. The efficiency of the Čerenkov detectors is very close to 100%.

4.2.2 Target

The target consists of a vacuum vessel where the scattering material is placed. Various solid state materials, mounted on a ladder can be moved into the beam during experiments using remote control. Also a cryogenic target can be used (as in the experiment described in this work) for materials like hydrogen (H,D) or helium (He^4, He^3): the technique for cooling and liquefying them is based on two cooling loops. The first loop is based on a Philips compressor for liquefying hydrogen which is then transported to the target vessel by a transfer pipe. Inside the vessel there is the second cooling loop (“Basel-loop”) which contains the scattering material. The liquid hydrogen of the first loop cools the second one by a heat exchanger and a fan provides continuous recirculation (see Fig. 4.5). The temperature of the liquid hydrogen is raised in the heat exchanger and it is then transported back to the

²The radiator gas is Freon 114 with a refraction index of about 1.0013.

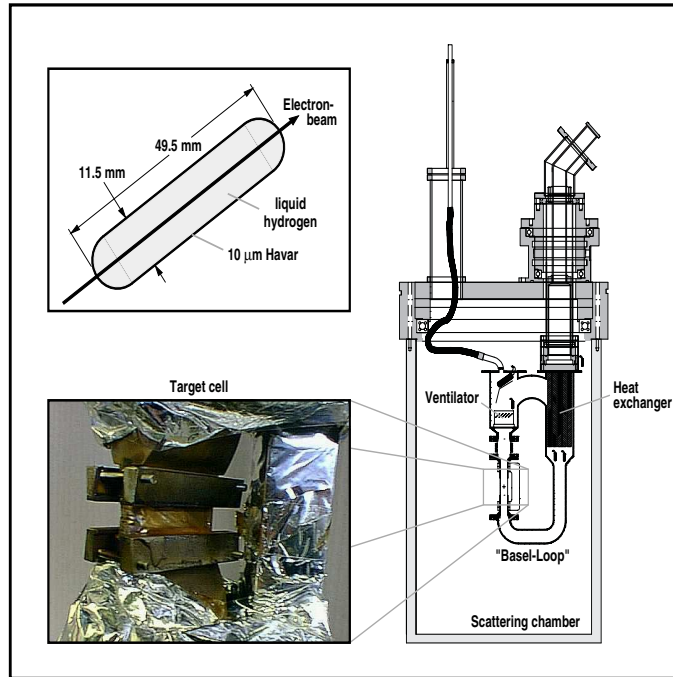


Figure 4.5: The target cell containing the liquefied gas is mounted in a scattering chamber. The hydrogen comes from the top and it is delivered by a compressor placed in the experimental hall. The target material is circulating in the “Basel-Loop” thanks to a ventilator (Figure from [49]).

Philips compressor. The Basel-loop is closed: it is filled with the scattering material at the beginning of the experiment and then it is maintained in the liquid phase by the first cooling loop.

In the Basel-Loop is placed the target cell which is 49.5mm long and made of a $10\mu\text{m}$ Havar walls. The geometry of the cell is optimized for enhancing the luminosity while keeping low the energy losses.

Temperature and pressure of the liquid are continuously measured and the beam is rastered in the transverse directions in order to keep temperature oscillations as small as possible avoiding local boiling of the liquid. The stability of the liquid phase is essential for a precise determination of the luminosity.

4.2.3 Proton Polarimeter

Since 1996, the A1 Collaboration operates a focal plane proton polarimeter [48], [49]. The polarimeter (FPP) is housed in spectrometer A, substituting, when needed, the Čerenkov detector, as shown in Fig. 4.6. The FPP consists of a carbon analyzer with variable width and of a detector package of four horizontal drift chambers (HDCs) for proton detection.

Protons are particles with spin $\frac{1}{2}$, and the spin vector can point in any direction \hat{d} . A projection of the spin vector onto an axis \hat{i} can have only two values, namely $\pm\frac{1}{2}$.

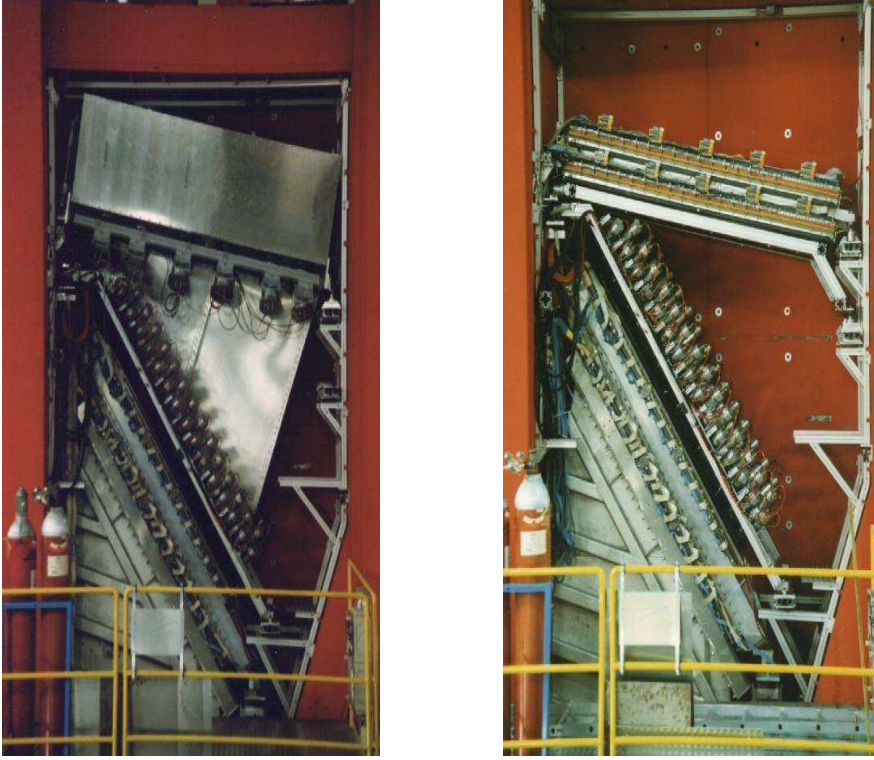


Figure 4.6: In the left figure, the detector package of spectrometer A is visible. The Čerenkov detector is installed on top of the VDCs and scintillators. In the right figure, the Čerenkov detector is replaced by the carbon analyzer and the HDCs.

The polarization is experimentally defined as

$$P_i = \frac{\langle S_i \rangle}{S} = \frac{N_+^i - N_-^i}{N_+^i + N_-^i}, \quad (4.2)$$

where N_+^i (N_-^i) is the number of protons with $+1/2$ ($-1/2$) spin projection on \hat{i} . The functioning principle of the polarimeter is based on the scattering of protons on a secondary carbon (^{12}C) target. If the proton is polarized, the azimuthal distribution after the $p^{12}\text{C}$ scattering is not symmetric and from this asymmetry, the proton polarization can be extracted.

In Fig. 4.7 the scattering of a polarized proton on a ^{12}C nucleus in two different situations where the proton has a $+\frac{1}{2}$ or $-\frac{1}{2}$ spin projection is shown. The potential between the proton and the nucleus has a spin-orbit coupling term

$$V_{pC} \propto V_r(r) + V_{ls}(r) \langle \vec{L} \cdot \vec{S} \rangle, \quad (4.3)$$

and this coupling is responsible for the final azimuthal distribution asymmetry. Experimentally, a carbon analyzer is placed between the vertical drift chambers and the horizontal drift chambers: in this way, the proton is tracked before and after its scattering on ^{12}C (See Fig 4.8) and the event can be fully reconstructed. From the azimuthal (Φ_s angle) distribution the polarization can be extracted. The cross

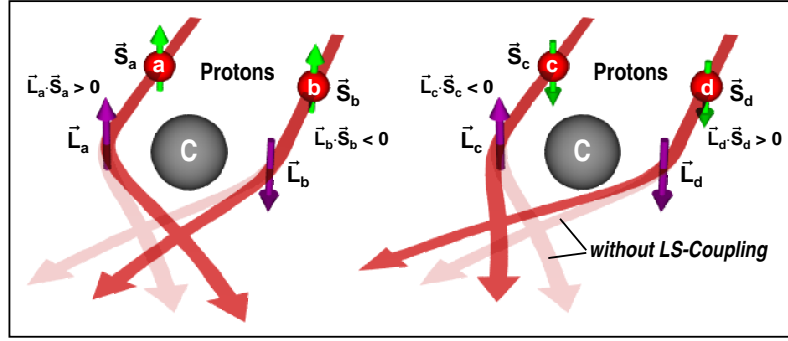


Figure 4.7: Scattering of a proton by a ^{12}C nucleus

section for the $p\ ^{12}\text{C}$ scattering process can be written as

$$\sigma = \sigma_0(\Theta, E_p) \left[1 + P_b h A_C(\Theta_s, E_p) (P_y^{FP} \cos \Phi_s - P_x^{FP} \sin \Phi_s) \right], \quad (4.4)$$

where $A_C(\Theta, E_p)$ is the carbon analyzing power (dependent on the scattering angle Θ_s and the proton energy E_p), P_x^{FP} and P_y^{FP} are two components of the proton polarization in the focal plane, h is the electron beam helicity and P_b the beam polarization.

It is clear, that in this way only two components of the proton polarization vector can be determined, but we are interested in the full polarization vector at target point, and not in the focal plane. Another complication arises from the fact that the proton spin is precessing in the spectrometer magnetic field, so the polarization measured in the focal plane is different from the polarization at the target position. In the next chapter, a solution to this problems will be presented.

Horizontal Drift Chambers

In order to detect the scattered protons by the carbon analyzer and then to reconstruct the azimuthal asymmetry, two horizontal drift chambers (HDC) with an active surface of $217.8 \times 74.95 \text{ cm}^2$ were constructed [50]. The two horizontal drift chambers are composed by two planes each. The first plane has $20\ \mu\text{m}$ thick signal wires with 10mm distance alternated by $100\ \mu\text{m}$ thick potential wires. The angle of the wires in respect to the chamber frame is 45° and in the second plane the wires are orthogonal in respect to the first. The wire planes are enclosed by aluminium-coated Mylar foils with $3.5\ \mu\text{m}$ thickness and the used gas mixture is Argon (20%) and Ethane (80%). The achieved space resolution is $\sigma_{x,y} \sim 300\ \mu\text{m}$ and the angular resolution is $\sigma_{\theta,\phi} \sim 2 \text{ mrad}$. The carbon analyzer is composed by an aluminium frame holding a graphite plane with a variable thickness of 1, 2 and 4 cm in order to adapt it to the mean proton energy fixed by the experimental kinematics. The analyzer is placed directly under the HDCs (see Fig 4.8).

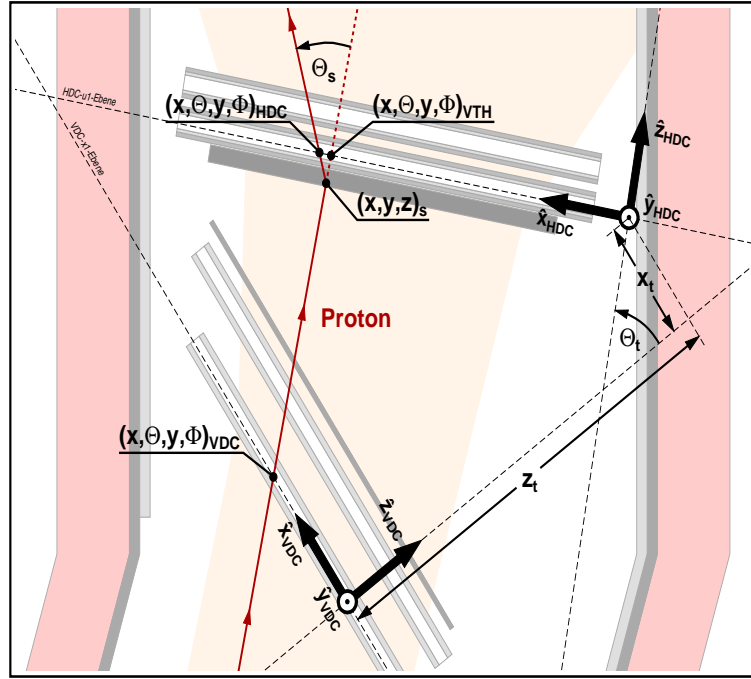


Figure 4.8: The various coordinate systems used with an example proton track are shown. The proton arrives from below after escaping the target, then its track is detected by the VDCs and, after scattering against the carbon analyzer with scattering angle Θ_s , is reconstructed by the HDCs. From the azimuthal Φ_s distribution, the polarization can be extracted. (Figure from [49])

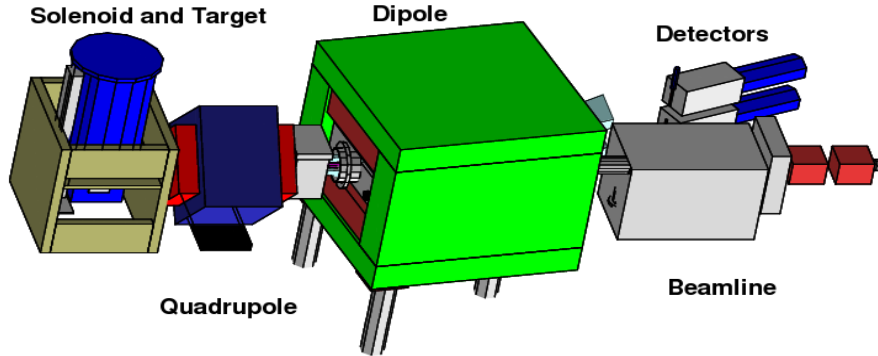


Figure 4.9: Møller Polarimeter for the absolute measurement of the electron beam polarization.

4.2.4 Møller Polarimeter

In order to have an absolute measurement of the beam polarization, a Møller Polarimeter is available directly before the target [47]. This gives the advantage to measure the polarization just before the scattering and after the path the electrons make through the accelerators and beam transport systems, where the polarization can change.

The polarimeter is based on the Møller scattering process $\vec{e} \vec{e} \rightarrow e e$ with cross section

$$\frac{d\sigma}{d\Omega} = \frac{d\sigma_0}{d\Omega} (1 + \alpha_{zz}(\theta_{cm}) P_b^z P_t^z) \quad (4.5)$$

where $d\sigma_0/d\Omega$ is the polarization independent part, P_b the beam polarization and P_t the target polarization. α_{zz} is the analyzing power (dependent from the scattering angle in the CM frame θ_{cm}) and the indices indicate the directions of the beam and target polarizations: α_{ij} with $i, j = x, y, z$.

In this case a specific direction is chosen because α_{zz} gives the higher figure of merit. In the general case, a sum over i and j must be performed.

The target polarization is fixed, while the beam polarization is reversed with 1 Hz frequency on a random basis. With a change of notation, calling $\sigma^{\uparrow\uparrow}$ and $\sigma^{\uparrow\downarrow}$ the two cases where the spins are parallel or antiparallel respectively, the following asymmetry can be built

$$A = \frac{\sigma^{\uparrow\uparrow} - \sigma^{\uparrow\downarrow}}{\sigma^{\uparrow\uparrow} + \sigma^{\uparrow\downarrow}} = \alpha_{zz}(\theta_{cm})P_b^z P_t^z \quad (4.6)$$

The polarized beam scatters on a 6 μm iron foil placed in a 4T magnetic field generated by a superconducting coil. The incoming polarized electrons scatter on the polarized ($P_{Fe} \sim 8\%$) electrons of the iron target. The scattered and the recoil electrons are focused by a quadrupole magnet and deflected by a dipole magnet in the direction of two Pb-Glass counters placed on one side of the beamline (Fig. 4.9). The two detectors are in time coincidence and the asymmetry 4.6 in their counts can be measured. The counting rate asymmetry, corrected by the luminosity and background counts (which are estimated with a non coincident time window)

$$\sigma^{\uparrow\uparrow,\uparrow\downarrow} = \frac{N_{coinc}^{\uparrow\uparrow,\uparrow\downarrow} - N_{bkg}^{\uparrow\uparrow,\uparrow\downarrow}}{N_{Lumi}^{\uparrow\uparrow,\uparrow\downarrow}} \quad (4.7)$$

is determined and knowing the analyzing power and the iron polarization degree, the polarization of the beam can be extracted:

$$P_b = \frac{A}{\alpha_{zz}(\theta_{cm})P_t^z} \quad (4.8)$$

The dominant contribution to the systematical error is given by the analyzing power: it is calculated theoretically but it should be averaged on the phase space accepted by the Pb-Glass detectors and this is done by simulation. Other sources of systematical errors are given by the knowledge of the beam and detector positions and from the target polarization P_t which depends mainly on the temperature and the applied magnetic field. The final systematical error reached for the beam polarization is $\sim \pm 1.2\%$. In the future, the systematical error will be lowered with the use of more segmented detectors (hodoscopes) made of scintillator strips. The single strips in coincidence have a smaller acceptance in comparison to the Pb-Glass detectors and this reduces the contamination given by electrons rescattered by the dipole magnet. With $\sim 500s$ measuring time, a statistical error comparable to the systematical one can be reached.

4.2.5 Trigger and Data Acquisition

The data acquisition system is triggered by the signals coming from the spectrometer scintillator planes dE and ToF. Every scintillator paddle is read by two photomultipliers in coincidence. The signals from the paddles are delivered to a PLU (Programmable Logic Unit). The PLU can select the events using only the dE or ToF signals, or asking for a coincidence between the two planes. The output of the PLU is taken by an FPGA³, where the coincidence between the spectrometers (or other detectors) is realized. The FPGA can be programmed in order to allow the variation of the coincidence time window and the variation of time delays depending on the kinematical configuration and the measured physical reaction.

The determination of the acquisition dead time is an important issue for realizing the coincidence between spectrometers. The acquisition dead time comes mainly from the electronics, while the detectors give practically no contribution. During the measurements the dead time is estimated by counters connected to the electronics gate signal.

In Fig.4.10 the logic structure of the trigger is shown.

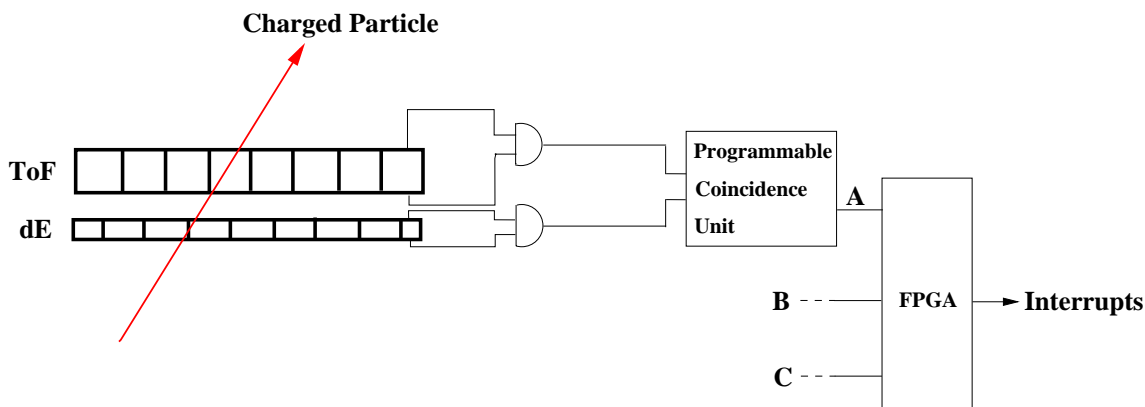


Figure 4.10: Logic scheme of the coincidence trigger.

³Field Programmable Gate Array

Chapter 5

Measurement of the Proton Polarization

“Angesichts von Hindernissen mag die kürzeste Linie zwischen zwei Punkten die krumme sein.”

Bertolt Brecht, Leben des Galilei

In this chapter, the method used for extracting the proton polarization is described. Only two components of the polarization can be measured in the focal plane, but it is possible to extract all the three components at the target position making use of the spin precession in the magnetic field of the spectrometer. In the reconstruction process the knowledge of the spin precession of the proton in the magnetic field is necessary. The study of the spin precession was carried out by Th.Pospischil [49] together with the development of a reconstruction algorithm based on a χ^2 fit.

In the χ^2 method, a binning in most of the kinematical variables was used, resulting in a very large number of bins ($\sim 10^3$): this implies some averaging on the variables and this is particularly problematic in the case of low statistics experiments.

In this work a new algorithm based on a maximum likelihood approach is developed which presents many advantages. The new method treats separately every event, avoiding the binning problem and then the most efficient use of the available statistics is done. For comparison with the theoretical calculations, a binning in one variable is chosen. In the VCS case, the theoretical polarizations are calculated as a function of $\theta_{\gamma\gamma}$ and it is the only binning variable used at the end.

After a description of the spin precession, the new method for reconstructing the proton polarization directly in the center of mass frame will be presented. The procedure is then extended to the direct fit of the generalized polarizabilities to the data.

5.1 Spin Precession in a Magnetic Spectrometer

The proton passes different magnetic fields in its path through the spectrometer and it is necessary to know how the proton spin is influenced by them. The variation with time of a spin four-vector in an electromagnetic field is described by the Bargmann-Michel-Telegdi (BMT) equation [52]

$$\frac{dS^\alpha}{d\tau} = \frac{e}{m} \left[\frac{g}{2} F^{\alpha\beta} S_\beta + \left(\frac{g}{2} - 1 \right) U^\alpha (S_\lambda F^{\lambda\mu} U_\mu) \right], \quad (5.1)$$

where $F^{\alpha\beta}$ is the electromagnetic field tensor, m the mass, τ the proper time, U^α the four-velocity, g the g-factor. The BMT equation for the spin vector \vec{S} is known as the Thomas equation ¹ [54]

$$\frac{d\vec{S}}{dt} = \frac{e}{m} \vec{S} \times \left[\left(\frac{g-2}{2} + \frac{1}{\gamma} \right) \vec{B} - \left(\frac{g-2}{2} \right) \frac{\gamma(\vec{v} \cdot \vec{B})\vec{v}}{c^2(\gamma+1)} - \left(\frac{g}{2} - \frac{\gamma}{\gamma+1} \right) \frac{\vec{v} \times \vec{E}}{c} \right]. \quad (5.2)$$

Here, the electric (\vec{E}) and magnetic (\vec{B}) fields are explicitly introduced. The particle velocity is \vec{v} and c is the speed of light. Decomposing then the magnetic field in two components, one parallel ($\vec{B}^\parallel = \frac{1}{|\vec{v}|^2}(\vec{v} \cdot \vec{B})\vec{v}$) and the other orthogonal ($\vec{B}^\perp = \vec{B} - \vec{B}^\parallel$) to \vec{v} and observing that $\vec{E} = 0$ inside the spectrometer's volume, the Thomas equation reduces to

$$\frac{d\vec{S}}{dt} = \frac{e}{m\gamma} \vec{S} \times \left[\frac{g}{2} \vec{B}^\parallel + \left(1 + \frac{g-2}{2}\gamma \right) \vec{B}^\perp \right]. \quad (5.3)$$

The vector product in the last equation implies that the variation is always orthogonal to the spin vector direction.

Simplified Case: Dipole Spectrometer

For a perfect Dirac particle, with $g = 2$ and placed in a magnetic field orthogonal to its motion, the relative orientation between velocity and spin does not change ². The proton has a bigger g-factor: $g_p = 5.5857$, so the spin vector is more influenced than the velocity vector from the magnetic field.

In order to understand how the precession is working, we can use the simplified case where a pure dipole magnetic field is applied in the \hat{y} direction while the particle is moving in the \hat{z} direction. In this approximation the angle χ of the spin \vec{S} variation due to \vec{B} is connected to the angle ϕ that express the trajectory bending caused by the Lorentz force by the relation

$$\chi = \gamma \left(\frac{g}{2} - 1 \right) \phi. \quad (5.4)$$

Typical values for protons entering spectrometer A are $\gamma \sim 1.1 \dots 1.27$; this, with an average bending angle of $\phi \sim 100^\circ$ gives a precession angle of $\chi \sim 200^\circ$. The important point is that the precession mixes two polarization components, leaving invariant the one transverse to the rotation plane (see Fig. 5.1). The connection between the focal plane polarization \vec{P}^{FPP} and the polarization \vec{P} before entering

¹This equation was already known before the generalized BMT equation: L.T. Thomas derived it already in 1927 in order to resolve a discrepancy between the observed atomic fine splitting and the Zeeman effect [53].

²This happens because spin and velocity are governed by the same kind of equation in the case of a purely orthogonal magnetic field acting on a Dirac particle: $\dot{s} \propto \vec{s} \times \vec{B}$; $\dot{v} \propto \vec{v} \times \vec{B}$

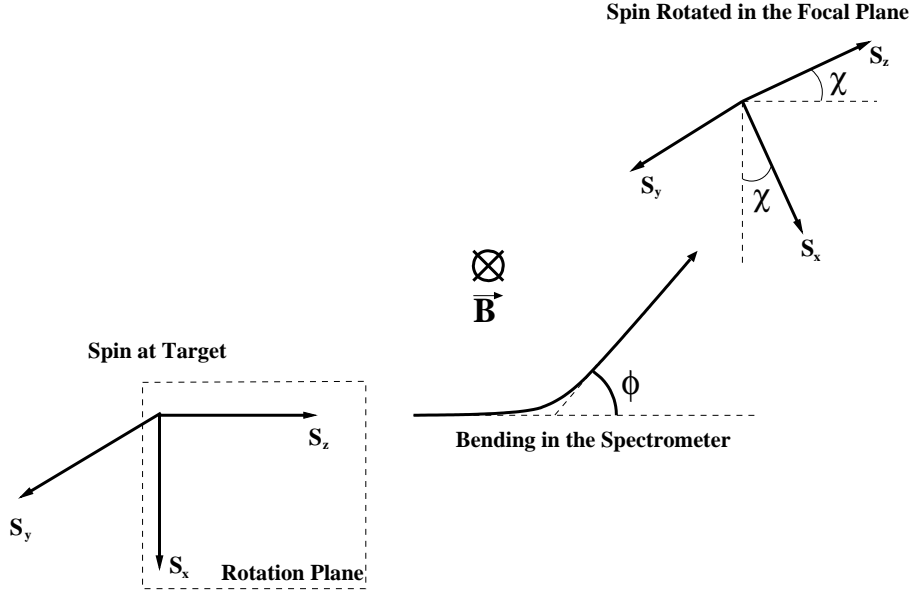


Figure 5.1: Precession of the spin components by the angle $\chi = \gamma \left(\frac{g}{2} - 1\right) \phi$: the polarization transversal to the rotation axis remains unchanged.

the spectrometer is given by

$$\begin{pmatrix} P_x \\ P_y \\ P_z \end{pmatrix}^{FPP} = \begin{pmatrix} \cos \chi & 0 & \sin \chi \\ 0 & 1 & 0 \\ -\sin \chi & 0 & \cos \chi \end{pmatrix} \begin{pmatrix} P_x \\ P_y \\ P_z \end{pmatrix}. \quad (5.5)$$

The component P_y does not precess, because it is parallel to the dipolar magnetic field. Furthermore, in the focal plane, only two components (P_x and P_y) can be measured, so Eq. 5.5 reduces to

$$\begin{pmatrix} P_x \\ P_y \end{pmatrix}^{FPP} = \begin{pmatrix} \cos \chi & \sin \chi \\ 1 & 0 \end{pmatrix} \begin{pmatrix} P_y \\ P_z \end{pmatrix}. \quad (5.6)$$

The above approximation is not precise enough for spectrometer A, and it is necessary to look for a more precise solution for describing the spin precession. In fact the magnetic field is not completely transversal to the particle path (the magnetic optics is not purely dipolar) and this means that also the component \vec{B}^{\parallel} in Eq. 5.3 is acting. Furthermore, the particle's path can and also be outside the spectrometer's middle plane.

Realistic case: Spectrometer A

The magnetic optics of spectrometer A is made by four magnets: a quadrupole, a sextupole and two dipoles, resulting in a rather large acceptance of 28 msr. This means that the particles can enter the spectrometer with different angles Θ_0 and Φ_0 and consequently the particle path is different for different angles.

Let's now take the example of two particles with the same momentum entering the

spectrometer, but with two different Θ_0 angles (and same Φ_0 for simplicity). The particles will arrive at the focal plane at the same point, but using two different paths. This means that the spin will precess differently in the two cases. On the focal plane, only two polarization components can be measured (using Eq. 4.4), but we need three components at target: it is exactly the redundancy explained before, that permits the reconstruction of three components starting from only two (see next section). In Fig. 5.2 three different tracks are drawn, corresponding to protons with the same momentum but different entrance variables: it is clear that the spin vector experiences a strong variation between different trajectories. Also the precession of particles entering with different Φ_0 and y_0 values, due to the quadrupole action are not well reproduced by a simple dipole approximation, as demonstrated in [49]. All the described problems force to find a better solution in order to calculate the polarization at the target position taking into account the complex magnetic configuration of the spectrometer.

5.2 Spin Backtracking in Spectrometer A

In order to overcome the problems given by the complex optics of spectrometer A, in [49] a program (QSPIN) was developed for calculating the spin precession as a function of the target coordinates $(\Delta p, \Theta_0, \Phi_0, y_0)$ and an initial proton spin vector \vec{S}^{Tg} . The program integrates the Thomas equation 5.3 with a variable step Runge-Kutta method. As an example, the tracks and spin precessions in Fig. 5.2 were obtained by QSPIN. What one needs, is a rotation that connects the spin vector in the focal plane to the spin vector at target: this can be written as

$$\begin{pmatrix} S_x \\ S_y \\ S_z \end{pmatrix}^{FP} = \begin{pmatrix} M_{xx} & M_{xy} & M_{xz} \\ M_{yx} & M_{yy} & M_{yz} \\ M_{zx} & M_{zy} & M_{zz} \end{pmatrix} \cdot \begin{pmatrix} S_x \\ S_y \\ S_z \end{pmatrix}^{Tg}. \quad (5.7)$$

The matrix \mathbf{M} is called *Spin Transfer Matrix*, or STM. The matrix elements are in principle unknown functions of the target variables $(\Delta p, \Theta_0^{Tg}, \Phi_0^{Tg}, y_0^{Tg})$ and the proton momentum p . The matrix elements can be expanded as a polynomial

$$M_{\kappa\lambda} = \sum_{ijklm} \langle M_{\kappa\lambda} | \Delta p^i \Theta_0^j y_0^k \Phi_0^l p_{ref}^m \rangle \Delta p^i \Theta_0^j y_0^k \Phi_0^l p_{ref}^m, \quad (5.8)$$

with $i, j, k, l, m \in \mathbb{N}_0$ and $\kappa, \lambda \in \{x, y, z\}$. A procedure for determining the coefficients $\langle M_{\kappa\lambda} | \Delta p^i \Theta_0^j y_0^k \Phi_0^l p_{ref}^m \rangle$ is needed.

With the aid of the program QSPIN, 1715 tracks were generated, assuming the starting spin vector configurations: (1,0,0), (0,1,0) and (0,0,1). The tracks are also generated for covering the entire spectrometer acceptance in angles, momentum and y_0 . The grid points used are reported in table 5.1. The resulting polynomial is rather large if one considers high powers of the coordinates: for reducing as much as possible the computational complexity, the power expansion was truncated differently depending on the coordinate, when a reasonable accuracy was reached. The

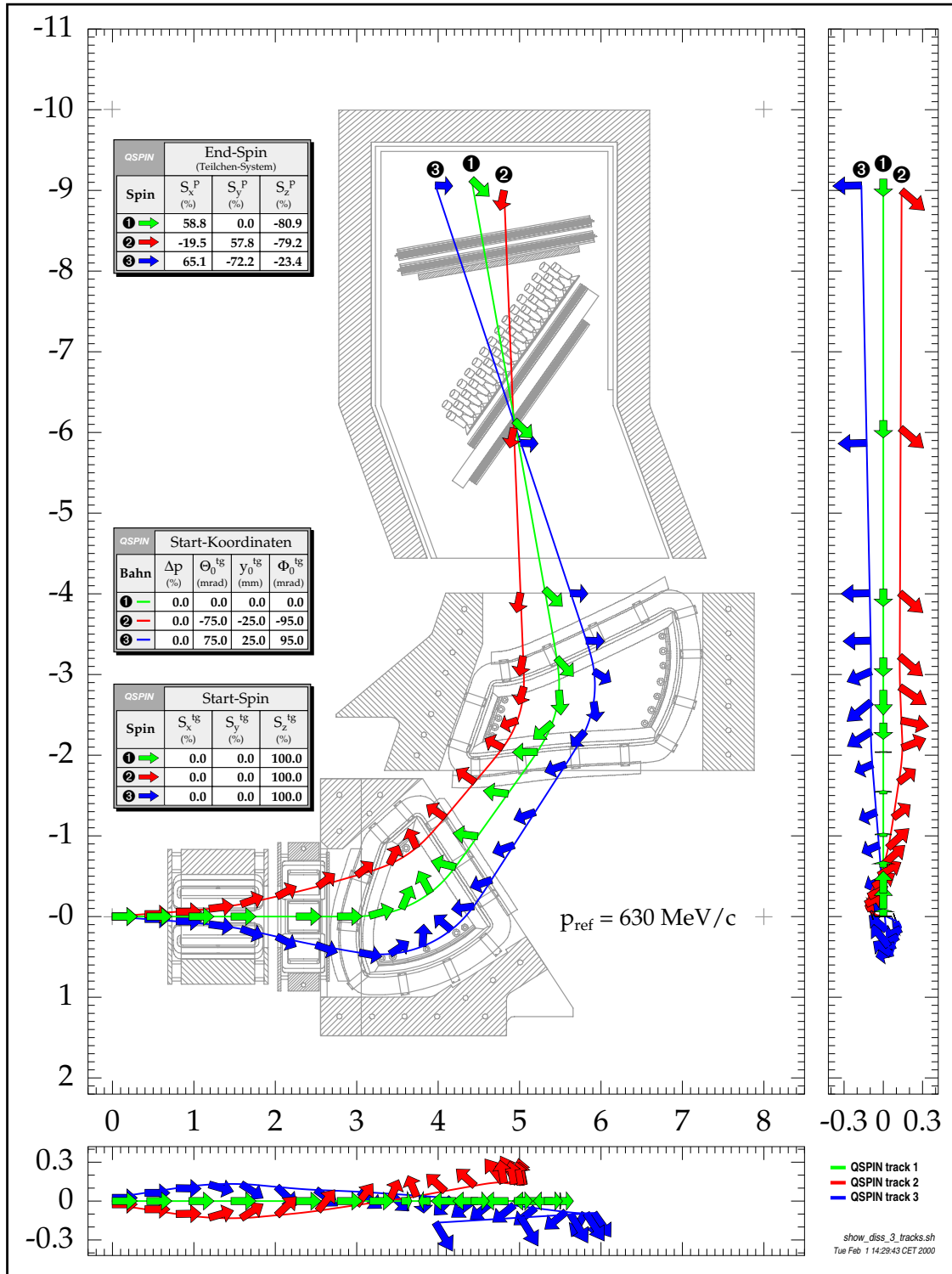


Figure 5.2: Three different tracks with the same initial spin but different target coordinates where calculated with the program QSPIN and here displayed inside spectrometer A. As it can be seen, the final spin is very different for the three tracks. The spin precession is then strongly dependent on the path inside the spectrometer magnetic fields (Figure from Th.Pospischil [49]).

Variable	Points	Order
dp	$[-5.7794, 0.0327, 5.6206, 11.0182, 16.2521]$ %	$i=2$
Θ_0	$[-75, -50, -25, 0, 25, 50, 75]$ mrad	$j=4$
y_0	$[-30, -20, -10, 0, 10, 20, 30]$ mm	$k=2$
Φ_0	$[-105, -70, -35, 0, 35, 70, 105]$ mrad	$l=4$
p_{ref}	$[480, 510, 540, 570, 600, 630]$ MeV/c	$m=2$

Table 5.1: Value of the parameters used to generate the tracks with the program QSPIN, and the relative polynomial order of the expansion. The resulting total number of parameters is 675

resulting total number of parameters is 675 and a χ^2 minimization procedure was used for their determination.

Using the fitted coefficients, the entries of the matrix \mathbf{M} are known. As a check, the fitted STM is able to reproduce with 0.3% accuracy the precessed spin components for the tracks used for the fit. The accuracy in reproducing “unknown” precessions is $\sim 1\%$, reflecting the good interpolating power of the STM.

5.3 Calculation of the Polarization

Having connected the FP polarization with the target polarization through the STM rotation matrix, a procedure is needed in order to “invert” this process and calculate the target polarization starting from the measured FP one. At the end we are interested in the CM frame polarization and also a Lorentz boost must be included in the procedure.

An “eventwise” method, based on a maximum likelihood approach was developed in this work and it will be presented in the following.

5.3.1 Maximum Likelihood algorithm: Introduction

Having mapped the proton precession in spectrometer A into the matrix \mathbf{M} , a method for reconstructing the proton polarization in the CM frame has to be developed. What can be directly measured, are two components of the proton polarization in the focal plane, using Eq 4.4 that we rewrite here for convenience

$$\sigma = \sigma_0(\Theta, E_p) \left[1 + P_b h A_C(\Theta_s, E_p) (P_y^{FP} \cos \Phi_s - P_x^{FP} \sin \Phi_s) \right]. \quad (5.9)$$

There is an efficient procedure for both fitting the Φ_s distribution and calculating the polarization vector in the CM frame and it is based on a maximum likelihood method. Starting from the cross section 5.9, the probability for the event i to have a certain polarization in the focal plane \vec{P}^{FP} given the analyzing power and the scattering angle Φ_s is

$$p_i(P^{FP} | A_C, \Phi_s) = \left[1 + P_b h A_C(\Theta_{s,i}, E_{p,i}) (P_y^{FP} \cos \Phi_{s_i} - P_x^{FP} \sin \Phi_{s_i}) \right]. \quad (5.10)$$

On an event basis, the likelihood function can be constructed:

$$\mathcal{L}(P_x^{FP}, P_y^{FP}) = \prod_{i=1}^N p_i(P^{FP}|A_{C,i}, \Phi_{s,i}), \quad (5.11)$$

where N is the total number of events considered. Maximizing this expression or, numerically easier, its logarithm³

$$\ln \mathcal{L}(P_x^{FP}, P_y^{FP}) = \sum_{i=1}^N \ln p_i(P^{FP}|A_{C,i}, \Phi_{s,i}), \quad (5.12)$$

the best estimate for P_x^{FP} and P_y^{FP} can be obtained. More statistical details about the method can be found in App. B.

We are finally interested in the polarizations in the CM frame. If the event kinematics is determined, all the transformations are known for bringing the polarization vector from the CM frame to the focal plane. If we express the action of all the transformations with the function $P^{\vec{FP}} = \mathbf{R}(\vec{P}^{CM})$, the likelihood is transformed in a function of \vec{P}^{CM}

$$\mathcal{L}(P_x^{CM}, P_y^{CM}, P_z^{CM}) = \prod_{i=1}^N \left[1 + P_b h_{AC}(\Theta_{s,i}, E_{p,i}) (\mathbf{R}(\vec{P}^{CM}) \cos \Phi_{s,i} - \mathbf{R}(\vec{P}^{CM}) \sin \Phi_{s,i}) \right], \quad (5.13)$$

The best estimate for the target polarization components is then

$$\left. \begin{aligned} \frac{\partial}{\partial P_x^{CM}} \ln \mathcal{L}(P_x^{CM}, P_y^{CM}, P_z^{CM}) &= 0 \\ \frac{\partial}{\partial P_y^{CM}} \ln \mathcal{L}(P_x^{CM}, P_y^{CM}, P_z^{CM}) &= 0 \\ \frac{\partial}{\partial P_z^{CM}} \ln \mathcal{L}(P_x^{CM}, P_y^{CM}, P_z^{CM}) &= 0 \end{aligned} \right\} \Rightarrow \langle P_x^{CM} \rangle ; \langle P_y^{CM} \rangle ; \langle P_z^{CM} \rangle. \quad (5.14)$$

The already discussed redundancy which permits to calculate also the three polarization components starting from two directly measured ones is present here in the likelihood function, where all the events are taken into account.

The full covariance matrix can also directly calculated (see. App. B) as

$$\sigma_{ij}^2 = \left[\frac{\partial^2 \ln \mathcal{L}}{\partial_i \partial_j \vec{P}^{CM}} \right]_{ij}^{-1}. \quad (5.15)$$

In the case of negligible covariances, the statistical errors on the single polarization components are the diagonal matrix elements $\delta P_i^{CM} = \sqrt{\sigma_{ii}}$.

³The logarithm is a monotonic function, so the position of maxima and minima of \mathcal{L} is not changed. Furthermore, \mathcal{L} is the product of distribution functions that are by definition positive, so $\ln \mathcal{L}$ is always well defined.

5.3.2 Maximum Likelihood algorithm: Implementation

Reference Frame Transformations

Measurements are done in the laboratory frame while usually theoretical calculations are done in the center of mass frame: in order to compare experimental and theoretical results a suitable transformation is needed.

The first transformation is a Lorentz boost \mathbf{L} from the CM frame to the laboratory frame. The effect of such a transformation on a spin vector is usually described by means of the Wick-Wigner angle⁴. A drawback in the practical calculation of the Wick-Wigner angle resides in its numerical instability so a more efficient way for defining the Lorentz transformation of a spin vector is used here. The spin vector \vec{s} is extended to a fourvector [53]:

$$S^\mu = \begin{pmatrix} \gamma \vec{\beta} \cdot \vec{s} \\ \vec{s} + \frac{\gamma^2}{\gamma+1} (\vec{\beta} \cdot \vec{s}) \vec{\beta} \end{pmatrix}. \quad (5.16)$$

The advantage is that one can use the usual Lorentz transformations of the fourvectors in order to change the reference frame of S^μ ⁵. After the transformation, the vector components are reprojected out:

$$\vec{s} = \vec{S} + \frac{\gamma^2}{\gamma+1} (\vec{\beta} \cdot \vec{S}) \vec{\beta}, \quad (5.17)$$

where one notices that only the spatial components of S^μ are used. The second transformation, \mathbf{S} , is a rotation from the laboratory to the spectrometer reference frame, which is described in Fig. 5.3. The third transformation \mathbf{M} is the application of the spin transfer matrix.

Parameterization of the transformations

The composition of the three transformations can be described with an unique rotation matrix

$$\mathbf{R} = \mathbf{M} \circ \mathbf{S} \circ \mathbf{L}. \quad (5.18)$$

Being \mathbf{R} a rotation matrix, it can be parameterized by three parameters which are chosen to be the Euler angles θ_x , θ_y and θ_z (Fig. 5.4). The full rotation matrix is then

⁴See [55] for the original article by G.C. Wick, [56] for the most commonly used expression for the Wick-Wigner angle and [57] for a recent discussion of the problem in the framework of electron scattering experiments.

⁵Within the A1 analysis software package (Cola++) a library for operations on four-vectors is available.

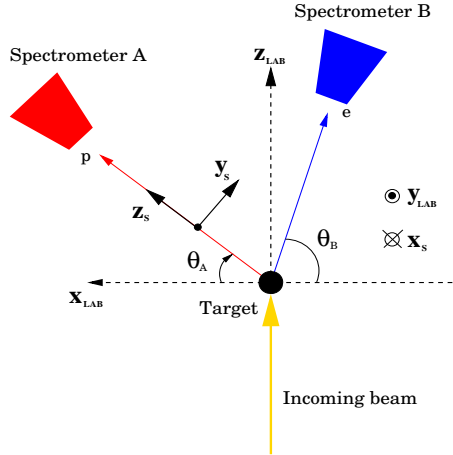


Figure 5.3: Laboratory reference frame: the z axis is oriented along the beam direction, the x axis points in the direction of the experimental hall floor. The spectrometer reference frame is defined through a rotation of the laboratory reference system around the x_{lab} axis by a θ_A angle.

$$R(\theta_x, \theta_y, \theta_z) = \begin{pmatrix} 1 & 0 & 0 \\ 0 & \cos \theta_x & -\sin \theta_x \\ 0 & \sin \theta_x & \cos \theta_x \end{pmatrix} \begin{pmatrix} \cos \theta_y & 0 & -\sin \theta_y \\ 0 & 1 & 0 \\ \sin \theta_y & 0 & \cos \theta_y \end{pmatrix} \begin{pmatrix} \cos \theta_z & -\sin \theta_z & 0 \\ \sin \theta_z & \cos \theta_z & 0 \\ 0 & 0 & 1 \end{pmatrix}, \quad (5.19)$$

and the Euler angles can be calculated with:

$$\begin{cases} \theta_x = \arctan \frac{R_{12}}{R_{22}} \\ \theta_y = \arctan \frac{-R_{02} \cos \theta_z}{R_{00}} \\ \theta_z = \arctan \frac{-R_{01}}{R_{00}} \end{cases} \quad (5.20)$$

Implementation

The polarization reconstruction based on the maximum likelihood method is implemented in the C++ program `CalcPolarization`. The A1 analysis software analyzes the experimental data and writes on a data file all the informations needed for the construction of the likelihood: beam helicity, analyzing power, scattering angle Φ_s and the three Euler angles. In addition, also $\theta_{\gamma\gamma}$ is stored: a maximum likelihood fit is done for every bin in this variable for direct comparison with theoretical calculations. Every other binning variable can be in principle be chosen.

The data file is read by `CalcPolarization` which builds the likelihood, maximizes⁶ it and calculates the covariance matrix for the estimated polarization components.

⁶In the program what is done is the minimization of $-\ln \mathcal{L}$ with a Simplex routine [5].

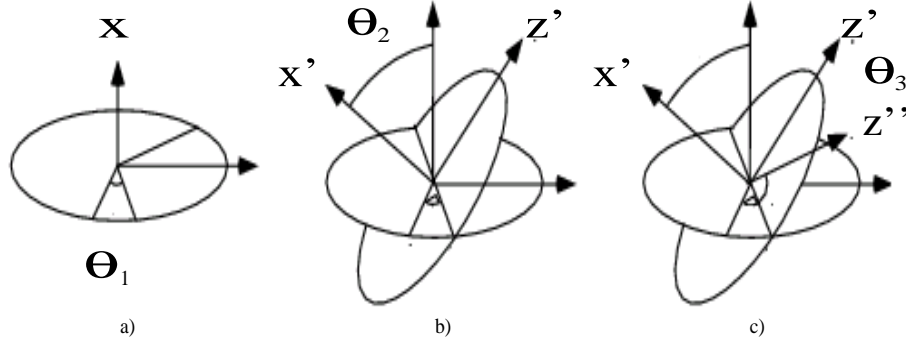


Figure 5.4: The figure explains the Euler rotations used for parameterizing the three transformations \mathbf{M} , \mathbf{S} and \mathbf{L} . Rotation $R(\theta_1)$ (a) is around the x axis by an angle θ_1 ; rotation $R(\theta_2)$ (b) is around the y axis by an angle θ_2 ; rotation $R(\theta_3)$ (c) is around the transformed y' axis by an angle θ_3 .

5.4 Extension to the Generalized Polarizabilities

The parameters of the likelihood can also be expressed as a function of another set of parameters: for example we have replaced \vec{P}^{FP} with \vec{P}^{CM} by means of a suitable set of transformations summarized by the rotation \mathbf{R} . The idea can be pushed forward: we can express now the CM frame polarization \vec{P}^{CM} directly as a function of the generalized polarizabilities.

$$\mathcal{L}(\vec{P}^{CM}) \implies \mathcal{L}(\text{GP}_i) \quad , \quad i = 1..6 \quad (5.21)$$

and this can be done with the aid of Eq. 2.52, 2.53, 2.54 and 2.55.

Once \vec{P}^{CM} is expressed as a function of the structure functions and then of the GPs, the maximization of the likelihood can be done directly varying the generalized polarizabilities instead of \vec{P}^{CM} . In alternative, also the structure functions can be chosen as fitting parameters.

5.5 Summary

A new procedure for the polarization reconstruction based on a maximum likelihood algorithm is developed. The algorithm works “eventwise”: there is no binning in the kinematical variables and all the events are taken into account in the likelihood. The full precession inside the magnetic optics of the spectrometer is considered for each event and the appropriate transformations for fitting the polarization components directly in the center of mass are used. The algorithm is theoretically founded (see App. B) and gives also a consistent treatment of the statistical errors in form of the full covariance matrix.

The final aim of this experiment is to measure the generalized polarizabilities or some new combination of them: the method can be extended in a natural way for fitting directly the structure functions or the generalized polarizabilities to the data.

Chapter 6

Simulation

The result of this experiment was inconclusive, so we had to use statistics

Overheard at an international physics conference, L.Lyons

6.1 Overview of the Simulation

Considering the precision needed for measuring the generalized polarizabilities in a double polarization experiment, a detailed simulation of the whole procedure described in the last chapter is mandatory.

Within the A1 collaboration a full simulation (`Simul++`) of the experimental setup was developed in the past. The package `Simul++` can simulate, according to a chosen kinematics the full phase space accepted by the spectrometers or in alternative, the events can be generated sampling a distribution given by the cross section of a specific process. The output data of the simulation is fully compatible with the real experimental data, so the same analysis and histogramming programs can be used in the two cases.

The simulation of the Bethe-Heitler and Born (BH+B) processes was developed initially by H.Merkel: the amplitudes are calculated for a given kinematics evaluating exactly all the needed Feynman graphs and this is done for every simulated event. In [59], the simulation was extended for the simulation of the BH+B polarizations starting from the BH+B amplitudes.

In this work, the simulation is further extended for simulating the VCS process (both the unpolarized cross section and the double polarization observables) with the LEX formalism described in Chapt. 2. The generalized polarizabilities used in the simulation are those of HB χ PT at $\mathcal{O}(p^3)$ [22].

The final simulation should be able to generate the full dataset needed for building the likelihood function and extract the polarization components from the simulated events. This means that also the carbon analyzing power and the azimuthal scattering angle in the focal plane have to be simulated. At the moment, the tracking and resolution effects of the HDCs are not taken into account and this will be matter of further development of the simulation.

In the following, it will be described in more detail how the simulated data are produced and the results for the polarization reconstruction will be shown.

6.2 Simulation of the Proton Polarization

In order to check if the procedure described in the last chapter is really able to extract the proton polarizations, the simulation program was extended for simulating them. As already explained, the program `CalcPolarization` maximizes the likelihood

$$\mathcal{L}(P_x^{cm}, P_y^{cm}, P_z^{cm}) = \prod_{i=1}^N \left[1 + h A_C(\Theta_{s,i}, E_{p,i}) (\mathbf{R}(\vec{P}^{CM}) \cos \Phi_{s,i} - \mathbf{R}(\vec{P}^{CM}) \sin \Phi_{s,i}) \right], \quad (6.1)$$

and the result is an estimate for the polarization components in the CM frame. With the function \mathbf{R} the various rotations connecting \vec{P}_{CM} and \vec{P}_{FP} are indicated. What is needed for building the likelihood function is, for each event:

- A variable as a function of which the polarization data are binned. Following the theoretical works, the chosen variable is the already defined angle between the two photons in the CM frame $\theta_{\gamma\gamma}$
- The analyzing power of the carbon plane: $A_C(E_p, \Theta_s)$
- The helicity h of the beam¹
- The azimuthal scattering angle Φ_s
- Three Euler angles which parameterize all the rotations involved in transforming the CM polarizations to the focal plane polarizations.

The angle $\theta_{\gamma\gamma}$ is calculable once an event has been generated and the helicity is reversed for each event. The full knowledge of the Bethe-Heitler plus the Born (BH+B) theoretical cross sections permits to simulate also the corresponding recoil proton polarization using

$$P_i = \frac{\hat{\sigma}_+^i - \hat{\sigma}_-^i}{\hat{\sigma}_+^i + \hat{\sigma}_-^i}, \quad (6.2)$$

for $\hat{i} = \hat{x}, \hat{y}, \hat{z}$.

The polarization is generated in the CM frame and needs to be transported to the focal plane. For doing this, the following transformations are applied:

- Lorentz boost for bringing the polarization to the laboratory frame
- A rotation to the spectrometer frame (see Fig. 5.3)
- The spin precession matrix (STM) is used for obtaining the focal plane polarizations.

The Euler angles corresponding to the full rotation ($\mathbf{M} \circ \mathbf{S} \circ \mathbf{L}$) are also saved for each event. When the focal plane polarizations are generated, the azimuthal distribution

$$P(\Phi_s | P_x^{fpp}, P_y^{fpp}) = [1 + h A_C(\Theta_s, E_p) (P_y^{FP} \cos \Phi_s - P_x^{FP} \sin \Phi_s)] , \quad (6.3)$$

can be sampled for generating a random scattering angle Φ_s if also the analyzing power is known.

¹In the real experimental case, the helicity is multiplied by the measured polarization degree of the beam P_b .

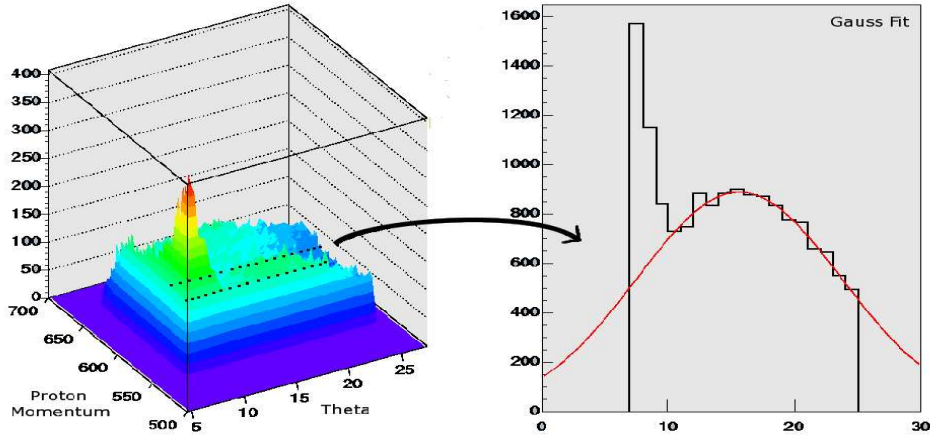


Figure 6.1: Parameterization of the analyzing power based on the experimental distribution. The large peak at low angles and energies is caused by multiple scattering events and it is cut away in the analysis.

6.2.1 Analyzing power sampling

The last ingredient for constructing the event distribution in the focal plane is the analyzing power. The analyzing power of the carbon plane is dependent from the proton energy in the carbon T_C and from the scattering angle Θ_s . The proton energy in the carbon T_C is calculated from the proton energy applying the appropriate energy losses. For the generation of the scattering angle Θ_s the chosen solution makes use of the experimental (T_C, Θ_s) two-dimensional distribution which is fitted in bins of T_C with a gaussian distribution as shown in Fig. 6.1. Once the proton energy in the carbon is known from the event kinematics, a bin in T_C is chosen and the corresponding fitted distribution for Θ_s is sampled. Knowing T_C and Θ_s , the analyzing power can at the end be calculated using the appropriate parameterization [60].

6.2.2 Statistical Errors and Correlations

For the final aim of extracting the generalized polarizabilities, it is important to know the final error achieved in the calculation of the polarizations. For studying this problem, different datasets were simulated with growing number of events. Constant polarizations in the phase space are simulated and fitted with the maximum likelihood algorithm and five bins in $\theta_{\gamma\gamma}$ are chosen in the range $[-150^\circ, -50^\circ]$. In Fig. 6.2 (top) the behavior of the error on the three polarization components P_x , P_y and P_z is displayed as a function of the number of events considered. It is evident the typical decreasing of the error as the square root of the number of events, as expected. The error on the P_z^{CM} component is also larger in respect to the other

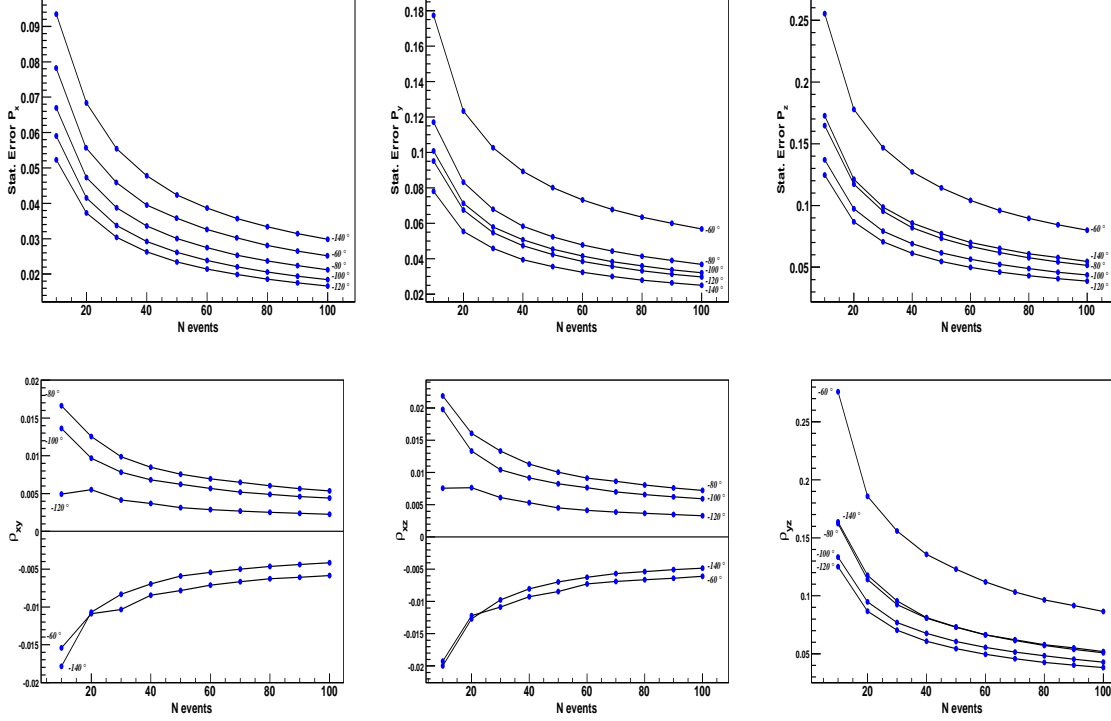


Figure 6.2: (Top): Statistical error as a function of the number of events for the three polarization components of PCM . (Bottom): From left, correlation coefficients $\rho_{ij} = \sigma_{ij} / \sqrt{\sigma_{ii}\sigma_{jj}}$ as a function of the number of events.

two: this is also expected, because this component is not directly measured in the focal plane but comes out thanks to the spin precession: its calculation is based on less information.

The method yields the full correlation matrix σ_{ij} with $i, j = x, y, z$ of which the square root of the diagonal elements are the errors on the polarization components (if the correlations can be neglected). The three off-diagonal terms (the matrix is symmetric) give the correlations between the components: in the Fig. 6.2 (bottom) the correlation coefficients $\rho_{ij} = \sigma_{ij} / \sqrt{\sigma_{ii}\sigma_{jj}}$ are plotted as a function of the number of events for each bin in $\theta_{\gamma\gamma}$. The correlation between P_x^{CM} and the other two components is low; on the contrary between P_y^{CM} and P_z^{CM} the correlation is higher. This fact is explained remembering that the spectrometer has in rough approximation a dipolar magnetic field which induces a rotation of the polarization vector mainly around the x axis, so the components P_y^{CM} and P_z^{CM} are rotated approximately by the same angle of precession. This is true only in first approximation, because the magnetic optics is more complex, but it explains the higher correlation between two of the three components.

6.3 Simulation of Virtual Compton Scattering Polarizations

The polarization of the VCS process depends on five kinematical variables: q , ϵ , $\theta_{\gamma\gamma}$, ϕ and q' . The values of q and ϵ are reasonably well fixed, but the acceptance regarding ϕ and q' is large. Also the acceptance in $\theta_{\gamma\gamma}$ is large, but the polarization components are calculated in bins of this variable.

The problem is that the reconstructed polarizations cannot be confronted with the theoretical predictions at nominal kinematics (where the five kinematical variables are fixed), because the mentioned large experimental acceptance.

A common solution is to construct a projection of the experimental data to nominal kinematics, but in this case a more practical solution is considered: construct a theoretical curve based on the real experimental kinematics as will be explained in the following.

The simulated data (or the real ones) can be used as an input to the theoretical polarization formulas: the result is a distribution of events in the $(P_{x,y,z}, \theta_{\gamma\gamma})$ plane which reflects also the variability of the other kinematical variables (in particular ϕ and q'). The distribution of the events is indicated in the next figures as a gray shaded region.

For each $\theta_{\gamma\gamma}$ point, the mean polarization can be calculated starting from the event distribution. The mean kinematical value is indicated in the next figures as $\langle \text{BH+B} \rangle$ (green curve). The nominal kinematics is also always reported as reference (red curve).

The maximum likelihood reconstruction of the simulated polarization in the VCS case is shown in Fig. 6.3: with the chosen kinematics², it is not possible to reconstruct exactly all the polarization components, because the projection of P_z on the focal plane is small. An error of about 10% remains for the P_y^{CM} and P_z^{CM} components which are strongly rotated by the magnetic field while P_x (which has a small precession) is more precisely reconstructed.

Introduction of Constraints

For the simulation of the BH+B polarizations the value of every component is known exactly for each event and this information can be used in the fitting procedure.

In the case of real data the appropriate constraint cannot be given, but the BH+B information remains close to the physical case, because the GPs effect is relatively small. The constraint can be used on P_y^{CM} or P_z^{CM} : for each event, the constrained component is calculated and used in the likelihood instead of fitting it. The results for both the constraints are shown in Fig. 6.4. A systematic difference between fitted values and mean theoretical polarization can be noted in this figures. The reason for this remaining discrepancy will be analyzed in the next section.

²The kinematics corresponds to the VCS90 experimental setup, see Chapt. 7

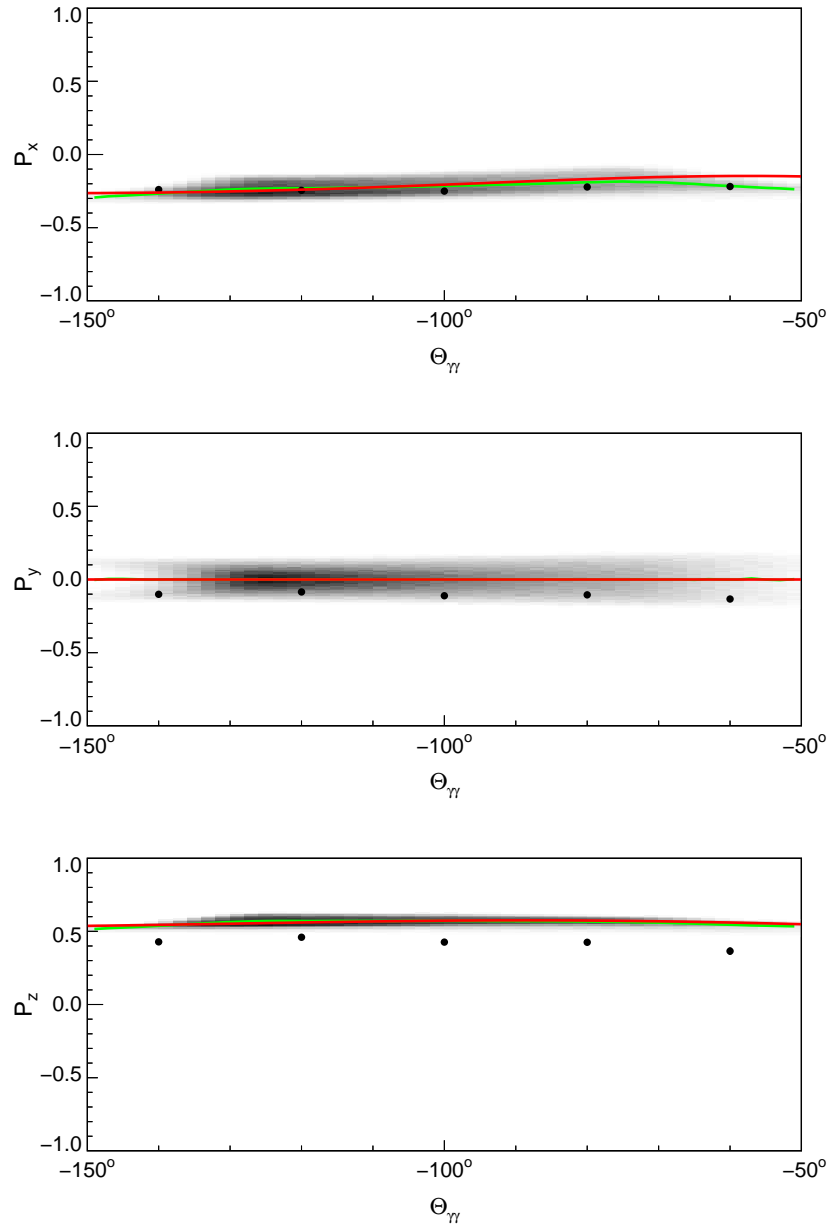


Figure 6.3: Simulated BH+B Polarizations ($5 \cdot 10^5$ events).

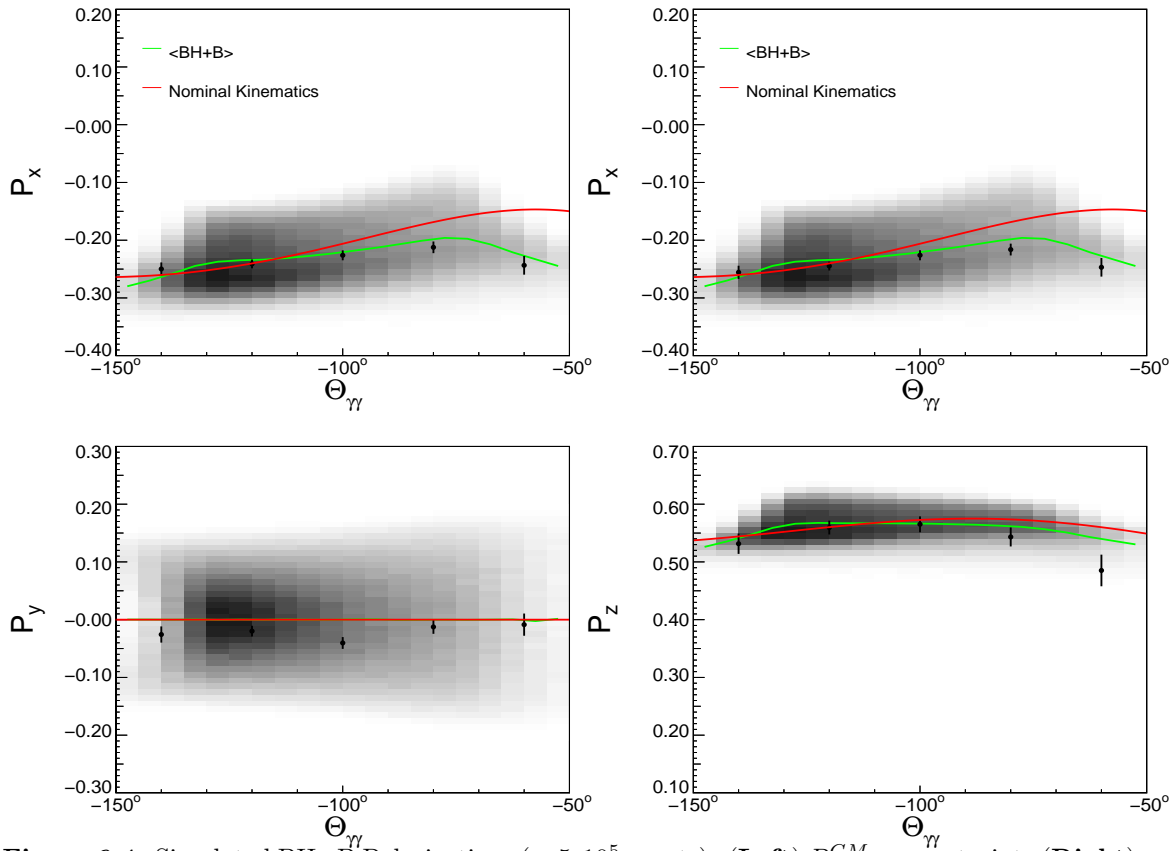


Figure 6.4: Simulated BH+B Polarizations ($\sim 5 \cdot 10^5$ events). **(Left)** P_z^{CM} as constraint. **(Right)** P_y^{CM} as constraint.

6.4 Correction of the P_y Polarization Component

As seen in the last section, a residual $\sim 3\%$ difference from the mean kinematical curve remains for the P_y^{CM} and P_z^{CM} components. The simulation and the reconstruction algorithms were extensively checked for finding the origin of this remaining discrepancy.

It is found that if the polarizations are simulated and reconstructed without the spin rotation due to the magnetic fields the procedure works perfectly (*i.e.*, with an increasing number of simulated events, the reconstructed points go exactly on the mean kinematical curve).

The problem must lie in the rotation matrix itself, which is different for each event. As described in the previous chapter, the rotation matrix contains all the rotations and the Lorentz boost needed for bringing a polarization vector from the center of mass frame to the focal plane. Being a rotation matrix, it can be parameterized by three variables, which in this case are chosen to be three Euler angles (see Chapt. 5).

The rotation matrix \mathbf{R} can be written as

$$R = \begin{pmatrix} a_{xx} & a_{xy} & a_{xz} \\ a_{yx} & a_{yy} & a_{yz} \\ a_{zx} & a_{zy} & a_{zz} \end{pmatrix} \quad (6.4)$$

where the matrix elements a_{ij} are not fixed constants but are dependent from the event kinematics. This matrix acts on the CM polarization vector

$$P_i^{FP} = R_{ij} P_j^{CM} \quad , \quad i, j = x, y, z \quad (6.5)$$

producing the polarization vector \vec{P}^{FP} in the focal plane. The logarithm of the likelihood to be maximized can then be rewritten with the aid of the above rotation matrix

$$\begin{aligned} \ln \mathcal{L}(P_x^{FP}, P_y^{FP}) = & \\ & \sum_{i=1}^N \ln [1 + hA_C(\Theta_{s,i}, E_{p,i}) P_y^{FP} \cos \Phi_{s,i} - P_x^{FP} \sin \Phi_{s,i}] = \\ & \sum_{i=1}^N \ln [1 + hA_C(\Theta_{s,i}, E_{p,i}) (a_{yx}^i P_x^{CM} + a_{yy}^i P_y^{CM} + a_{yz}^i P_z^{CM}) \cos \Phi_{s,i} - \\ & (a_{xx}^i P_x^{CM} + a_{xy}^i P_y^{CM} + a_{xz}^i P_z^{CM}) \sin \Phi_{s,i}] . \end{aligned} \quad (6.6)$$

and rearranging the terms

$$\begin{aligned} \ln \mathcal{L}(P_x^{FP}, P_y^{FP}) = & \\ & \sum_{i=1}^N \ln \{ 1 + hA_C(\Theta_{s,i}, E_{p,i}) [P_x^{CM} (a_{xx}^i \cos \Phi_{s,i} - a_{yx}^i \sin \Phi_{s,i})] + \\ & hA_C(\Theta_{s,i}, E_{p,i}) [P_y^{CM} (a_{xy}^i \cos \Phi_{s,i} - a_{yy}^i \sin \Phi_{s,i})] + \\ & hA_C(\Theta_{s,i}, E_{p,i}) [P_z^{CM} (a_{yz}^i \cos \Phi_{s,i} - a_{xz}^i \sin \Phi_{s,i})] \} . \end{aligned} \quad (6.7)$$

In the last expression it is clearly visible the third component of the CM polarization which is not directly measured, but enters indirectly in the likelihood through the rotation matrix. It is also clear that the fit of P_z is more difficult, because only two off-diagonal matrix elements related to the z component are entering the likelihood, while the other two components are represented with more coefficients related to their own rotation.

As demonstrated, the reconstruction of the focal plane polarization \vec{P}^{FP} is feasible, in the sense that the result, with an increasing number of events, converges to the mean focal plane polarization.

It is not an obvious fact if after the application of the rotation matrix, also \vec{P}^{CM} converges to the mean center of mass polarization. As showed in Fig. 6.4 it is not the case.

This can happen if a matrix element is strongly asymmetric as a function of a target

variable.

This is the case for a_{xy} , which varies in a not symmetric way for events above or under the scattering plane: this causes a biased reconstruction of the P_y^{CM} component. In Fig. 6.5 the simulated matrix elements involved in the likelihood are plotted as a function of the out-of-plane angle $\phi_{\gamma\gamma}$: every coefficient has a kind of symmetry in respect to $\phi_{\gamma\gamma} = 0$, but a_{xy} has not. For $\phi_{\gamma\gamma} < 0$ the value of the matrix element is $a_{xy} \sim -1$ (with a small dispersion around this value, as the error bars show). To reconcile the fitted points with the theoretically expected values, two strategies are possible:

- Do not compare the fitted points with the mean CM polarization, but introduce an appropriate weighting factor for taking into account the asymmetric treatment of the out-of-plane events. The weighting factor is the matrix element a_{xy} itself evaluated for each event. In Fig. 6.6 are visible the weighted theoretical mean values, which are now in accordance with the reconstructed polarizations. The asymmetry in the treatment of the out-of-plane events results in the lowering of P_y^{CM} .
- The P_y^{CM} component is reconstructed with an offset which is the same in each bin. An appropriate correction factor can be applied (the same in each bin) for bringing the fitted points back on the theoretical mean value ($P_y^{CM} = 0$).

In the following we choose then the second strategy for comparing reconstructed and theoretical polarizations because

- As seen, only P_y^{CM} is affected by the weighting factor, while P_x^{CM} remains almost unaffected.
- P_y^{CM} is constant as a function of $\theta_{\gamma\gamma}$ so an unique offset value is sufficient

With a large statistics sample of simulated events ($\sim 1 \cdot 10^6$ events) the overall correction offset is

$$\delta P_y = -0.027 \quad (6.8)$$

with a negligible statistical error.

Using this correction offset for P_y directly in the fit for each event, good agreement is found. The remaining discrepancies are caused from the analyzing power, which is different for each event and in particular it is low for low energy protons (low $|\theta_{\gamma\gamma}|$ angles). If the analyzing power is fixed to a constant value, perfect agreement is found with negligible error bars. The final results are shown in Fig. 6.7 for the fit of P_x^{CM} and P_y^{CM} while P_z^{CM} is used as constraint.

The correction is used only for better comparing theory and experimental result: there is no error in the polarization reconstruction. The reconstructed polarization has to be confronted not with the mean polarization in CM frame but with a curve weighted with the appropriate factor that takes into account the different spin rotations which the events experience in the spectrometer magnetic field. The disagreement of the reconstructed polarization with the expected value decreases as a function of the number of simulated events and the convergence is faster if a constant value of the analyzing power is used.

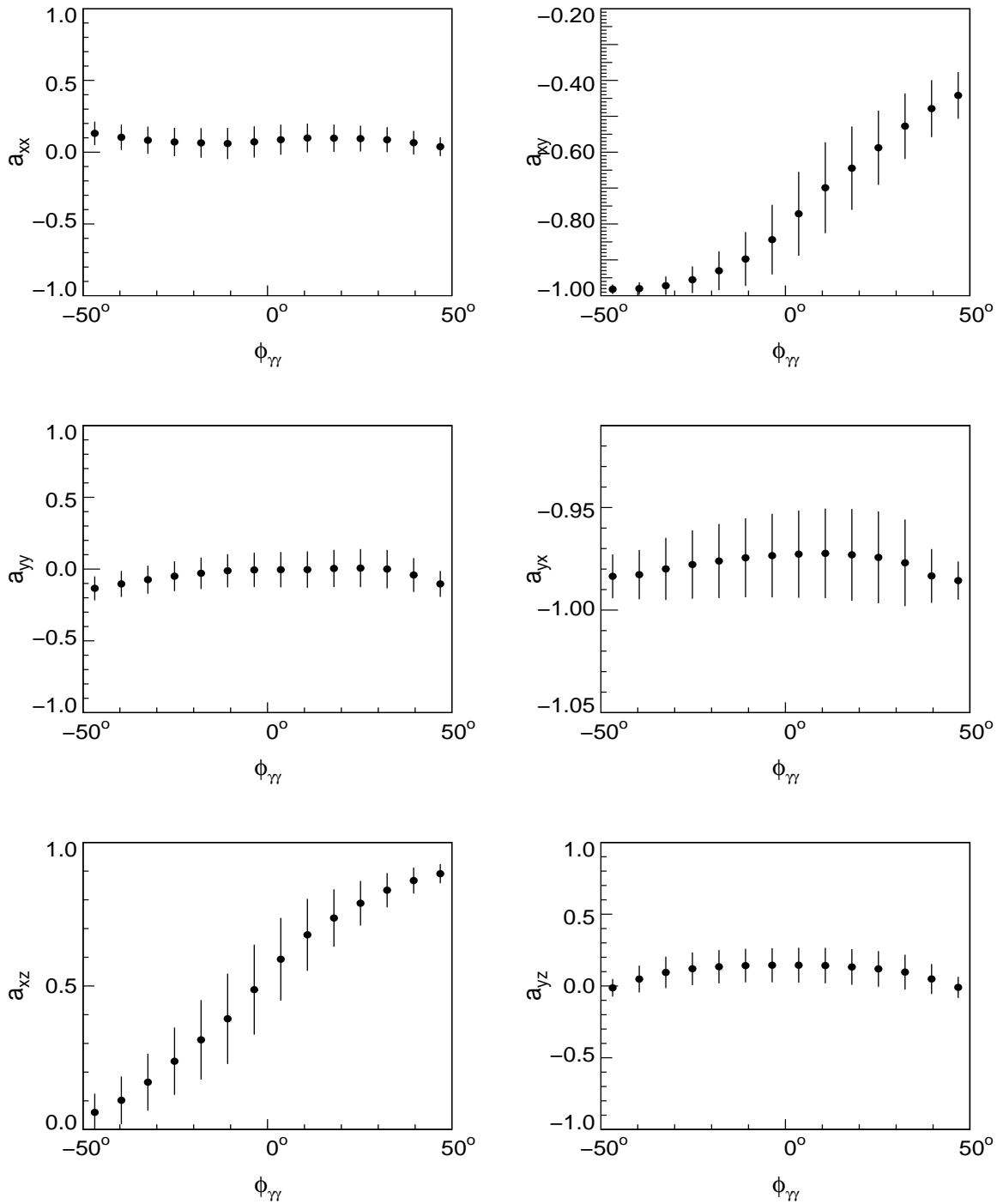


Figure 6.5: Simulated matrix elements of the rotation matrix \mathbf{R} : the coefficient a_{xy} is strongly asymmetric in respect to the out-of-plane angle ϕ_{γ} . This causes a bias in the mean value of the reconstructed P_y^{CM} component.

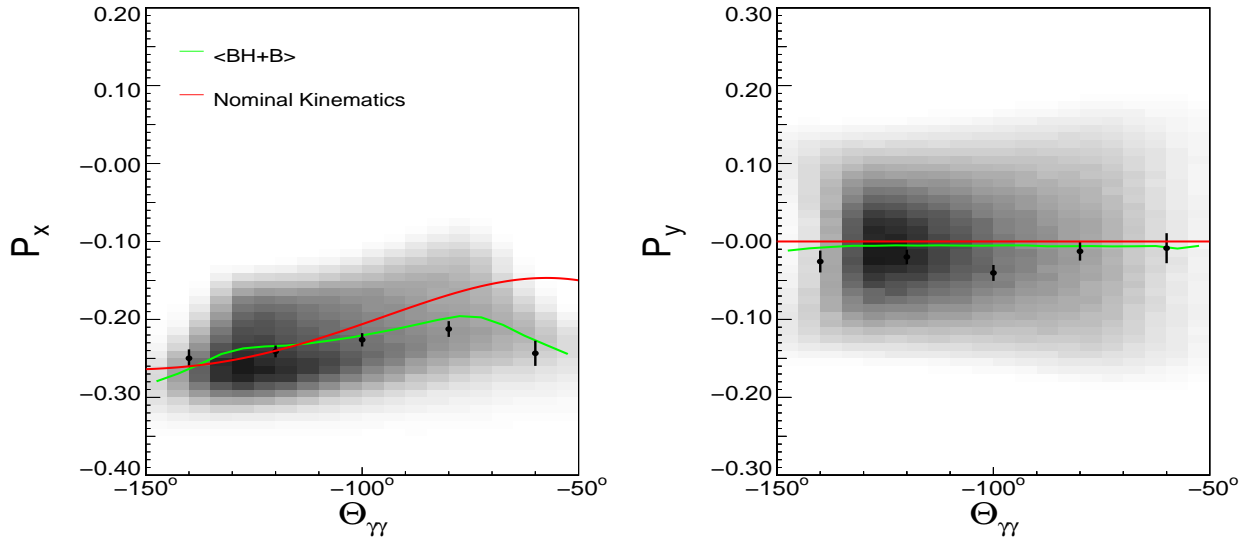


Figure 6.6: The reconstructed polarizations are compared to the theoretical ones, weighted with the matrix element a_{xy} for every event. The asymmetry in the rotation between out-of-plane events with $\phi_{\gamma\gamma} > 0$ or $\phi_{\gamma\gamma} < 0$ results in a lowering of the P_y^{CM} component, while P_x^{CM} remains almost unchanged. The remaining disagreement is mainly due to the analyzing power, which is different for every event.

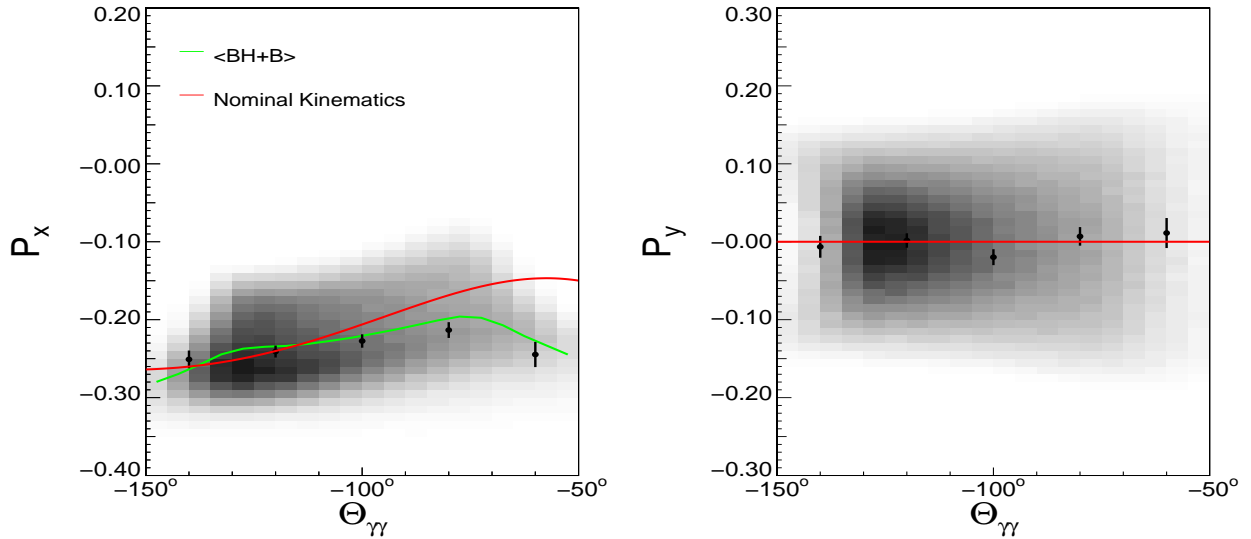


Figure 6.7: Reconstructed P_x and P_y polarizations with corrected P_y ($5 \cdot 10^5$ events)

6.5 Summary

A simulation of the whole fitting procedure was performed for investigating if the algorithm based on a maximum likelihood method is working. All the transformations needed in order to bring the polarization vector from the CM frame to the focal plane polarimeter are taken into account, including the spin precession in the magnetic field of the spectrometer. The following points summarize the results of the simulation.

- The reconstructed polarizations should be compared with the mean polarization on the accepted phase space of the spectrometers
- The previous point is exactly valid if the polarization vector is fitted in the focal plane.
- The simultaneous fit of the three polarization components is very difficult for the considered kinematics, so the theoretical value for one of them is used for constraining the fit.
- As it can be expected, P_z^{CM} is the most difficult component to fit, because it enters the likelihood only indirectly through the spin precession.
- The fit of \vec{P}^{CM} is close to the mean theoretical value, but a small discrepancy remains: it is found that this discrepancy comes from a different rotation of the events above and under the scattering plane so, after the rotation, the maximum of the likelihood does not lie on the mean value, but a bias is introduced.
- Using P_z^{CM} as constraint, only P_y^{CM} is affected by the bias, which can be corrected with an overall offset in the fitting procedure, reconciling the reconstructed polarizations with the mean theoretical value.

Chapter 7

Data Analysis: Unpolarized Cross Section

Beauty is the purgation of superfluities.

Michelangelo

7.1 Introduction

In this chapter the data analysis for the unpolarized cross section is discussed.

For the data acquisition and analysis, different software packages are used which were specifically developed within the A1 Collaboration using the C++ language and object oriented techniques.

Aqua++ is the data acquisition program which reads the output of the detector electronics and constructs the raw data files.

Simul++ is the A1 simulation package. With its aid, the accepted phase space distribution can be simulated. Also different physical reactions can be simulated including the detector resolution effects and energy losses. The energy losses can be due to detector materials and also to radiative corrections.

Lumi++ This program is used in order to calculate the effective luminosity of a run of datataking. The calculation uses the constants in Eq. 7.5, 7.6 and the beam current information. The result is corrected for the dead time which arises mainly from the acquisition electronics while from the detectors comes practically no contribution.

Cola++ Is the analysis package, which reconstructs fourvectors from the raw data and applies all the energy loss corrections in the target, in the spectrometer materials and in the detectors. The reconstruction of the particle fourvectors implies also the tracking in the drift chambers and the use of the transfer matrices of the magnetic optics for connecting the events measured in the focal plane to the target frame.

Within this program, also the Euler angles for the polarization precession in the spectrometer magnetic fields are calculated.

7.2 Kinematical Setups

The datataking periods and the used kinematical setups are summarized in table 7.1. The setup VCS90 was chosen for maximizing the expected effect of the generalized polarizabilities in respect to the expected number of events: while the GP effect grows with q' , the event statistics decreases. With the chosen kinematics, a reasonable compromise between the two tendencies was found [61].

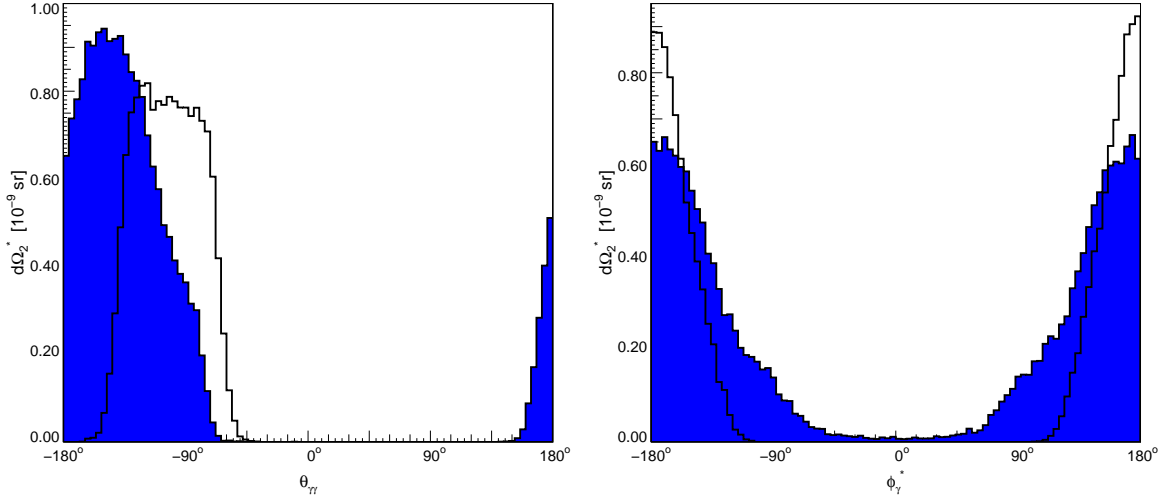


Figure 7.1: Simulated phase space for the VCS90 and VCS90b (shaded histogram) setups. The VCS90b setup has a larger $\theta_{\gamma\gamma}$ and $\phi_{\gamma\gamma}$ coverage.

Period	Setup	E_{Beam} (MeV)	Spec A		Spec B	
			q_c (MeV/c)	Angle	q_c (MeV/c)	Angle
April 05	VCS90	855	620	34.1°	546.0	50.6°
July 05	VCS90	855	620	34.1°	546.0	50.6°
November 05	VCS90b	855	645	38°	539.0	50.6°
April 06	VCS90	855	620	34.1°	546.0	50.6°
July 06	VCS90b	855	645	38°	539.0	50.6°

Table 7.1: Setups used for the VCS measurement. q_c is the central momentum of the spectrometer.

The setup VCS90b uses a higher proton momentum: this implies a different coverage of the phase space as shown in Fig 7.1: the setup VCS90b covers higher values of the $\theta_{\gamma\gamma}$ variable, giving access to a larger region and this will be necessary for the Rosenbluth separation [62] and therefore the determination of $P_{LL} - \frac{1}{\epsilon}P_{TT}$ and P_{TT} . The cross sections calculated in this work are relative to the first three beamtimes, while the determination for the last two beamtimes is in progress.

7.3 Cross Section Determination

The number of event counts in one chosen bin is

$$N_{exp} = \int \mathcal{L}_{exp} \frac{d\sigma}{d\Omega} d\Omega + N_{bkg}, \quad (7.1)$$

where \mathcal{L}_{exp} is the experimental luminosity, $d\Omega$ the phase space and N_{bkg} the number of background events. If we consider a constant luminosity inside the bin

$$N_{exp} = \mathcal{L}_{exp} \frac{\int \frac{d\sigma}{d\Omega} d\Omega}{\int d\Omega} \int d\Omega + N_{bkg} = \mathcal{L}_{exp} \left\langle \frac{d\sigma}{d\Omega} \right\rangle \Delta\Omega + N_{bkg}, \quad (7.2)$$

where the mean cross section inside the bin $\langle \frac{d\sigma}{d\Omega} \rangle$ and the total phase space in the bin $\Delta\Omega$ are introduced. The experimental cross section can be finally written, if we consider it nearly constant inside the bin as

$$\frac{d\sigma}{d\Omega_{exp}} = \frac{N_{exp} - N_{bkg}}{\mathcal{L}_{exp}\Delta\Omega}. \quad (7.3)$$

The phase space factor $\Delta\Omega$ accounts for the finite detector acceptance and it is calculated by simulation (**Simul++**) including resolution effects and radiative corrections. The luminosity \mathcal{L}_{exp} integrated over the whole measurement time T (integrated luminosity) is defined in a fixed target experiment as

$$\mathcal{L}_{exp} = \int_0^T L(t)dt = N_e N_t, \quad (7.4)$$

with

$$N_e = \frac{1}{e} \int_0^T I(t)dt, \quad (7.5)$$

$$N_t = \frac{\rho \bar{x} N_A}{A}. \quad (7.6)$$

N_e is the number of electrons hitting the target, N_t is the number of target particles per cm^2 and $L(t)$ is the instantaneous luminosity at time t .

The number of incoming electrons is calculated integrating the beam current divided by the elementary charge e . The beam current is continuously measured by a Förster probe.

Target Density

The luminosity depends on the target density which must be kept as constant as possible. The heating power of the beam should not be concentrated only on one point of the target for avoiding local temperature fluctuations. This aim is reached deflecting alternatively the beam in the x and y directions by ~ 2 mm with a sinusoidal signal of ~ 10 kHz. Hydrogen is maintained in the liquid subcooled phase by means of a Philips cooling machine. Local boiling of the liquid has to be avoided with care, because the formation of bubbles results in a sudden decrease of the density which implies a wrong calculation of the luminosity and then in too low measured cross sections. The beam can deposits in his travel through the relatively long target (49.5 mm) up to 2W of power. Using the Landau theory for energy losses, the most probable value is around 1W of power transfered from the beam to the hydrogen. The target temperature is constantly measured by two temperature sensors and also the corresponding pressure is measured. Knowing temperature and pressure the liquid hydrogen density can be calculated using *e.g.* the equation of state ¹.

¹In particular, the method employed for the calculation of the density is based on the Hankinson-Thomson model for saturated liquid density (also known as COSTALD) which is more precise in respect to methods based on an equation of state (for a general discussion see *e.g.* [71]). Typical values for the target temperature and pressure are 21.9K and 1987mbar which correspond to a density of 0.688 g/cm^3 .

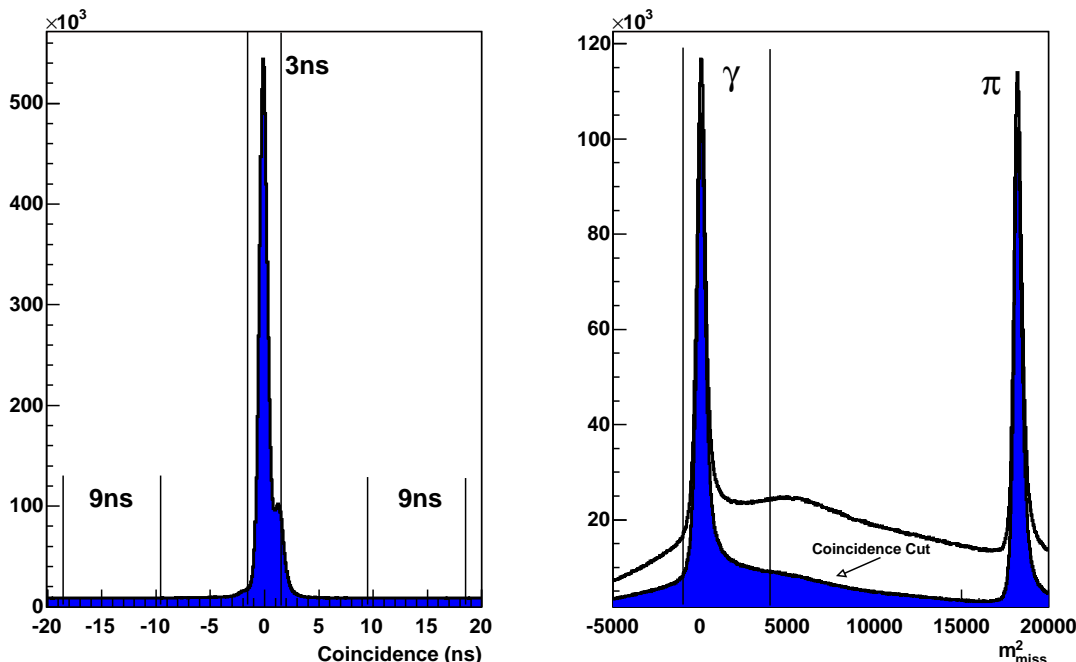


Figure 7.2: Left: Coincidence time spectrum. Two peaks are visible: a main peak for the signal events and a smaller one due to slower particles entering spectrometer B. The smaller peak is fully removed using the Čerenkov detector or (as in this work) a cut on the missing mass spectrum. For the signal selection a time window of 3ns was chosen. The background estimation windows are 9ns wide and 14ns away from the coincidence.

Right: Squared missing mass spectrum. The peak due to photons ($m_{miss}^2 = 0$) and that due to pions are clearly separated. A cut around the photon peak selects the photon electroproduction events after the cut in coincidence time. The effect of the coincidence time is also shown, demonstrating the high background reduction.

7.4 Particle Identification

In this experiment, protons are detected by spectrometer A and electrons by spectrometer B. The identification is mainly done through timing coincidence between the two spectrometers and it is given by the fast scintillator signals. The time difference is then corrected for the time of flight (for example in spectrometer A the maximum difference between two different particle paths can be of 3 m) and for the different cable lengths of the scintillator paddles. The corrected timing spectrum is shown in Fig. 7.2 (left). Two peaks are visible: the main peak corresponds to coincidences between protons and electrons while the second smaller peak is due to coincidences between protons and pions entering spectrometer B (which are slower in respect to electrons). A cut using the Čerenkov detector of spectrometer B fully removes the peak, proving its origin.

A cut of ± 1.5 ns is applied on the coincidence timing peak. Not only electrons and protons can enter the spectrometers (as seen also by the timing spectrum), but also other charged particles, e.g. pions or muons.

In order to distinguish them, the scintillators and Čerenkov detector (only for spec-

trometer B: in spectrometer A the Čerenkov detector is replaced with the proton polarimeter) can be used.

In Fig. 7.3 (left and middle) the signal from the two scintillator layers of spectrometer A is shown: protons and other lighter particles are well separated. For the cross section measurement, a cut on the scintillator signal is not applied, because after coincidence and missing mass cuts (see next section) the contamination due to lighter particles is negligible. The same applies to the Čerenkov detector in spectrometer B: the pion contamination is negligible after the event selection and also this cut can be avoided. If these cuts are not relevant, as in this case, it is better to not use them, because scintillators and Čerenkov detectors have an acceptance slightly different from that of the drift chambers. For avoiding uncontrolled influences on the acceptance, the particle identification cuts are not used for the cross section analysis.

7.5 Reaction Identification

The coincidence cut selects the right particles entering the spectrometers, but the right reaction must be fixed. The reaction identification is performed through the missing mass technique. The squared missing mass is defined as

$$m_{miss}^2 = (k + p - k' - p')^2 \quad (7.7)$$

where k (k') is the fourvector of the incoming (outgoing) photon and p (p') is the fourvector of the target proton (outgoing proton).

In Fig. 7.2 (right) the squared missing mass spectrum is shown before and after the coincidence time cut. While only photons in the final state are requested, the cut $-1 < m_{miss}^2 < 4(MeV/c^2)^2$ is applied. The rather large cut applied for positive values of m_{miss}^2 accepts also a part of the radiative tail of the photon peak which contains true VCS events. The cut was determined enlarging it while checking that the cross section remains unchanged.

7.6 Target Walls

As it is visible in Fig. 7.4, the end caps in the z direction (laboratory frame) of the target give rise to two peaks corresponding to their position. In Fig. 7.5 the events in the walls are analyzed with the same cuts as for the determination of the cross section. A large pion production contribution is visible in the time spectrum as a small peak on the right side of the coincidence one: in the case of events in the center of the target, this peak is eliminated with a cut on the m_{miss}^2 variable, while here it is still present. From the inspection of the m_{miss}^2 spectrum for the wall events, a photon peak is also visible and this indicates that some good events are present, but the background is very high ($\sim 50\%$). We decide then to exclude from the analysis all the wall events because there is not a clear way in order to safely isolate the true photon electroproduction ones. Fitting the event distribution along the target

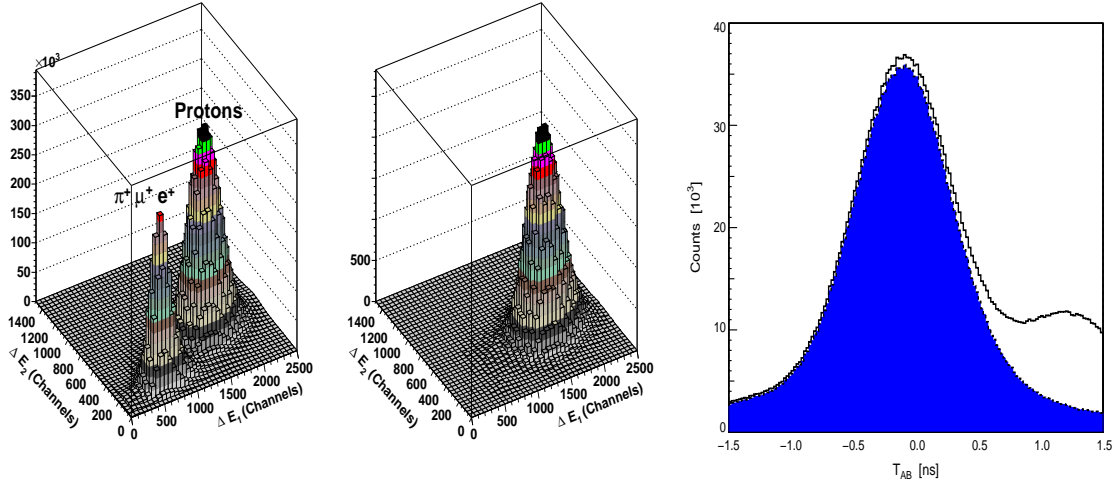


Figure 7.3: **Left:** Output signal for the two scintillator planes ΔE_1 and ΔE_2 without cuts. A peak due to protons and a peak due to lighter positive particles (π^+ , μ^+ , e^+) is visible. **Middle:** Output signal after coincidence and m_{miss}^2 cuts: the light particles contamination is almost removed. **Right:** With a cut in the Čerenkov detector the pion contamination disappears in the coincidence timing peak.

length (see Fig. 7.4), the position and width of the peaks can be estimated, then a cut is chosen to exclude them.

During the beamtimes, because of a not sufficiently high vacuum in the target vessel, there was also formation of snow around the target cell. This problem is particularly significant in the last parts of the beamtimes, where the accumulated snow formed a thick layer around the target, causing a different energy deposition of incoming electrons and of particles emerging from it. The effect is visible as a shift of the reconstructed missing mass as a function of the target length. A model for the snow layer is implemented in the analysis software, which takes into account the additional energy losses restoring a good event reconstruction.

7.7 Background Estimation

The background due to random coincidences is estimated selecting events outside the coincidence peak (see Fig 7.2). A time window of 4.5 ns is considered: one to the left, one to the right and 14ns away of the coincidence peak. The obtained background events are then subtracted to the coincidence events. Before subtraction, the background events are multiplied by a factor w_c/w_b where w_c and w_b are respectively the width of the coincidence (3 ns) and background (2×4.5 ns) timing windows.

The background spectrum of some of the most important kinematical variables is shown in Fig 7.6: they are obtained with the same cuts applied to signal events, but with time window as already described.

In the background events are present both protons and pions, but there is no pronounced peak in the missing mass spectrum.

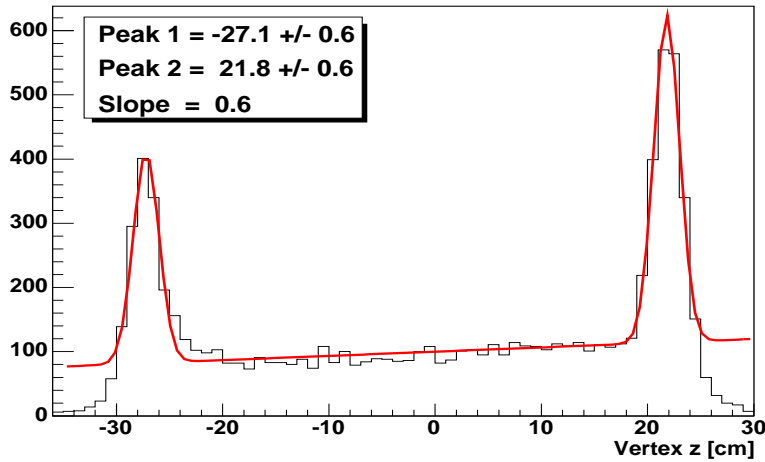


Figure 7.4: Target spectrum in the z_{lab} direction. The target walls are clearly visible: a cut on the peak position $\pm 2\sigma$ is used in order to select only the central region.

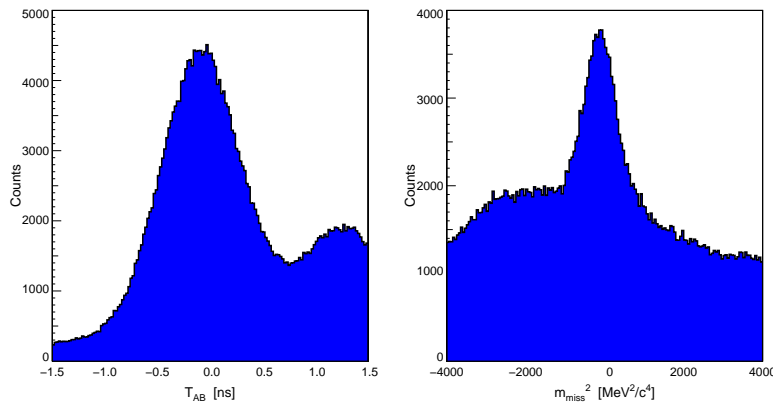


Figure 7.5: (Left) Timing spectrum of the wall events: a large contribution of pions is present. (Right) Squared missing mass spectrum: a photon peak is visible, but the background is large ($\sim 50\%$).

Other background can be present also in the coincidence peak, then it is not due to not coincident events, but to unwanted particles entering the spectrometer (pions, electrons, positrons) which are produced by reactions with a similar kinematics to the studied process. As seen before, the contamination is in any case practically absent and cuts for the elimination of unwanted particles in scintillator planes or Čerenkov detectors are avoided for not influencing the detector acceptance.

7.8 VCS Cross Section

The identification of the VCS events for the calculation of the cross section is realized mainly using the coincidence timing cut and the cut on the squared missing mass, in order to select only events where one photon is produced in the final state.

The kinematics is fixed selecting the momentum of the outgoing photon with the cut $q' = 90 \pm 10$ MeV/c. In Fig. 7.7 the spectrum of the reconstructed outgoing photon

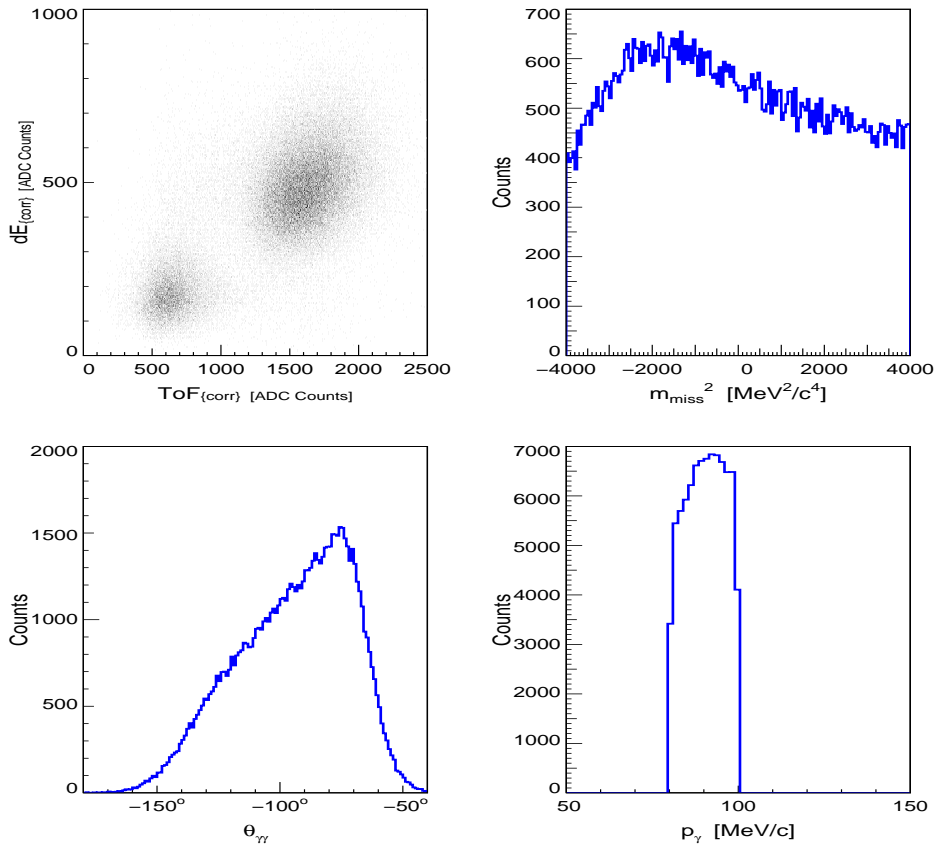


Figure 7.6: Background spectrum regarding the random coincidences for the scintillator planes (top left) and some of the relevant kinematical quantities of the VCS reaction.

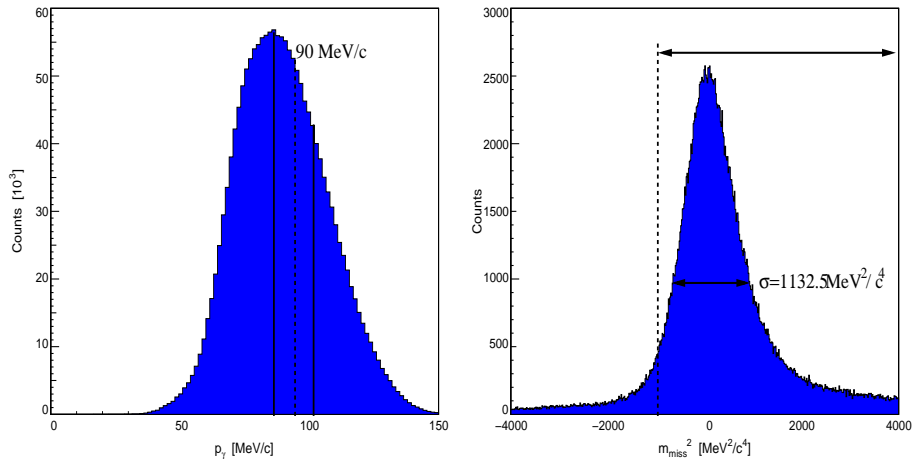


Figure 7.7: (Left) Experimental spectrum of the reconstructed real photon momentum after coincidence and missing mass cuts. The cut used for the determination of the cross section is shown: $p_{\gamma} = 90 \pm 10$ MeV/c. **(Right)** Final missing mass square spectrum after all the analysis cuts.

momentum is shown after coincidence and missing mass cuts. The unpolarized cross section is measured for the first three datasets corresponding to the periods of

Period	April05	July05	November05
Setup	VCS90	VCS90	VCS90b
Coincidence (ns)	± 1.5	± 1.5	± 1.5
M_{miss}^2 (MeV/c^2) ²	[-1,4]	[-1,4]	[-1,4]
Target Walls (cm)	[-23.1,17.6]	[-26.3,13.5]	[-18,18]
$\phi_{\gamma\gamma}$ Cut	-	-	[-180°, -110°] [110°, 180°]
Momentum Acceptance (A)	10%	10%	10%
Momentum Acceptance (B)	7.5%	7.5%	7.5%

Table 7.2: Cuts used in the unpolarized cross section analysis.

datataking listed in table 7.1.

The cross sections are found to be in agreement with the old VCS measurement done at MAMI [6] for the same kinematics of this experiment. Using the unpolarized cross section, two combinations of the generalized polarizabilities can be extracted with Rosenbluth separation [62]. The separation can cleanly be done only with enough lever arm for enabling a reliable linear fit and this happens only with a sufficient angular coverage in $\theta_{\gamma\gamma}$. The angular coverage of the VCS90 setups is not sufficient for the structure function separation ($\theta_{\gamma\gamma} \approx [-150^\circ, -50^\circ]$): this was the main motivation for measuring VCS also with the kinematics setup VCS90b, with a larger angular coverage $\theta_{\gamma\gamma} \approx [-180^\circ, -50^\circ]$. A large angular range will be also useful for the extraction of the generalized polarizabilities.

Right before the November 2005 beamtime the drift chambers of spectrometer A and B were repaired with substitution of “dead” wires and the replacement of the high-voltage foils: after this the chambers were installed again and a new calibration of the spectrometers was needed.

Particular care on the new calibration of the spectrometers was used in the VCS90b experiment of November 2005 [73] and this should be reflected in a good quality of the data, particularly for an absolute measurement like a cross section. Because of the large angular range and the quality of the calibrations, the data of this beam time were then used for extracting again the structure functions $P_{LL} - (1/\epsilon)P_{TT}$ and P_{LT} .

Analysis Cuts

The same main cuts are used in analyzing the various datasets. Some additional or modified cuts were in some cases needed and they are summarized in table 7.2. The cut for the target walls is different for the first two beamtimes, because the target was not mounted in the central position. This offset is taken into account also in the phase space simulation. In the case of the VCS90b setup, also a cut for excluding out of plane events is used, because in this case the acceptance in $\phi_{\gamma\gamma}$ is large.

7.9 Results

For the first three beamtimes the unpolarized cross sections were determined and compared with the results obtained in [6]. In Fig. 7.8, 7.9, 7.10 the measured cross sections are shown: they are found to be consistent with the previous measurements. From the cross section measured in the November 2005 beamtime the structure functions are extracted. The experimental unpolarized VCS cross section can be written as

$$\frac{d^5\sigma^{exp}}{dk'_{lab}d\Omega_{k'_{lab}}d\Omega_{p'}} = \frac{(2\pi)^{-5}k'_{lab}}{64M} \frac{s - M^2}{k_{lab}s} \mathcal{M} = \phi\mathcal{M} \quad (7.8)$$

and following the low energy expansion, the difference between the experimental amplitude and the known BH+B amplitude is

$$\Delta\mathcal{M}_0 = \mathcal{M}_0 - \mathcal{M}_0^{BH+B} = v_{LL} \left[P_{LL}(q) - \frac{1}{\epsilon}P_{TT} \right] + v_{LT}P_{LT}(q). \quad (7.9)$$

Since the BH+B cross section, given the proton form factors, is known, the structure functions

$$\begin{aligned} S_1 &= P_{LL} - \frac{1}{\epsilon}P_{TT} \\ S_2 &= P_{LT} \end{aligned} \quad (7.10)$$

can be extracted by means of a linear fit to the two variables

$$\begin{aligned} y &= \Delta\mathcal{M}_0/v_{LT} = (d^5\sigma^{exp} - d^5\sigma^{BH+B})/(\phi v_{LT}) \\ x &= v_{LL}/v_{LT} \end{aligned} \quad (7.11)$$

The results of the fit using the form factor parameterization of Mergell et al. [64] is

$$\begin{aligned} P_{LL} - \frac{1}{\epsilon}P_{TT} &= 25.6 \pm 2.9 \text{ GeV}^{-2} \\ P_{LT} &= -5.0 \pm 1.1 \text{ GeV}^{-2} \end{aligned} \quad (7.12)$$

and for the Friedrich-Walcher parameterization [72]

$$\begin{aligned} P_{LL} - \frac{1}{\epsilon}P_{TT} &= 25.3 \pm 2.9 \text{ GeV}^{-2} \\ P_{LT} &= -7.5 \pm 1.1 \text{ GeV}^{-2} \end{aligned} \quad (7.13)$$

The linear fits are shown graphically in Fig. 7.11 and 7.12.

Iteration Procedure

As discussed at the beginning of the chapter, the cross section is determined with the assumption that it does not vary strongly inside a bin. This approximation introduces a bias in the cross section determination. A procedure for avoiding the approximation was used in [73], correcting the cross section in the following way

$$N_{exp} = \mathcal{L}_{exp} \left(\frac{d\sigma}{d\Omega} \right)_0 \int \left[1 + \frac{\frac{d\sigma}{d\Omega} - \left(\frac{d\sigma}{d\Omega} \right)_0}{\left(\frac{d\sigma}{d\Omega} \right)_0} \right] d\Omega = \mathcal{L}_{exp} \left(\frac{d\sigma}{d\Omega} \right)_0 \underbrace{(\Delta\Omega_1 + \omega)}_{\Delta\Omega_2} \quad (7.14)$$

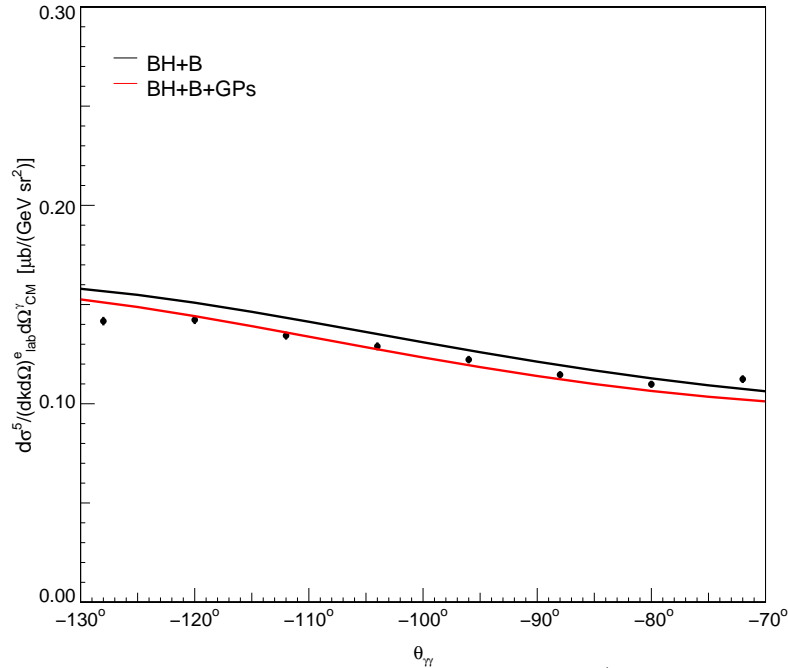


Figure 7.8: Experimental cross section for the VCS90 kinematics (April05 beamtime) The black curve corresponds to the BH+B calculation, the red curve is the result of [6]

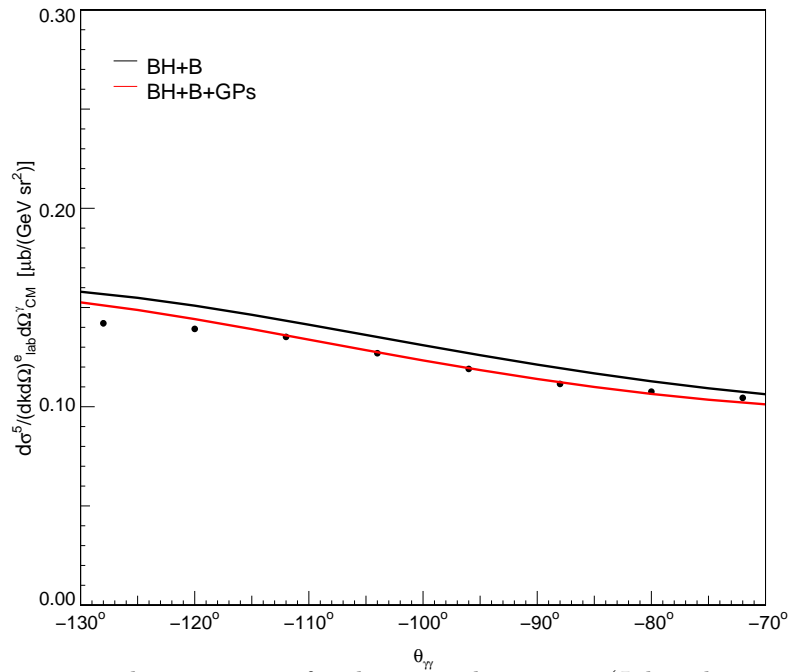


Figure 7.9: Experimental cross section for the VCS90 kinematics (July05 beamtime) The black curve corresponds to the BH+B calculation, the red curve is the result of [6]

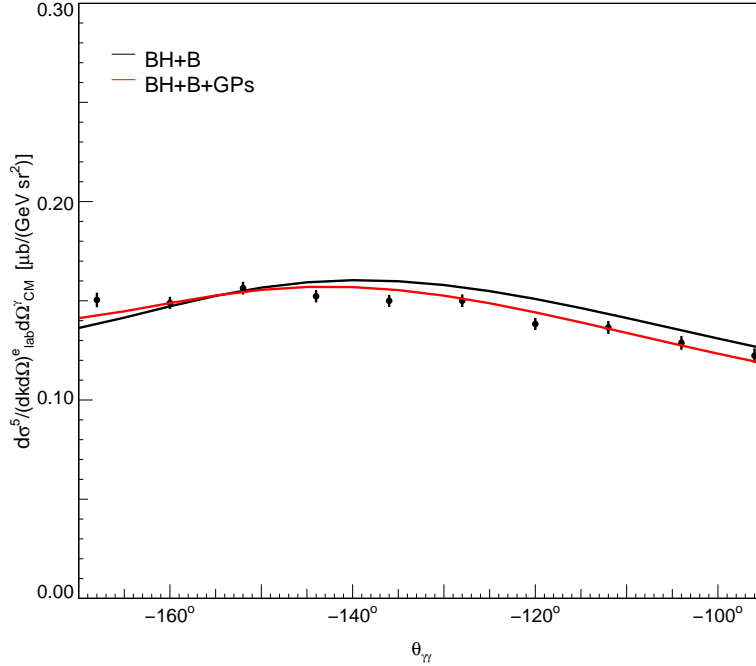


Figure 7.10: Experimental Cross Section for the VCS90b kinematical setting (data of November 2005). The black curve corresponds to the BH+B calculation, the red curve is the result of [6]

The new phase space factor $\Delta\Omega_2$ is calculated with an iterative procedure: in the first step the BH+B cross section is used, then, after the extraction of the structure functions, a first full VCS cross section is used for determining $\Delta\Omega_2$ again. The procedure is repeated until convergence for the values of the structure functions is found. The final result for the Mergell et al. parameterization is

$$\begin{aligned} P_{LL} - \frac{1}{\epsilon} P_{TT} &= 28.5 \pm 1.9 \text{ GeV}^{-2} \\ P_{LT} &= -5.2 \pm 0.7 \text{ GeV}^{-2} \end{aligned} \quad (7.15)$$

and

$$\begin{aligned} P_{LL} - \frac{1}{\epsilon} P_{TT} &= 27.1 \pm 1.9 \\ P_{LT} &= -8.0 \pm 0.7 \end{aligned} \quad (7.16)$$

for the Friedrich-Walcher parameterization.

7.10 Systematic Errors

The systematic error coming from the form factor parameterization was already treated before, performing a separate analysis of the structure functions extraction for two different parameterizations. The main sources of systematic errors are the spectrometer calibrations and the absolute normalization of the cross section.

In [73] a careful study of this effects and their impact on the extracted structure

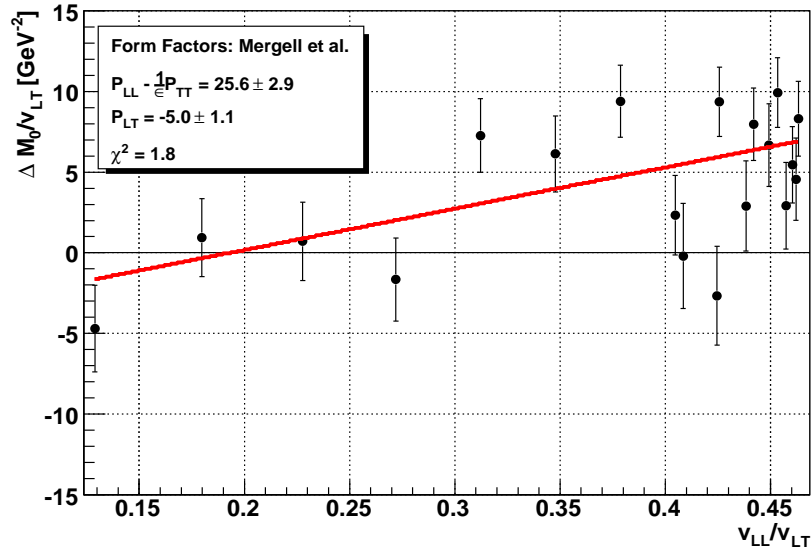


Figure 7.11: Separation of the structure functions with the Mergell et al. form factor parameterization [64]

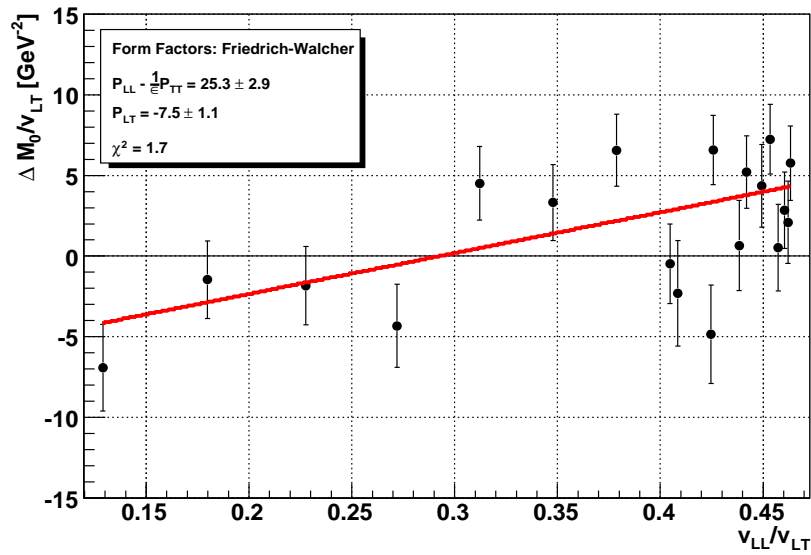


Figure 7.12: Separation of the structure functions with the Friedrich-Walcher form factor parameterization [72]

functions was done with the following result:

$$\begin{aligned} P_{LL} - \frac{1}{\epsilon} P_{TT} &\rightarrow \pm 2.7 \pm 0.6 \text{ GeV}^{-2} \\ P_{LT} &\rightarrow \pm 1.0 \pm 1.9 \text{ GeV}^{-2} \end{aligned} \quad (7.17)$$

where the errors are respectively the systematic errors coming from the spectrometer momentum calibration and from the absolute normalization of the cross section.

The error on the momentum calibration is estimated varying the spectrometer momentum inside the error bar which refers to the precision of the calibration itself, while the error on the absolute normalization is obtained varying the normalization in a 2% range, which is the estimated error on the phase space and luminosity calculation. For every variation of these two quantities a new extraction of the structure functions is done and then the range of their variation is taken as systematic error.

	$P_{LL} - \frac{1}{\epsilon} P_{TT}$ (GeV) ⁻²	P_{LT} (GeV) ⁻²
Theory (HB χ PT)	26.0	-5.4
MAMI 2000 ([6])	23.7 \pm 2.2 \pm 0.6 \pm 4.3	-5.0 \pm 0.8 \pm 1.1 \pm 1.4
This Exp. (Mergell et al.)	25.6 \pm 2.9	-5.0 \pm 1.1
This Exp. (Friedrich-Walcher)	25.3 \pm 2.9	-7.4 \pm 1.1
Iteration (Mergell et al.) [73]	28.5 \pm 1.9	-5.2 \pm 0.7
Iteration (Friedrich-Walcher) [73]	27.1 \pm 1.9	-8.0 \pm 0.7

Table 7.3: Final results for the separation of the structure functions.

7.11 Summary

The unpolarized VCS cross section is measured for the first three datataking periods finding good agreement with the first A1 measurement [6]. The data were analyzed in the framework of the low energy expansion (LEX) which permits the extraction of two combinations of the generalized polarizabilities, while an analysis based on the dispersion relation model [26] is in preparation [61]

The kinematical setup VCS90b measured in the period November-December 2005 is used for the extraction. Only this setup is used because of its large angular coverage needed for the Rosenbluth separation and for the good quality of the data. Before this beamtime the drift chambers of the spectrometers were repaired and a new calibration of their alignment was done.

The last two beamtimes show also good agreement with the already analyzed ones, but the precise determination of the cross section is still to be completed. The data are in any case useful for the polarization measurement which are not dependent from luminosity, efficiencies or detector acceptance issues.

The obtained results are reported in table 7.3 together with the results obtained in [73] with the use of the iteration procedure.

The first error is statistical, while the second is the full systematic error where the different contributions are summed quadratically.

The P_{LT} structure function is more sensitive to a form factor change: the ordinate in the linear fit depends directly on the cross section which is lowered by the use of the Friedrich-Walcher parameterization in respect to the use of the form factors of Mergell et al., as can be seen in Fig. A.1 in appendix A. The final results are found to be in general agreement with the first MAMI experiment [6] and with the predictions of HB χ PT at $O(p^3)$.

Chapter 8

Data Analysis: Double Polarization Observables

A man is like a fraction whose numerator is what he is and whose denominator is what he thinks of himself. The larger the denominator, the smaller the fraction.

Лев Николаевич Толстой

8.1 Introduction

The double polarization observable was introduced in Chapt. 2 and it is here reported for convenience as predicted by the low energy expansion (LEX)

$$\mathcal{P}_i = \frac{\mathcal{M}(\xi^e, \hat{i}) - \mathcal{M}(\xi^e, -\hat{i})}{\mathcal{M}(\xi^e, \hat{i}) + \mathcal{M}(\xi^e, -\hat{i})} = \frac{\Delta d^5 \sigma}{2d^5 \sigma} = \frac{\Delta d^5 \sigma^{BH+B} + \phi q' \Delta \mathcal{M}^{nBorn}(h, \hat{i}) + \mathcal{O}(q'^2)}{2d^5 \sigma}. \quad (8.1)$$

The denominator contains the result of the unpolarized analysis $d^5 \sigma$. The numerator contains, depending on the component (x,y,z), different structure functions, which are combinations of the generalized polarizabilities.

For a fixed beam polarization, the proton polarization is measured in the focal plane proton polarimeter installed in spectrometer A.

The procedure for the calculation of the polarizations was explained in detail in Chapt. 5 together with its extension to the fit of the generalized polarizabilities.

For the calculation of the proton polarizations the whole available dataset consisting in five beamtimes is used taking also advantage from a new carbon analyzing power measurement.

8.2 Measurement of the Carbon Analyzing Power

The knowledge of the carbon analyzing power $A_C(\Theta_s, E_p)$ is needed for measuring the proton azimuthal distribution in the HDCs and thus the polarization.

The analyzing power has to be determined experimentally and this can be done if the proton polarization is known.

This is the case of elastic $\vec{e}p \rightarrow ep$ scattering with polarized electrons, where the recoil proton polarization is exactly known and is given in the CM frame as

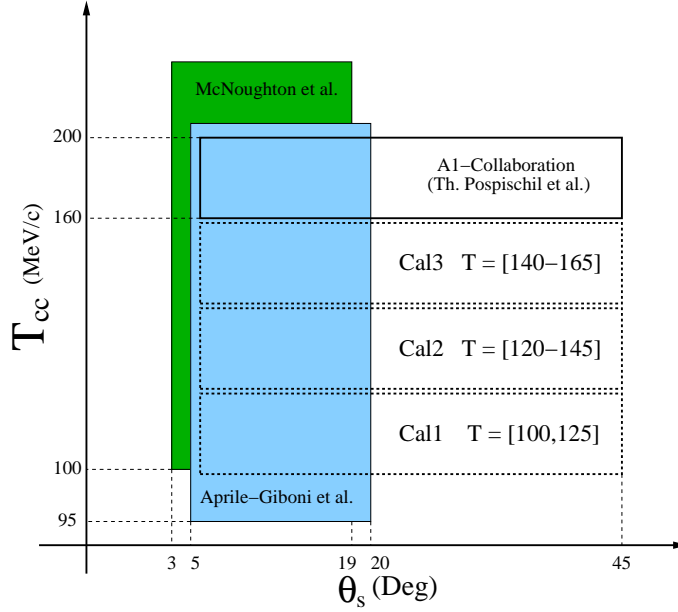


Figure 8.1: The existing analyzing power experiments together with the new ones in the $(T_{cc}-\Theta_s)$ plane. The scales on the axes are arbitrary.

$$\begin{aligned}
 P_x &= -2h \frac{\sqrt{\tau(1+\tau)} \tan \frac{\theta_e}{2} G_E G_M}{\sigma_0} P_b, \\
 P_y &= 0 \\
 P_z &= 2h\tau \frac{\sqrt{(1+\tau)(1+\tau \sin^2 \frac{\theta_e}{2})} \frac{\tan \frac{\theta_s}{2}}{\cos \frac{\theta_e}{2}} G_M^2}{\sigma_0} P_b
 \end{aligned} \tag{8.2}$$

with

$$\begin{aligned}
 \tau &= \frac{Q^2}{4M_p^2}, \\
 \sigma_0 &= G_E^2 + \tau G_M^2 \left[1 + 2(1+\tau) \tan^2 \frac{\theta_e}{2} \right],
 \end{aligned}$$

where P_b is the electron beam polarization and h the helicity.

In literature, experiments where $A_C(\Theta_s, E_p)$ was measured are already present (e.g.: [58],[60]), but they cover a limited part of the $(\Theta_s - E_p)$ plane. For enlarging the range available for polarimetry measurements, in [49] a new determination of $A_C(\Theta_s, E_p)$ including higher values of Θ_s was carried out, but in a limited range of E_p .

Double polarization VCS is a very demanding experiment regarding statistics and in order to enlarge the dataset, other measurements of the analyzing power were carried out in this work. In table 8.2 and graphically in Fig. 8.1, the actual situation about the knowledge of the carbon analyzing power is reassumed: the three new measurements are called **Cal1**, **Cal2** and **Cal3** with the corresponding kinematics

Experiment	Angular Range (Deg.)	Energy Range (MeV)
1. McNaughton et al. [58]	3-19	100-750
2. Aprile-Giboni et al [60]	5-20	95-570
3. A1@MAMI [49]	5-45	160-200
4. A1@MAMI Cal1	5-45	100-125
5. A1@MAMI Cal2	5-45	120-145
6. A1@MAMI Cal3	5-45	140-165

Table 8.1: Existing data on the carbon analyzing power measurements. The experiments 1 and 2 were extended in 3 to higher proton scattering angles. In the measurements 4,5,6 performed within the present work, the angular range is extended also for other energy values.

Setup	E_{Beam} (MeV)	q_p (MeV)	q_e (MeV)	θ_p	θ_e	T_c (MeV)
Cal1	855	569.9	697.0	54.0°	41.6°	113
Cal2	855	600.0	679.0	52.2°	44.3°	133
Cal3	855	630.0	663.0	50.3°	47.0°	153

Table 8.2: Kinematics for the three new analyzing power measurements.

listed in table 8.2.

Three proton kinetic energy T_c regions were measured with mean value $\bar{T}_c=113, 133$ and 153 MeV. The method used for calculating the analyzing power is directly based on the maximum likelihood method also used for the polarization reconstruction: the polarizations are in this case known and the likelihood is maximized in respect to $A_C(\Theta_s, E_p)$.

The procedure is repeated for the three setups and for every bin in Θ_s . In the following, the steps done by the algorithm, implemented in the `CalCAnpower` C++ code, are listed:

- The minimization algorithm chooses a value for A_C (E_p is considered fixed by the choice of the setup and a specific bin in Θ_s is used).
- On an event basis, the polarizations defined in Eq. 8.2 are calculated.
- The polarizations are transported to the focal plane with the transformation (Eq. 5.18) $\mathbf{R} = \mathbf{M} \circ \mathbf{S} \circ \mathbf{L}$ which includes the Lorentz boost from CM-frame to laboratory frame, the rotation to the spectrometer reference frame and the spin precession.
- Using the elastic polarization components in the focal plane P_x^{FP} and P_y^{FP} the likelihood can be calculated, using the beam helicity h and the azimuthal proton scattering angle Φ_s :

$$\ln \mathcal{L}(A) = \sum_{i=0}^N \ln [1 + h_i P_b A_{C,i} (P_{x,i}^{FP} \cos \Phi_{s,i} - P_{y,i}^{FP} \sin \Phi_{s,i})] \quad (8.3)$$

- The algorithm¹ varies A_C , until the maximum of $\mathcal{L}(A_C)$ is found.

¹As for the calculation of the VCS polarizations, a Simplex optimization algorithm is used

θ (Deg.)	A(T=120 MeV)	A(T=130 MeV)	A(T=150 MeV)
0	0.003 \pm 0.008	0.006 \pm 0.009	0.016 \pm 0.008
3	0.004 \pm 0.008	0.010 \pm 0.010	0.022 \pm 0.011
6	0.068 \pm 0.0148	0.104 \pm 0.020	0.149 \pm 0.021
9	0.237 \pm 0.0204	0.312 \pm 0.026	0.357 \pm 0.026
12	0.285 \pm 0.0202	0.352 \pm 0.025	0.460 \pm 0.256
15	0.284 \pm 0.0210	0.410 \pm 0.027	0.487 \pm 0.027
18	0.330 \pm 0.0233	0.382 \pm 0.030	0.482 \pm 0.030
21	0.360 \pm 0.0268	0.306 \pm 0.035	0.425 \pm 0.033
24	0.324 \pm 0.0317	0.325 \pm 0.010	0.320 \pm 0.036
27	0.300 \pm 0.0374	0.267 \pm 0.044	0.281 \pm 0.039
30	0.244 \pm 0.0440	0.222 \pm 0.048	0.113 \pm 0.041
33	0.280 \pm 0.0508	0.122 \pm 0.053	0.130 \pm 0.044
36	0.242 \pm 0.0587	0.019 \pm 0.060	0.016 \pm 0.048
39	0.215 \pm 0.0719	0.067 \pm 0.071	0.029 \pm 0.056
42	0.346 \pm 0.0880	0.136 \pm 0.089	-0.077 \pm 0.069

Table 8.3: Measured analyzing power in the three elastic setups.

a_{ij}	i=1	i=2
j=1	-0.038839	0.000346743
j=2	0.0251266	-0.000379229
j=3	-0.0119151	0.000176289
j=4	0.00101624	-1.36822e-05
j=5	-2.9514e-05	3.76534e-07
j=6	2.89796e-07	-3.54018e-09

Table 8.4: Coefficients resulting from the fit ($\chi^2/dof = 44.25/33 \simeq 1.34$) to the analyzing power data using the function 8.4

The results for A_C and the corresponding statistical errors are listed in table 8.3. This data is then used for determining a parameterization of the analyzing power in the new kinematical region. The data are fitted with the following two dimensional polynomial function

$$A_C(T_c, \Theta_s) = \sum_{i=1}^2 \sum_{j=1}^6 a_{ij} T_c^i([\text{MeV}]) \Theta_s^j([\text{°}]). \quad (8.4)$$

The fitted coefficients a_{ij} are determined with $\chi^2/dof \simeq 1.34$ and are listed in table 8.4.

In Fig. 8.2 one dimensional slices of the parameterization are shown together with the experimental data. The validity of the parameterization is up to $\Theta_s = 35^\circ$: at higher scattering angles the statistics becomes too low.

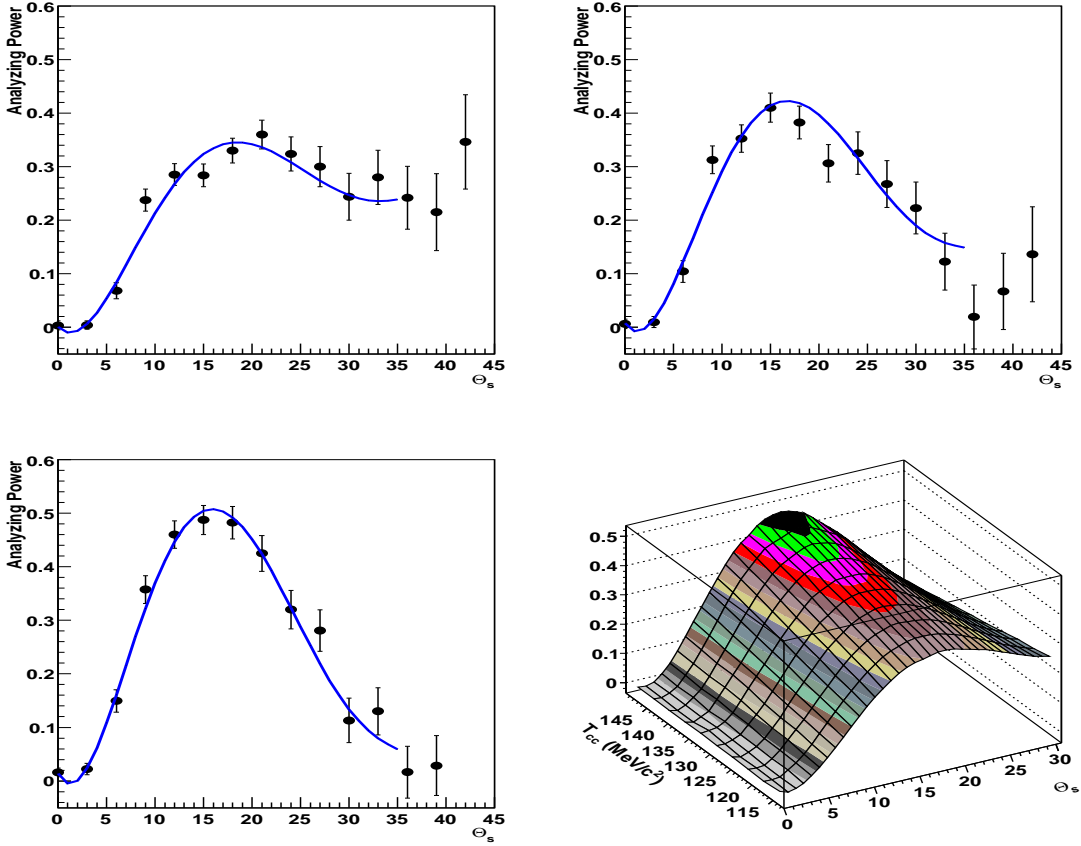


Figure 8.2: Carbon analyzing power fit results. **Top left:** $T=120$ MeV, **top right:** $T=130$ MeV, **bottom left:** $T=150$ MeV. In the **bottom right** figure a tridimensional representation of the obtained fitting function is drawn.

8.3 Analysis of the Polarimeter Events

Protons entering spectrometer A are tracked by the VDCs and after them they hit the secondary target which consists of a carbon plane. The scattering between a polarized proton and a ^{12}C nucleus is described by the cross section (see also Chapt. 5)

$$\sigma = \sigma_0(\Theta, E_p) [1 + P_b h A_C(\Theta_s, E_p) (P_y^{FP} \cos \Phi_s - P_x^{FP} \sin \Phi_s)] . \quad (8.5)$$

A large part of the events in the carbon plane are due to multiple scattering of protons in the material and are concentrated at small scattering angles Θ_s . These events do not contribute to the asymmetry in the azimuthal Φ_s distribution from which the polarization is extracted, so they have to be discarded. The cut $\Theta_s > 9^\circ$ is chosen, which discards almost all the multiple scattering events. In Fig. 8.3, histograms for the scattering angles Θ_s and Φ_s are shown together with the effect of the different cuts used:

- **VCDok and HDCok cuts:** For the reconstruction of the secondary scattering events, the coordinates of the proton have to be known before and after the carbon plane, so two cuts are introduced (conventionally called **VDCok** and **HDCok**) for requiring a good quality of the track reconstruction in the VDCs and HDCs (see also table 8.5).
- A small error in the VDC coordinates reconstruction is required: $\Delta x < 1$, $\Delta y < 1$, $\Delta \theta < 0.4$, $\Delta \phi < 2$
- **Carbon Plane Cut:** it requires that the polarimeter events effectively take place inside the carbon plane, so a cut is introduced for discarding wrongly reconstructed events or scattering events inside detector frames or other materials.

Using only the **VCDok** cut, the directions of the HDCs wires are clearly visible as spikes in the Φ_s spectrum. After all the cuts, the Φ_s distribution (for both beam helicities) is flat, as expected.

An additional cut in the $(\Theta_s - T_C)$ plane is used for selecting only the events for which the carbon analyzing power parameterization is known.

For identifying the VCS events a coincidence cut and a missing mass cut are introduced, as already done in the unpolarized cross section analysis. In this case the cut on the outgoing photon momentum q' and out of plane angle $\phi_{\gamma\gamma}$ are avoided for gaining more statistics: the change of the polarization as a function of q' and $\phi_{\gamma\gamma}$ is taken into account comparing the reconstructed polarization with the theoretical mean polarization over the accepted phase space (see. Chapt. 6).

Other cuts are introduced for eliminating the target wall (**TargetCut**) events and for accepting only events where the spin precession matrix is parameterized (**SpinTraceCut**).

In order to obtain the most cleaner set of events, also cuts in the scintillators of spectrometer A and in the Čerenkov detector of spectrometer B are applied.

The complete list of analysis cuts employed can be found in table 8.5.

Cut	Value	Description
VDCAok		VDCAok=1: The total hits in x_1 and x_2 is at least 3 The same for s_1 and s_2
VDCBok		The same for spectrometer B
HDCok		The event is accepted if it has one hit per plane and all positive drift times If two close wires give a signal but the sum of the drift times is $< 375\text{ns}$ the event is accepted If the above conditions are met, the event is accepted also if there are some hits with negative drift times. If two close wires have the sum of drift times $> 375\text{ns}$ and there are other wires with negative drift times, the tracking uses the wire with the shortest drift time.
VDCerror	$\Delta x < 1$ & $\Delta y < 1$ $\Delta\theta < 0.4$ & $\Delta\phi < 2$	Events with large reconstruction error are excluded
MomAcpt	$ \delta p_A < 10$ & $ \delta p_B < 7$	Cut on the spectrometer momentum acceptance
ApowCut		Cut on the accepted analyzing power, consistent with the known parameterizations ([60], [49] and Chapt.5)
FPPTheta		Cut on Θ_{FPP} , as discussed in the text
CarbonCut	$z > -20\text{cm}$ & $z < -4\text{cm}$	Cut on the z FPP coordinate: the secondary scattering should be inside the carbon plane
ScintCut		Cut on scintillator planes of spec. A
CerCut		Cut on Čerenkov detector of spec.B
TargetCut		The events in the target walls are excluded as for the cross section analysis
CoincCut	$ t_{coinc} < 1.5$	Coincidence Time Cut
MmassCut	$ m_{miss}^2 < 0.001 \text{ MeV}^2/c^4$	Missing Mass Cut
SpinTraceCut		This cut accepts only events in the kinematical region where the spin rotation matrix is defined (see Chapt. 5)

Table 8.5: Cuts used for the selection of the events used in the reconstruction of the proton polarization.

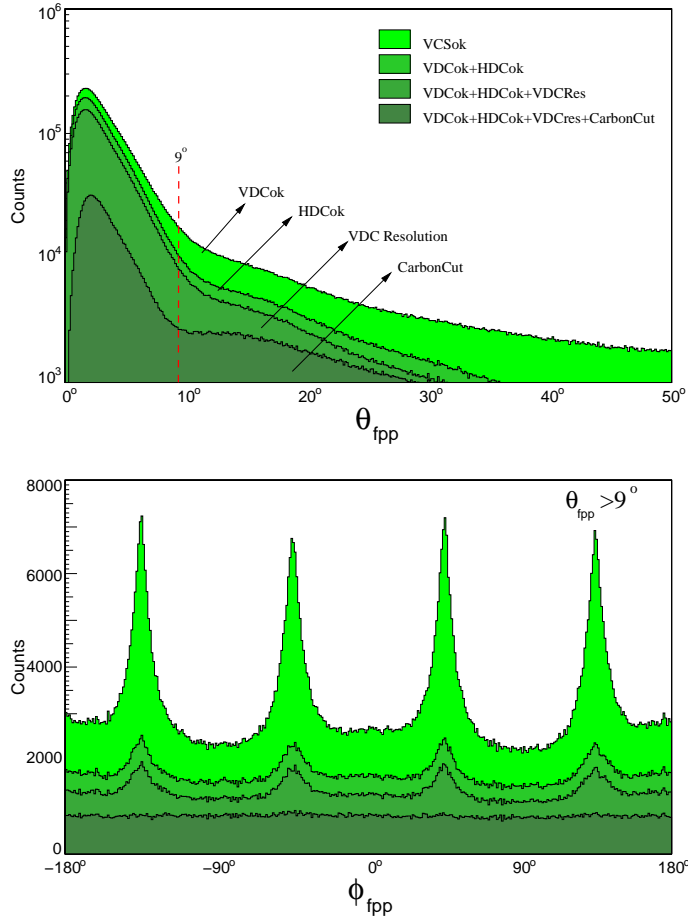


Figure 8.3: Distribution of Φ_s and Θ_s and the effect of the various cuts. At the end a flat Φ_s distribution is obtained.

8.4 False Asymmetries

For double polarization observables, false asymmetries are expected to be nearly absent, but a direct check is appropriate.

False asymmetries can arise for example from detector misalignments: this problem is minimized as well as possible by careful calibration of the HDCs, but a perfect alignment is never reached. Another source of false asymmetries can be the non-uniform efficiency of the drift chamber planes.

Once the false asymmetries are known, they can be included in the single event probabilities in the focal plane p_i adding them to the VCS polarizations:

$$p_i = \frac{1}{2\pi} \left[1 + (a_0 + P_b h_i A_C P_y^{FP}) \cos \Phi_{s,i} + (b_0 - P_b h_i A_C P_x^{FP}) \sin \Phi_{s,i} \right]. \quad (8.6)$$

The false asymmetries are encoded in the parameters a_0 and b_0 . It is not possible to calculate a priori this asymmetries of instrumental origin, so an experimental determination is required.

The method for the determination of the false asymmetries is based on the following observation: if we analyze a dataset without taking into account the beam helicity information $h = \pm 1$, we have to do with an effectively unpolarized beam: the final

$\theta_{\gamma\gamma}$ (deg)	P_x^{PCM}			P_y^{PCM}			P_z^{PCM}		
[-180, -162]	-0.173	\pm	0.219	-0.6165	\pm	0.395	-0.370	\pm	0.495
[-162, -144]	0.369	\pm	0.166	-0.0303	\pm	0.300	0.078	\pm	0.389
[-144, -126]	-0.016	\pm	0.122	0.3677	\pm	0.212	0.555	\pm	0.268
[-126, -108]	0.072	\pm	0.114	-0.1288	\pm	0.188	0.319	\pm	0.251
[-108, -90]	0.447	\pm	0.123	0.2797	\pm	0.190	0.419	\pm	0.262
[-90, -72]	0.351	\pm	0.129	0.3457	\pm	0.210	0.839	\pm	0.298

Table 8.6: Double polarization observable for the non coincident background in the center of mass frame.

proton asymmetries must disappear and what remains should be only of instrumental origin.

As an unpolarized dataset, the polarized one can be used, but without taking into account the beam polarization information h . In this case, the single event probability in the focal plane is

$$p_i = \frac{1}{2\pi} [1 + a_0 \cos \Phi_{s,i} + b_0 \sin \Phi_{s,i}] , \quad (8.7)$$

from which, by fitting the azimuthal Φ_s distribution, a_0 and b_0 can be estimated. Using the same dataset as for the proton polarization reconstruction, the following values for the false asymmetries are found:

$$a_0 = 0.043 \pm 0.016 , \quad (8.8)$$

$$b_0 = -0.001 \pm 0.016 . \quad (8.9)$$

The results demonstrate that the false asymmetries are effectively low and, their impact on the final results is negligible.

8.5 Polarization of the Background

As seen in the case of the unpolarized cross section analysis, the events are selected inside the coincidence peak between the two spectrometers.

An estimation of the background due to random coincidences was performed and the relative counts were subtracted from the signal events. Selecting the same timing window as for the background determination for the cross section, the contamination due to random coincidences in the polarization analysis is estimated to be $c=1.76\%$. The measured polarization P_{exp} is composed by a contribution from the signal P_s and one from the background P_b : $P_{exp} = (1 - c)P_s + cP_b$ and then

$$P_s = \frac{P_{exp} - cP_b}{1 - c} \quad (8.10)$$

The results reported in table 8.6 for each bin in $\theta_{\gamma\gamma}$ show the reconstructed background polarization. Applying Eq. 8.10, the effect on P_s is found to be negligible and it will not be considered further in the analysis.

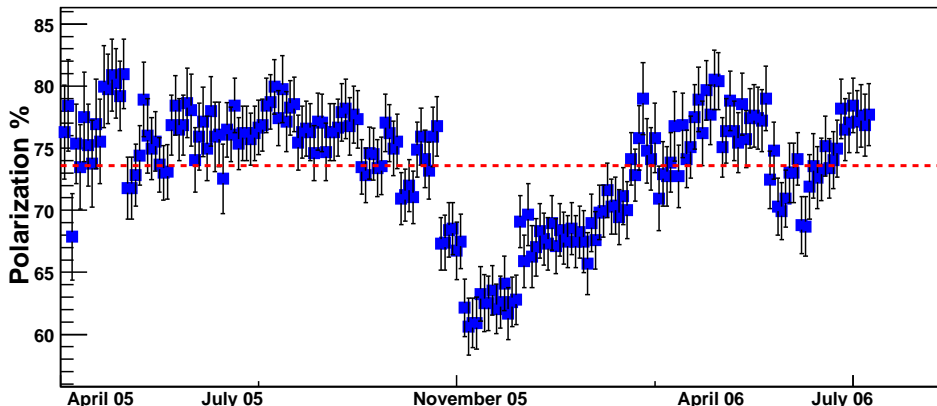


Figure 8.4: Electron beam polarization during the three beamtimes of 2005 and 2006. The measurement is repeated two times each day. The error bars are the sum of statistical and systematic errors. With the red dashed line, the mean value is indicated: $\langle P_{Beam} \rangle = 73.5$

8.6 Beam Polarization

The beam polarization was measured each day with the Møller polarimeter (Chapt. 4) installed directly in the beamline of the experimental hall before the target.

The achieved polarization degree is shown in Fig. 8.4 as a function of datataking time. The obtained polarization is of the order of 70-80% over the whole datataking period.

The mean error on the single measurements is ± 1.0 statistical (500 seconds of measurement) and ± 1.2 systematic. The systematic error comes mainly from the uncertainty on the Møller target polarization and its analyzing power. Work is in progress for lowering the systematic error of the polarimeter using detector hodoscopes with higher segmentation.

The beam polarization information is used only in the calculation of the double polarization observables, while for the cross section it is not needed: the two helicity states of the beam are equally taken into account with the result of having effectively an unpolarized beam.

8.7 Influence of the Beam Polarization on the Proton Polarization

The average beam polarization over the dataset used for the proton polarization calculation is

$$\langle P_{Beam} \rangle = 73.5 \pm 1.2 \quad (8.11)$$

The error is dominated by the systematical contribution.

For checking the dependence of the recoil proton polarization from the beam polarization, the following procedure was used: we fix an average value for the beam

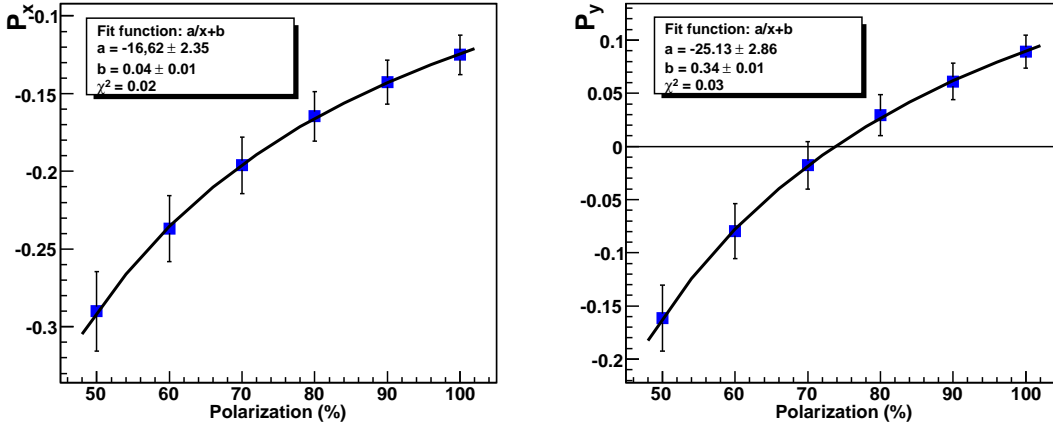


Figure 8.5: Proton Polarization dependence from Beam Polarization for the two components P_x^{CM} and P_y^{CM} . A fit is done in both cases for estimating the systematic dependence.

$\langle P_{Beam} \rangle$	$\langle P_x^{CM} \rangle$	$\langle P_y^{CM} \rangle$
100%	-0.125 ± 0.013	0.089 ± 0.016
90%	-0.143 ± 0.014	0.061 ± 0.017
80%	-0.165 ± 0.016	0.029 ± 0.019
70%	-0.196 ± 0.018	-0.018 ± 0.022
60%	-0.237 ± 0.021	-0.080 ± 0.026
50%	-0.290 ± 0.026	-0.161 ± 0.031

Table 8.7: Mean proton polarization reconstructed with different values for the mean beam polarization.

polarization and perform the fit² without binning, obtaining at the end a single value which is the mean proton polarization over all the accepted phase space. The procedure is repeated for six different mean beam polarizations in the range [50%, 100%] and the results are shown in table 8.7.

The experimental double polarization observable is expected to be proportional to $1/P_{Beam}$: the chosen fitting function is then $P_{exp} = a/P_{Beam} + b$. The fit results are shown in Fig. 8.7 and they confirm the expected behavior.

If the fitted curve on $\langle P_y^{CM} \rangle$ is used to calculate the value of $\langle P_{Beam} \rangle$ needed for having, as expected, $\langle P_y^{CM} \rangle = 0$, the following value is found

$$P_{Beam} = 73.9\% \pm 4.1 \quad (8.12)$$

which is consistent with the measured mean beam polarization given in 8.11.

²The fit is done using P_z^{CM} as given by the theoretical BH+B calculation. This constraint is also used for the polarization calculation as explained in the next section.

$\theta_{\gamma\gamma}$	P_x	P_y	P_z
-170°	-0.18 ± 0.05	-0.16 ± 0.01	0.23 ± 0.12
-150°	-0.27 ± 0.04	-0.10 ± 0.08	0.39 ± 0.10
-130°	-0.22 ± 0.03	-0.09 ± 0.06	0.52 ± 0.08
-110°	-0.21 ± 0.04	-0.11 ± 0.06	0.37 ± 0.08
-90°	-0.12 ± 0.05	-0.23 ± 0.08	0.21 ± 0.11
$P_z^{CM} = \text{BH} + \text{B}$			
-170°	-0.22 ± 0.05	0.05 ± 0.07	-
-150°	-0.26 ± 0.04	0.01 ± 0.05	-
-130°	-0.22 ± 0.03	-0.04 ± 0.04	-
-110°	-0.18 ± 0.03	0.02 ± 0.04	-
-90°	-0.07 ± 0.04	-0.02 ± 0.05	-
$P_y^{CM} = \text{BH} + \text{B}$			
-170°	-0.21 ± 0.05	-	0.39 ± 0.08
-150°	-0.27 ± 0.04	-	0.51 ± 0.07
-130°	-0.21 ± 0.03	-	0.63 ± 0.05
-110°	-0.19 ± 0.03	-	0.51 ± 0.05
-90°	-0.08 ± 0.04	-	0.48 ± 0.07

Table 8.8: Reconstructed proton polarizations in the CM frame. In the last two parts of the table the $P_z^{CM} = \text{BH} + \text{B}$ and $P_y^{CM} = \text{BH} + \text{B}$ constraints are used.

8.8 Proton Polarization

The events selected after the cuts discussed in the last section are then used for the extraction of the proton polarizations.

Additionally, the correction due to false asymmetries and the correction determined via the simulation in Chapt. 6 are used, while the background asymmetry is considered negligible.

The used dataset of all the available beamtimes results after all the analysis cuts in $\sim 9 \cdot 10^4$ events. As demonstrated by simulation, the use of a constraint for one polarization component is mandatory for achieving a good reconstruction: this is also visible in Fig. 8.6 where the data are used for fitting all the components.

In Fig. 8.7 and Fig. 8.8 the fit with, respectively, P_z^{CM} and P_y^{CM} fixed by the BH+B theoretical calculation is shown. The component P_z^{CM} is hard to reconstruct and probably more data are needed, while P_y^{CM} is reconstructed in good agreement with $P_y^{CM} = 0$ as expected. The component P_x^{CM} is easier to reconstruct, because it does not precess strongly in the magnetic field of the spectrometer. P_x^{CM} is also found to be systematically higher than the BH+B mean kinematical curve, indicating a contribution of the VCS process.

The P_x^{CM} component is nearly uncorrelated to the other two and this can be also appreciated observing that the result does not change regarding which constraint is used.

The results are presented in a restricted range of $\theta_{\gamma\gamma}$: $[-180^\circ, -80^\circ]$, where $\sim 7.5 \cdot 10^4$ total events are considered.

Values of the angle ($\theta_{\gamma\gamma} > -80$) are excluded because in this region the proton energy is low (also the analyzing power) and the track reconstruction in the HDCs is correspondingly not sufficient for a polarization measurement. This problem can be corrected in the future with a dedicated measurement with an optimized setup and eventually with a carbon plane of reduced thickness.

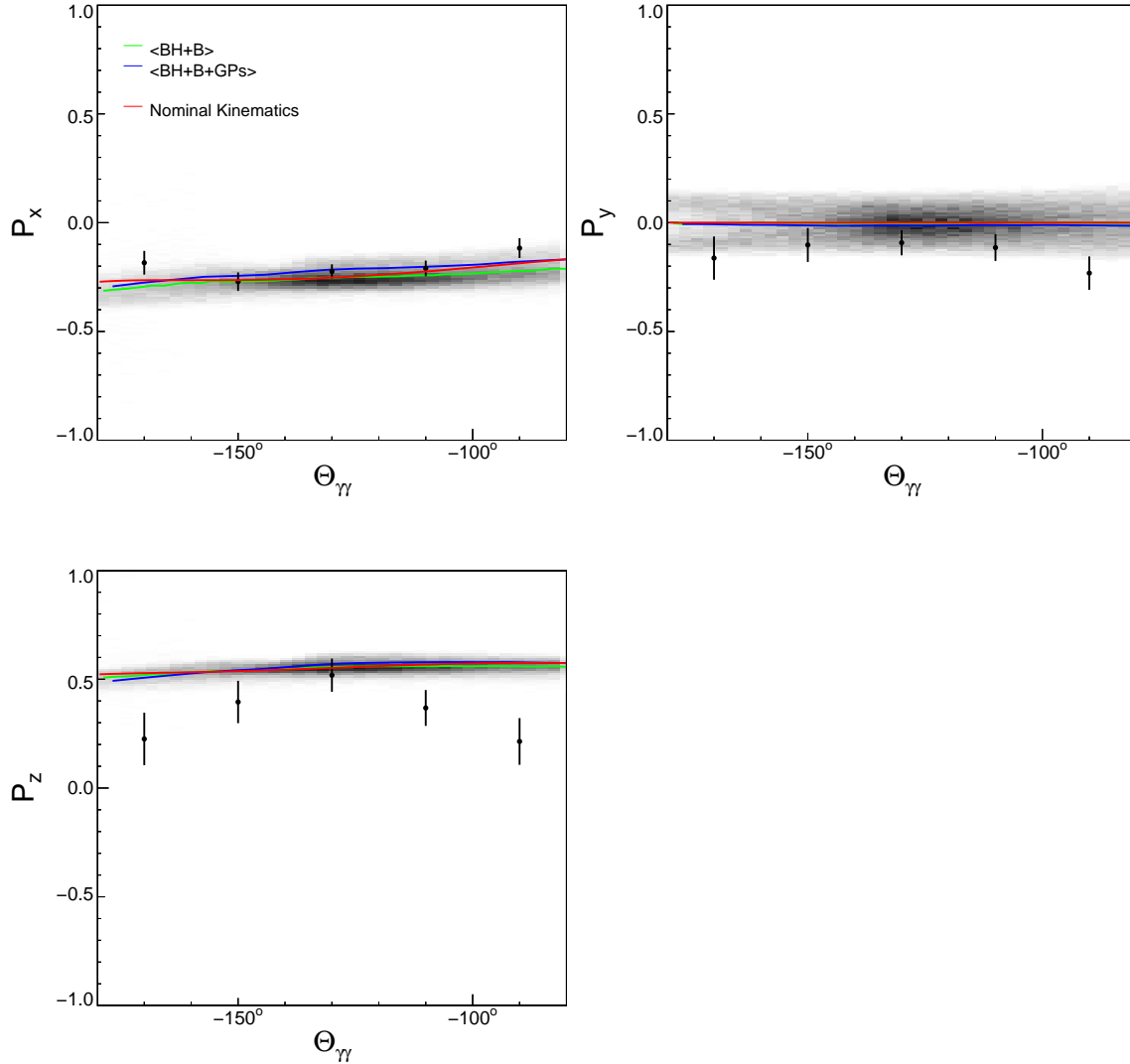


Figure 8.6: Polarization components in the center of mass frame calculated using all the available data. No constraint is used, and as already shown by simulation, a reliable reconstruction is difficult to achieve.

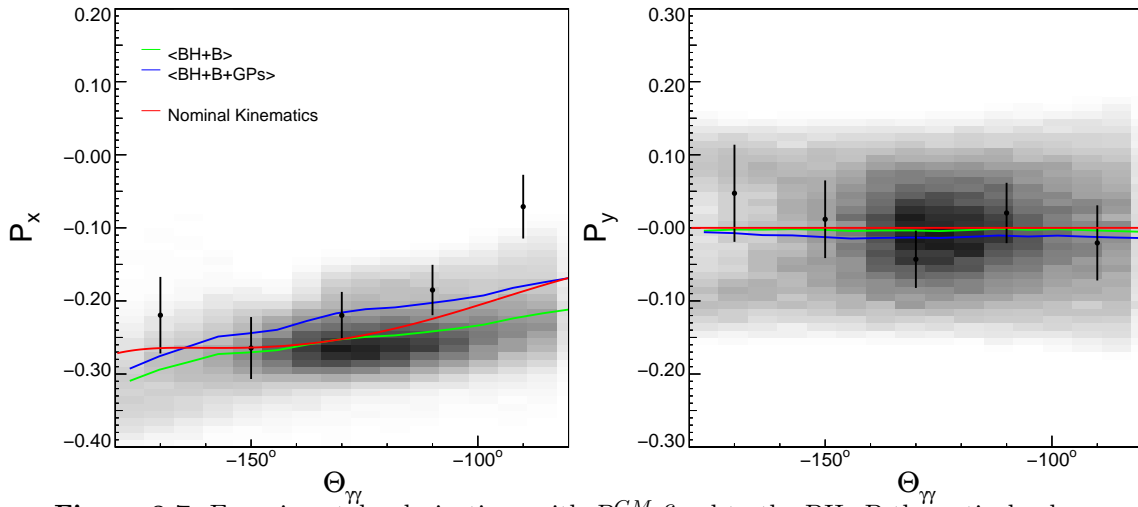


Figure 8.7: Experimental polarizations with P_z^{CM} fixed to the BH+B theoretical value

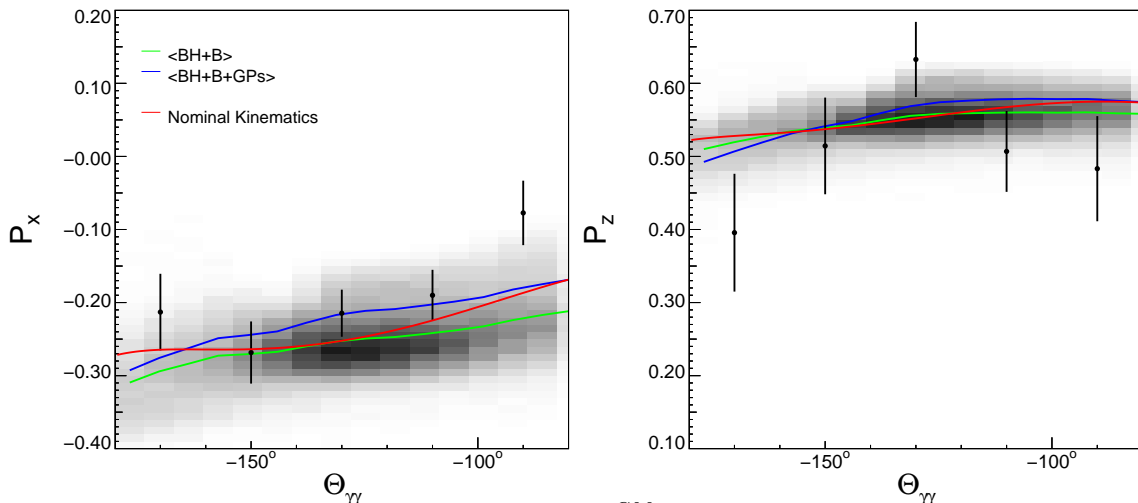


Figure 8.8: Experimental polarizations with P_y^{CM} fixed to the BH+B theoretical value

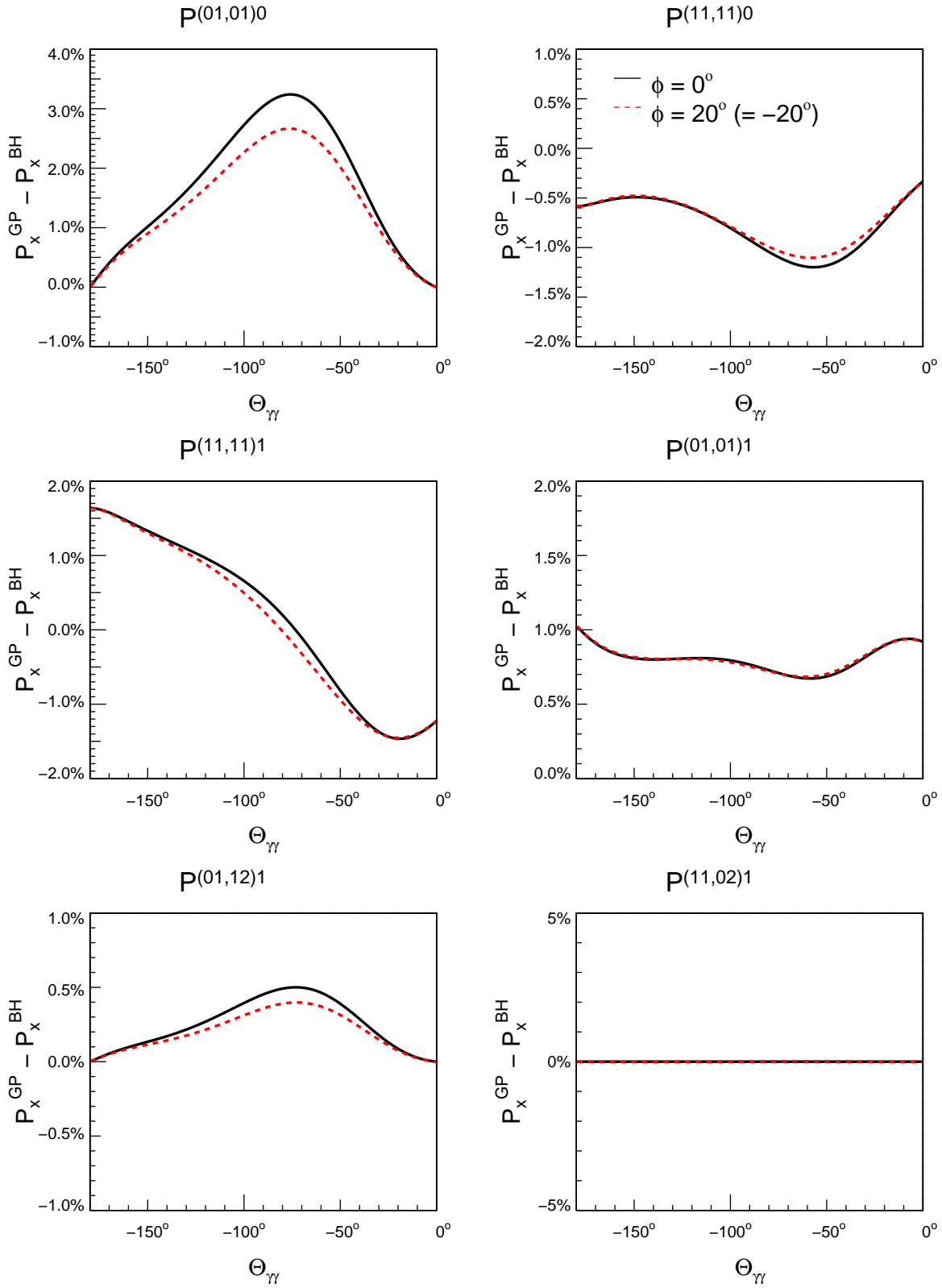


Figure 8.9: The effect of a single Generalized Polarizability on the P_x^{CM} component of the polarization is shown for $\phi_{\gamma\gamma} = 0$ (black solid line) and $\phi_{\gamma\gamma} = \pm 20^\circ$ (red dashed line).

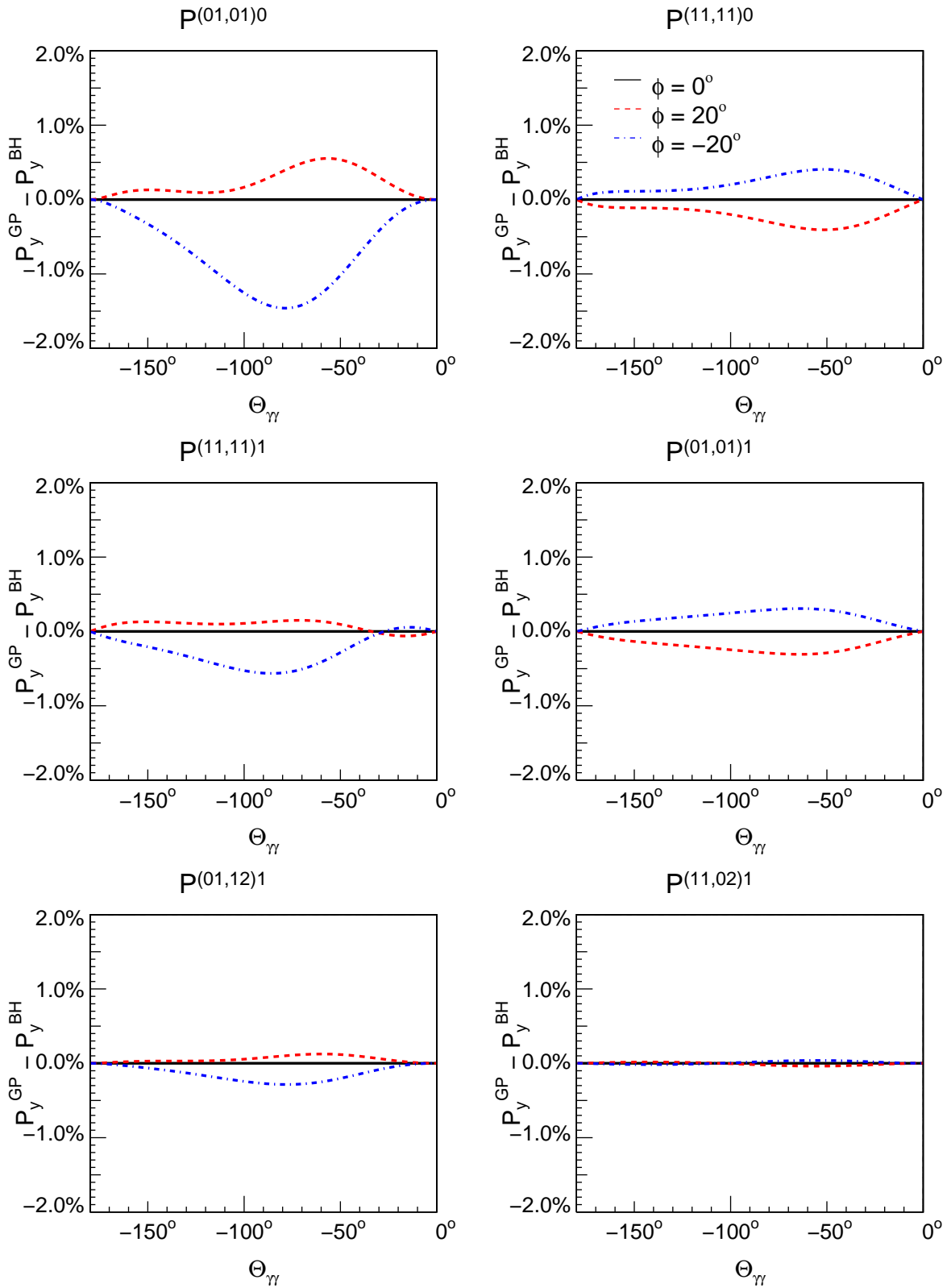


Figure 8.10: The effect of a single Generalized Polarizability on the P_y^{CM} component of the polarization is shown for $\phi_{\gamma\gamma} = 0$ (black solid line), $\phi_{\gamma\gamma} = 20^\circ$ (red dashed line) and $\phi_{\gamma\gamma} = -20^\circ$ (blue dot-dashed line).

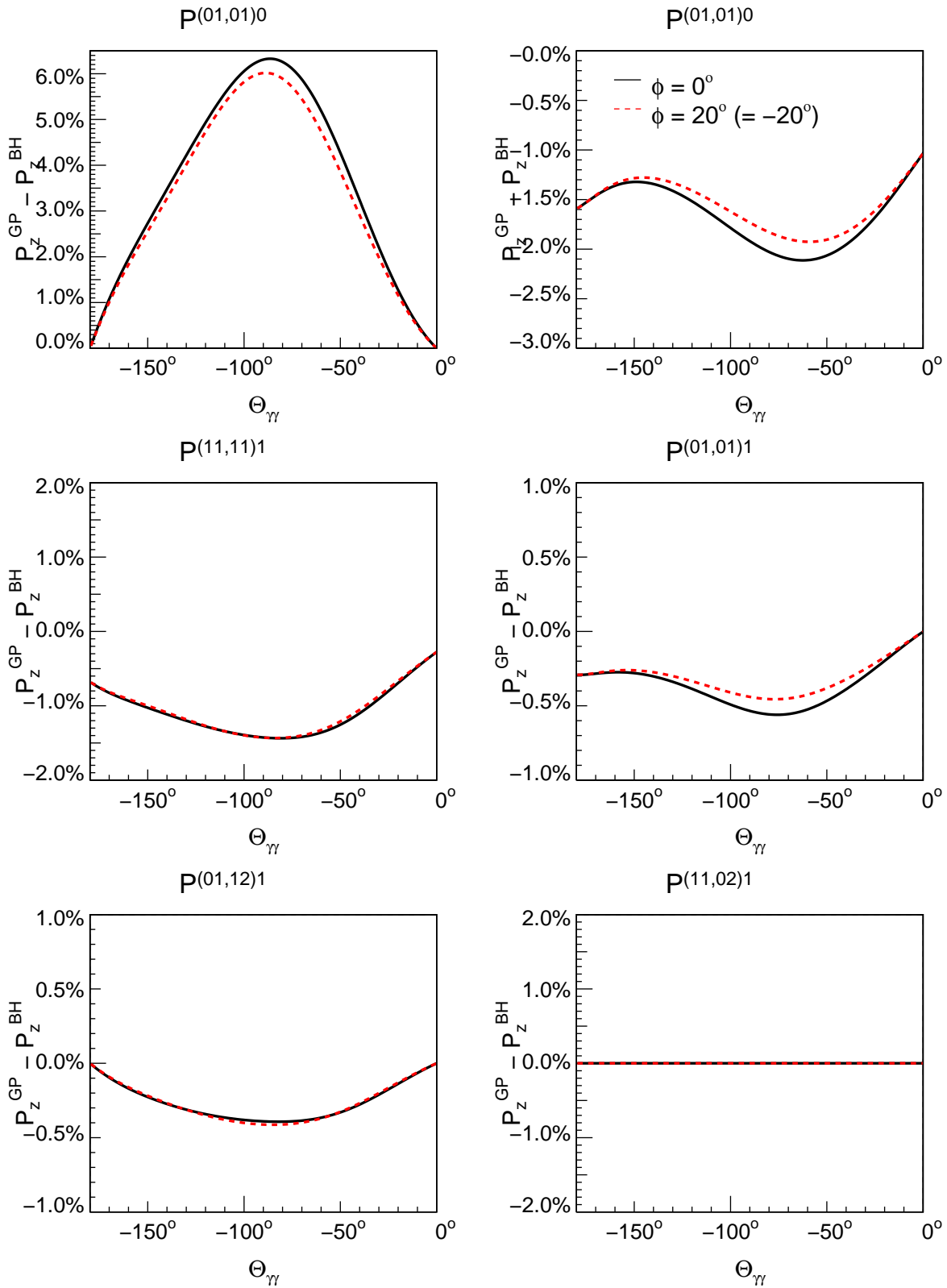


Figure 8.11: The effect of a single Generalized Polarizability on the P_z^{CM} component of the polarization is shown for $\phi_{\gamma\gamma} = 0$ (black solid line) and $\phi_{\gamma\gamma} = \pm 20^\circ$ (red dashed line).

8.9 Extraction of the Generalized Polarizabilities

A double polarization experiment gives the possibility to measure in principle all the generalized polarizabilities. Practically there are experimental limitations mainly due to the high statistics required and the need of out of plane measurements. In order to understand how much this experiment is sensitive to the different GPs, the Chiral Perturbation Theory model [22] is used for studying the quantity

$$\Delta P_{x,y,z}(\theta_{\gamma\gamma}) = P_{x,y,z}^{BH+B+GP_i}(\theta_{\gamma\gamma}) - P_{x,y,z}^{BH+B}(\theta_{\gamma\gamma}) \quad (8.13)$$

which represents the difference from the BH+B polarization component P_x^{CM} , P_y^{CM} , or P_z^{CM} given by the generalized polarizability GP_i ($i=1..6$) as a function of the angle $\theta_{\gamma\gamma}$.

The result is shown in Fig. 8.9, 8.10 and 8.11. In these figures, the effect of the single polarizabilities is shown for every polarization component in the case of an in-plane kinematics ($\phi_{\gamma\gamma} = 0$) and in two cases of out-of-plane kinematics ($\phi_{\gamma\gamma} = 180^\circ \pm 20^\circ$). Only in the case of P_y^{CM} the effect for opposite out-of-plane angles is different, while for P_x^{CM} and P_z^{CM} only the absolute value of the angle is important. From the figures some conclusions can be drawn:

- The polarizability $P^{(11,02)1}$ gives a negligible effect for every polarization component (also out-of plane)
- For the P_x^{CM} and P_z^{CM} components only $P^{(01,01)0}$, $P^{(11,11)0}$ and $P^{(11,11)1}$ give an effect above 1%
- The P_y^{CM} shows an overall low sensitivity to the polarizabilities
- P_z^{CM} has a rather strong sensitivity to $P^{(01,01)0}$ (proportional to the generalized electric polarizability)
- In general, a single polarizability can lower or enhance a polarization component.

As a first trial, we decide to fit the three generalized polarizabilities with the higher expected sensitivity, which are $P^{(01,01)0}$, $P^{(11,11)0}$ and $P^{(11,11)1}$. As an additional information, the result on the GP combinations obtained from the unpolarized cross section is used (see Eq. 8.1) and the P_z^{CM} component is fixed to the BH+B theoretical value, calculated for each event kinematics.

The result of the fit is shown in table 8.9. For investigating if the fit procedure is stable, 3 different starting points are used for the initial value of the GPs: the theoretical value of $HB\chi PT$ is multiplied by 1, 0 or -1. An inspection of the results shows clearly that the fitting procedure finds different results depending on the starting point and with large statistical errors. With the available data, it seems that there is not sufficient sensitivity for extracting in a consistent way the generalized polarizabilities. In the next section the problem is simplified through the direct fit of the structure functions instead of the generalized polarizabilities.

Init. Value	$P^{(01,01)0}$	$P^{(11,11)0}$	$P^{(11,11)1}$
(1, 1, 1)	-79.1±5.4	-20.0±12.6	-5.1±3.0
(0, 0, 0)	-57.5±26.7	42.2±25.2	-2.1±0.8
(-1, -1, -1)	-63.4±23.3	81.8±21.8	1.9±0.2

Table 8.9: Result of the fit for extracting three generalized polarizabilities

8.10 Extraction of the Structure Functions

Fitting the structure functions instead of the generalized polarizabilities is in principle easier because there are less kinematical coefficients involved and in this way many correlations between GPs are excluded in the fit (some structure functions contain the same GPs).

Having seen the impact of the single polarizabilities on the polarization components, it is also interesting to look at the sensitivity to the single structure functions. Recall that the effect due to VCS in the low energy expansion (LEX) approach is given by (see also Chapt. 2)

$$\Delta\mathcal{M}_x^{nB} = 4K_2(2h) \left\{ \begin{array}{ll} v_1^x \sqrt{2\epsilon(1-\epsilon)} P_{LT}^\perp(q) & + v_2^x \sqrt{1-\epsilon^2} P_{TT}^\perp(q) + \\ v_3^x \sqrt{1-\epsilon^2} P_{TT}'^\perp(q) & + v_4^x \sqrt{2\epsilon(1-\epsilon)} P_{LT}'^\perp(q) \end{array} \right\},$$

$$\Delta\mathcal{M}_y^{nB} = 4K_2(2h) \left\{ \begin{array}{ll} v_1^y \sqrt{2\epsilon(1-\epsilon)} P_{LT}^\perp(q) & + v_2^y \sqrt{1-\epsilon^2} P_{TT}^\perp(q) + \\ v_3^y \sqrt{1-\epsilon^2} P_{TT}'^\perp(q) & + v_4^y \sqrt{2\epsilon(1-\epsilon)} P_{LT}'^\perp(q) \end{array} \right\},$$

$$\Delta\mathcal{M}_z^{nB} = 4K_2(2h) \left\{ \begin{array}{ll} -v_1 \sqrt{1-\epsilon^2} P_{TT}(q) & + v_2 \sqrt{2\epsilon(1-\epsilon)} P_{LT}^z(q) + \\ v_3 \sqrt{2\epsilon(1-\epsilon)} P_{LT}'^z(q) & \end{array} \right\} .$$

Note that the structure functions in $\Delta\mathcal{M}_x^{nB}$ and $\Delta\mathcal{M}_y^{nB}$ are the same and in the current analysis $\Delta\mathcal{M}_z^{nB}$ is fixed to zero (i.e. the P_z^{CM} is calculated from the BH+B process only). Within this approach the maximum number of structure functions which are left is four: P_{LT}^\perp , P_{TT}^\perp , $P_{TT}'^\perp$ and $P_{LT}'^\perp$.

In Fig. 8.12 the effect of the single structure functions on $\Delta M_{0,i}$ (i=x,y,z) is investigated in the framework of the HB χ PT model [22]. From the obtained results some conclusions can be drawn:

- In the measured kinematical settings, the highest sensitivity is given by P_{LT}^\perp
- As known, for the in-plane kinematics, $P_y^{CM} = 0$ and then also $\Delta M_{0,y} = 0$
- Also for out of plane events, P_{LT}^\perp gives the bigger contribution, in this case also for the P_y^{CM} component
- The other structure functions give a rather small contribution and in particular the contribution of $P_{LT}'^\perp$ is practically negligible.

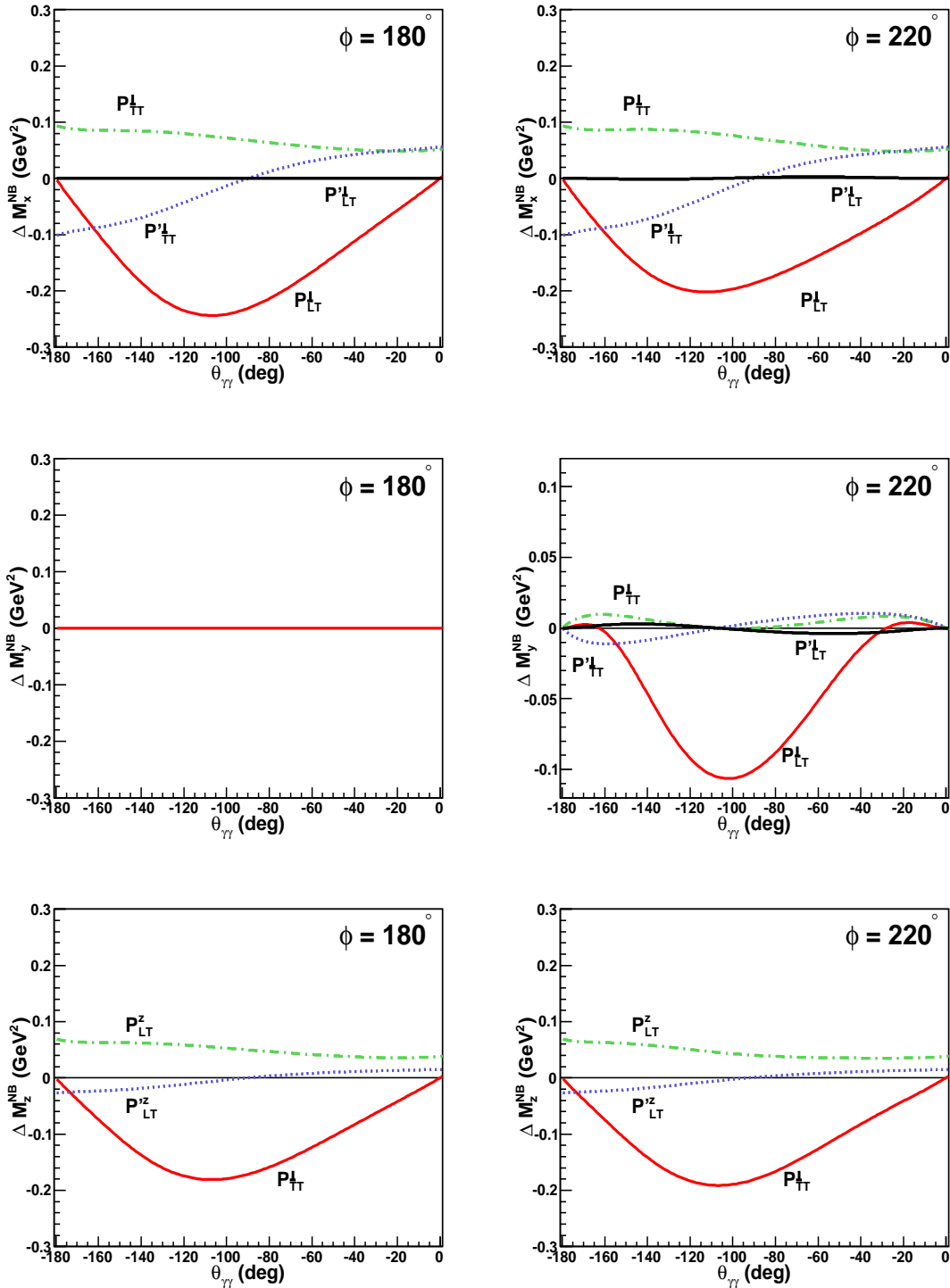


Figure 8.12: Effect of the single structure functions on $\Delta M_{0,x}$, $\Delta M_{0,y}$ and $\Delta M_{0,z}$. In the figures on the left the in-plane kinematics is shown, while in the figures on the right an out-of-plane angle of $\phi = 220^\circ$ is considered. For $\phi = 180^\circ$ the function $\Delta M_{0,y}$ is always zero.

Init. Value	P_{LT}^\perp (GeV $^{-2}$)	P_{TT}^\perp (GeV $^{-2}$)	$P_{TT}^{\perp'}$ (GeV $^{-2}$)
(1, 1, 1)	-13.6 \pm 2.0	2.1 \pm 1.5	3.3 \pm 3.5
(0, 0, 0)	-7.8 \pm 2.7	-2.5 \pm 1.5	1.1 \pm 2.2
(-1, -1, -1)	-5.4 \pm 0.9	-6.7 \pm 3.4	-1.7 \pm 1.3

Table 8.10: Result of the fit for extracting three structure functions.

As a first step, P_{LT}^\perp , P_{TT}^\perp and $P_{TT}^{\perp'}$ are fitted to the data, considering $P_{LT}^{\perp'} = 0$. The results are collected in table 8.10. Different starting points of the fitting routine are used for better investigating convergence issues or the possibility of trapping in local minima.

As can be seen also in this case stable results are not reached.

8.11 Extraction of the Structure Function P_{LT}^\perp

It is difficult with the actual dataset to extract more structure functions, then we choose to fit the most relevant one, which is P_{LT}^\perp . The P_x^{CM} polarization component is rather sensitive to this structure function, while P_y^{CM} has a smaller sensitivity and only for out-of-plane events.

In this case only one variable is fitted to the data, so it is easy to directly check the shape of the likelihood as a function of it. In Fig. 8.13 the negative logarithm of the likelihood is shown as a function of the fitting parameter, which multiplies P_{LT}^\perp as obtained from the chiral perturbation theory model [22].

As it is visible, only one minimum for the likelihood exists at a scale parameter of 1.285, which means that the measurement gives a P_{LT}^\perp 1.285 times larger than the prediction of HB χ PT at $O(p^3)$ in the case of the Mergell et al. form factor parameterization. The fit is repeated for the Friedrich-Walcher parameterization giving comparable results.

In the extraction procedure, in order to extract a structure function free from model dependencies, P_z^{CM} is fixed to the BH+B calculation, while all the other structure functions are set to zero.

For the function ΔM_0 , the values obtained by the iterated fit [73] of the cross section are used.

The obtained results are the following, for the two different form factor parameterizations

Form Factors	P_{LT}^\perp (GeV $^{-2}$)
Mergell et al.	-13.7 \pm 2.8
Friedrich-Walcher	-13.8 \pm 4.0

8.12 Systematical Errors

For the determination of the systematical error on P_{LT}^\perp various effects should be taken into account. Some effects are of experimental origin, while others come from

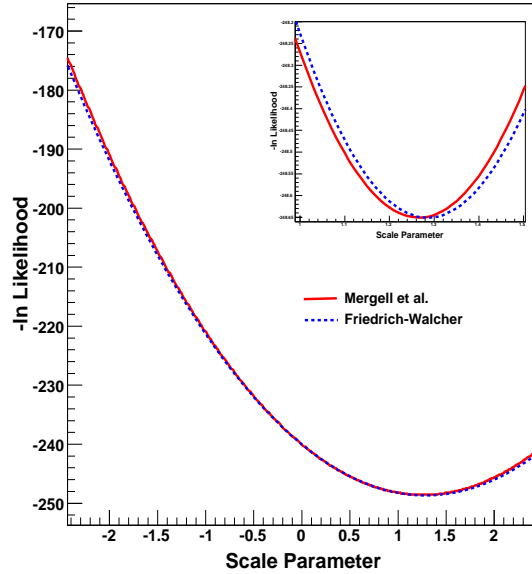


Figure 8.13: Negative logarithm of the likelihood function. Only one minimum is visible as a function of the parameter which is optimized to the experimental data.

the extraction technique and the approximations done.

- The denominator of the theoretical double polarization asymmetry in the LEX approach is fixed by the result of the unpolarized analysis. The sensitivity to this external constraint is investigated using two different values for ΔM_0 : the extracted and the iterated one.
- The polarization component P_z^{CM} is fixed to the BH+B theoretical value. The extraction is also done for P_z^{CM} fixed to the HB χ PT prediction.
- The beam polarization has a direct influence on the double polarization observable and a variation of $\pm 2\%$ of it is used for estimating its systematic influence.
- The sensitivity to the other structure functions is very low and in principle they can be set to zero for simplifying the fitting procedure. This systematic effect is investigated fitting P_{LT}^\perp with the other structure functions set to zero or to the HB χ PT calculated values.

As systematic error, the maximum range of variation among the single contributions is taken and all the studies were done with the Mergell et al. form factors.

The results for P_{LT}^\perp in the different fitting conditions are reported in table 8.11.

8.13 Separation of P_{LL} and P_{TT}

The extracted structure function P_{LT}^\perp depends on P_{LL} and P_{TT} :

$$P_{LT}^\perp = \frac{RG_E}{2G_M} P_{TT}(q) - \frac{G_M}{2RG_E} P_{LL}(q), \quad (8.14)$$

Systematics	P_{LT}^\perp (GeV ⁻²)
$P_z^{CM} = HB\chi PT$	-14.2 ± 2.9
$P_{TT}^\perp, P_{TT}'^\perp, P_{LT}^\perp = HB\chi PT$	-15.1 ± 3.1
$P_{beam} + 2\%$	-14.2 ± 2.9
$P_{beam} - 2\%$	-13.0 ± 2.6
M_0 no iter.	-13.4 ± 2.7

Table 8.11: Extraction of P_{LT}^\perp in different conditions for estimating the systematic uncertainty.

where the kinematical coefficient R was defined in Chapt. 3, G_E and G_M are the nucleon form factors and are dependent on \tilde{Q}^2 .

From the cross section analysis the combination

$$S_1 = P_{LL} - P_{TT}/\epsilon, \quad (8.15)$$

was also extracted, so the two experimental results of Eq. 8.14 and 8.15 can be combined for separating P_{LL} and P_{TT} .

A possible expression for P_{LL} is

$$P_{LL} = \left[P_{LT}^\perp + \frac{\epsilon R G_E}{2G_M} S_1 \right] / \left[\frac{\epsilon R G_E}{2G_M} - \frac{G_M}{2R G_E} \right], \quad (8.16)$$

and P_{TT} can be then obtained from 8.15. The results are

$$\begin{aligned} P_{LL} &= 52.3 \pm 21.6 \pm 81.4 \\ P_{TT} &= 13.8 \pm 10.6 \pm 56.0 \end{aligned} \quad (8.17)$$

The errors are very large and this is caused by the kinematical coefficients which do not permit a clean separation because the lines defined by Eq. 8.14 and 8.15 are nearly parallel.

8.14 Summary

The recoil proton polarization is measured after scattering with a polarized electron beam. A maximum likelihood method was developed for fitting the recoil polarization. The fit uses as constraint P_z^{CM} which is fixed to the BH+B theoretical value for each event.

A new determination of the carbon analyzing power, based on elastic $\vec{e}p$ scattering, extending the existing parameterizations was also performed: the measurement permits to gain more statistics, which is strongly limited by the polarimeter efficiency ($\sim 2\%$).

The available dataset permits the extraction of a new structure function using the LEX approach. The extraction was achieved extending the maximum likelihood method used for the recoil proton polarization fit.

The various systematic effects due to the hypotheses underlying the fit were considered: the use of the BH+B or HB χ PT predictions as constraint to P_z^{CM} , the effect

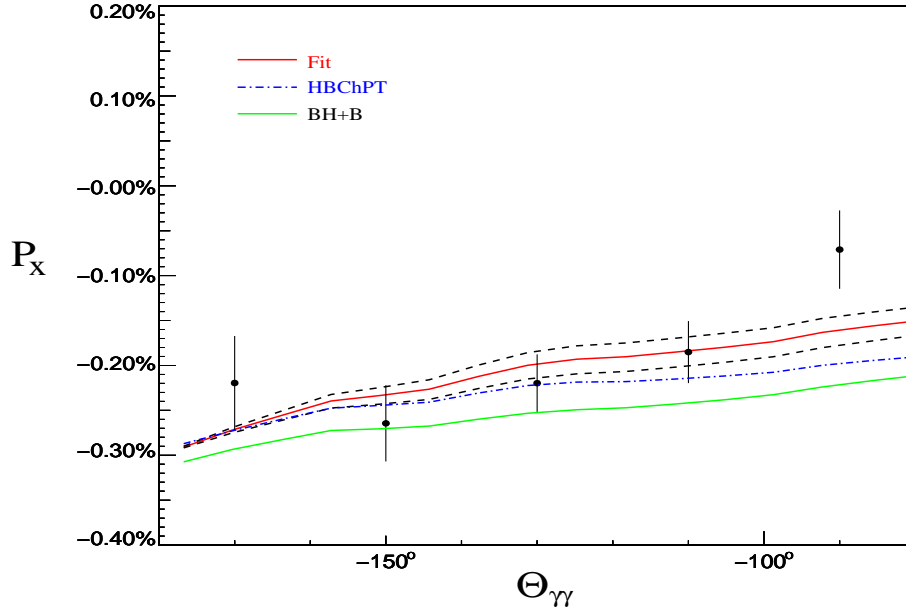


Figure 8.14: Polarization component P_x^{CM} with the fitted value of P_{LT}^\perp : the solid red line is the obtained result, the dashed black lines indicate the statistical error. As reference, the $\text{HB}\chi\text{PT}$ (dash-dotted blue line) and the BH+B (solid green line) results are shown.

of the beam polarization and of the iteration procedure in determining the structure functions from the unpolarized cross section.

The final result for the two different form factor parameterizations used is

Form Factors	P_{LT}^\perp (GeV^{-2})
Mergell et al.	$-13.7 \pm 2.3 \pm 2.1$
Friedrich-Walcher	$-13.8 \pm 4.0 \pm 2.1$

In Fig. 8.14 the effect of the fitted structure function is shown on the P_x^{CM} component together with the BH+B and $\text{HB}\chi\text{PT}$ result in the case of the Mergell et al. form factor parameterization.

Chapter 9

Conclusions

The first double polarization virtual Compton scattering experiment under the pion threshold was performed at MAMI at $Q^2 = 0.33 \text{ (GeV/c)}^2$. The cross section and the recoil proton polarizations using a highly polarized electron beam were measured. The scattered proton and electron were detected in coincidence by two high resolution magnetic spectrometers. In the proton arm a focal plane proton polarimeter was installed. This consists of a carbon layer as a secondary scatterer and a package of horizontal drift chambers for proton tracking.

The VCS reaction was measured at $q = 600 \text{ MeV/c}$ and $\epsilon = 0.645$ with an outgoing photon momentum $q' = 90 \text{ MeV/c}$. Using the ansatz of a low energy expansion, two structure functions were extracted by use of a linear separation: $P_{LL} - P_{TT}/\epsilon$ and P_{LT} . The values obtained are in agreement with the results of [6] and in [73] an iteration procedure was developed for further improvement and consistency. The results are in good agreement with the HB χ PT calculations at $O(p^3)$ of [22].

In this experiment, the structure function P_{LT}^\perp was also extracted for the first time through a double polarization measurement.

A maximum likelihood algorithm was developed together with a simulation for carefully investigating the whole fitting procedure. Correction factors for the spin precession in the magnetic fields of the spectrometer and for the false asymmetries were determined and used in the polarization reconstruction.

The algorithm was then extended to directly fit the generalized polarizabilities or the structure functions to the data. The P_z^{CM} component was not determined to high enough precision so it was fixed to the theoretical BH+B value. This approximation was proven to have a negligible effect and in fact P_x^{CM} , which mainly contributes to P_{LT}^\perp , is practically uncorrelated with P_z^{CM} .

For the structure function P_{LT}^\perp a lower result than the HB χ PT prediction is found. This structure function contains the same generalized polarizabilities as $P_{LL} - P_{TT}/\epsilon$ and P_{LT} , but the particular kinematics used does not permit the clear separation of the single contributions of the GPs. The extraction of more combinations or the direct extraction of the GPs requires a better measurement of the P_z^{CM} polarization component and a wider kinematical range. Future kinematical arrangements should also be chosen in order to maximize the polarimeter tracking accuracy, which is higher for highly energetic protons.

The two analyses were performed with two different form factor parameterizations. The structure functions $P_{LL} - P_{TT}/\epsilon$ and P_{LT}^\perp were found to be rather insensitive to the form factors, whilst P_{LT} was more sensitive.

In the following table the final results for the two different form factor parameterizations are shown.

	Mergell et al (GeV ⁻²)	Friedrich-Walcher (GeV ⁻²)	HB χ PT Mergell / FW (GeV ⁻²)
$P_{LL} - P_{TT}/\epsilon$	$25.6 \pm 2.9 \pm 2.8$	$25.3 \pm 2.9 \pm 2.8$	26.3 / 26.0
P_{LT}	$-5.0 \pm 1.1 \pm 2.1$	$-7.5 \pm 1.1 \pm 2.1$	-5.5 / -5.4
P_{LT}^\perp	$-13.7 \pm 2.8 \pm 2.2$	$-13.8 \pm 4.0 \pm 2.2$	-10.7 / -10.6

The results for the different parameterizations of the form factors agree within error bars. It was not possible to use the obtained results to further separate the P_{LL} and P_{TT} contributions due to the error bars and the characteristics of the kinematical coefficients.

In the future, more experimental effort is needed in order to separate more structure functions or polarizabilities, for example by enlarging the actual dataset or attempting a measurement with new kinematics with different virtual photon polarization ϵ . The separation of P_{TT} is very interesting, because it depends only on spin GPs and this will be useful for testing theoretical models, in particular the dispersion relation model. It would also be interesting to analyze the double polarization data without making use of the low energy expansion, but instead using dispersion relations. This would take all orders in q' into account, as it has already been done for the unpolarized data.

Appendix A

Nucleon Form Factors

The elastic electron scattering on spin $\frac{1}{2}$ particles with extended structure and anomalous magnetic moment can be described by the following Rosenbluth cross section [62] :

$$\frac{d\sigma}{d\Omega} = \left(\frac{d\sigma}{d\Omega} \right)_{Mott} \cdot \left\{ F_1^2(Q^2) + \frac{Q^2}{4M^2} \left[F_2^2(Q^2) + 2(F_1^2(Q^2) + F_2^2(Q^2)) \tan^2 \frac{\theta}{2} \right] \right\} \quad (\text{A.1})$$

where $\left(\frac{d\sigma}{d\Omega} \right)_{Mott}$ is the Mott cross section for pointlike particles without magnetic moment. In Eq. A.1 the Dirac form factor F_1 and the Pauli form factor F_2 are introduced in order to parameterize the a priori unknown hadronic current of the nucleon. More often the Sachs form factors are used:

$$G_E(Q^2) = F_1(Q^2) - \frac{Q^2}{4M^2} F_2(Q^2) \quad (\text{A.2})$$

$$G_M(Q^2) = F_1(Q^2) + F_2(Q^2) \quad (\text{A.3})$$

They are called respectively electric and magnetic form factors.

The knowledge of the form factors is fundamental for describing electromagnetic interactions on the nucleon. Many parameterizations of the form factors are available and in the following two of them, relevant in the low energy range, are discussed. The dipole parameterization is also briefly summarized.

Dipole Parameterization

The simplest parameterization which is able to describe the gross properties of the form factors is the so called ‘‘Dipole’’ parameterization

$$G_E^p = \frac{1}{(1 + q^2/M_d)^2} \quad (\text{A.4})$$

$$G_M^p = \frac{\mu_N}{(1 + q^2/M_d)^2} \quad (\text{A.5})$$

where μ_N is the anomalous magnetic moment of the proton. The parameterization depends only from one parameter, the ‘‘dipole mass’’ $M_d = 0.71\text{GeV}/c^2$ which is the same for the two form factors and this is a remarkable property of this model.

$a_{10}^E = 1.041$	$a_{10}^M = 1.002$
$a_{11}^E = 0.765$	$a_{11}^M = 0.749$
$a_{20}^E = -0.041$	$a_{20}^M = -0.002$
$a_{21}^E = 6.2$	$a_{21}^M = 6.0$
$a_b^E = -0.23$	$a_b^M = -0.13$
$Q_b^E = 0.07$	$Q_b^M = 0.35$
$\sigma_b^E = 0.27$	$\sigma_b^M = 0.21$

Table A.1: Constants resulting from the FW phenomenological parameterization fit

Friedrich-Walcher Parameterization

Precise measurements of the electric form factor of the neutron are very difficult because this particle presents globally no electric charge. Nowadays, with enough available data, the Q^2 dependence of this quantity is better known and it seems to present a “bump” in the region of $Q^2 = 0.3 \text{ GeV}/c^2$. This qualitative observation is taken as motivation in [72] for a new parameterization of the nucleon form factors which is made superimposing to a smooth part constructed as a sum of two dipoles (for maintaining more flexibility):

$$G_s^E(q^2) = \frac{a_{10}^E}{(1 + Q^2/a_{11}^E)^2} + \frac{a_{20}^E}{(1 + Q^2/a_{21}^E)^2} \quad (\text{A.6})$$

$$G_s^M(q^2) = \frac{a_{10}^M}{(1 + Q^2/a_{11}^M)^2} + \frac{a_{20}^M}{(1 + Q^2/a_{21}^M)^2} \quad (\text{A.7})$$

a new term accounting for the presence of the “bump”:

$$G_b^E(q^2) = e^{-\frac{1}{2}\left(\frac{Q^2 - Q_b^E}{\sigma_b^E}\right)^2} + e^{-\frac{1}{2}\left(\frac{Q^2 + Q_b^E}{\sigma_b^E}\right)^2} \quad (\text{A.8})$$

$$G_b^M(q^2) = e^{-\frac{1}{2}\left(\frac{Q^2 - Q_b^M}{\sigma_b^M}\right)^2} + e^{-\frac{1}{2}\left(\frac{Q^2 + Q_b^M}{\sigma_b^M}\right)^2} \quad (\text{A.9})$$

and expressing then the form factors as:

$$G_E(q^2) = G_s^E(q^2) - a_b^E q^2 G_b^E(q^2) \quad (\text{A.10})$$

$$G_M(q^2) = \mu(G_s^M(q^2) - a_b^M q^2 G_b^M(q^2)) \quad (\text{A.11})$$

with $\mu = 2.79284739$

This parameterization is fitted to the available world data on form factor measurements, yielding for the constants the values reported in table A.1.

Mergell et al. Parameterization

This parameterization [64] is obtained with the aid of a dispersion relation analysis using the 1995 world data set. The analysis is constrained using unitarity and the

results from perturbative QCD for the high- Q^2 region. The explicit result of the fit is given by the following formulae

$$F_1(Q^2) = F_1^s(Q^2) + F_1^v(Q^2) \quad (\text{A.12})$$

$$F_2(Q^2) = F_2^s(Q^2) + F_2^v(Q^2) \quad (\text{A.13})$$

$$\begin{aligned}
F_1^s(Q^2) &= \left[\frac{9.464}{0.611 + Q^2} - \frac{9.054}{1.039 + Q^2} - \frac{0.410}{2.56 + Q^2} \right] \left[\ln \left(\frac{9.733 + Q^2}{0.35} \right) \right]^{-2.148} \\
F_2^s(Q^2) &= \left[-\frac{1.549}{0.611 + Q^2} + \frac{1.985}{1.039 + Q^2} - \frac{0.436}{2.56 + Q^2} \right] \left[\ln \left(\frac{9.733 + Q^2}{0.35} \right) \right]^{-2.148} \\
F_1^v(Q^2) &= \frac{\left[1.032(\ln 26.38)^{2.148} + 0.088(\ln 26.6657)^{2.148}(1 + Q^2/0.318)^{-2} \right]}{2(1 + Q^2/0.55)} \\
&\quad - \frac{38.885}{2.103 + Q^2} + \frac{425.007}{2.743 + Q^2} - \frac{389.742}{2.835 + Q^2} \left[\ln \frac{9.733 + Q^2}{0.35} \right]^{-2.148} \\
F_2^v(Q^2) &= \frac{\left[5.782(\ln 26.38)^{2.148} + 0.391(\ln 26.6657)^{2.148}(1 + Q^2/0.142)^{-1} \right]}{2(1 + Q^2/0.536)} \\
&\quad - \frac{73.535}{2.103 + Q^2} + \frac{83.211}{2.743 + Q^2} - \frac{29.467}{2.835 + Q^2} \left[\ln \frac{9.733 + Q^2}{0.35} \right]^{-2.148}
\end{aligned}$$

A.1 Bethe-Heitler + Born Cross Section and Form Factors Dependence

In order to estimate the systematic effect of a different form factor parameterization, the cross section of the BH+Born process is calculated using different form factors. In Fig. A.1 the three discussed parameterizations are used in the calculation of the BH+B cross section, which is the known part of the photon electroproduction reaction. The Friedrich-Walcher parameterization gives a considerably lower cross section. In Fig. A.2, the evolution as a function of Q^2 of the form factors is shown: the Mergell et al. and Friedrich-Walcher form factors are normalized by the dipole parameterization for better appreciating the differences. While at the $Q^2 = 0.33(\text{GeV}/c)^2$, which is the kinematical point of the present experiment, the electric form factors are similar, the magnetic one is different in absolute value.

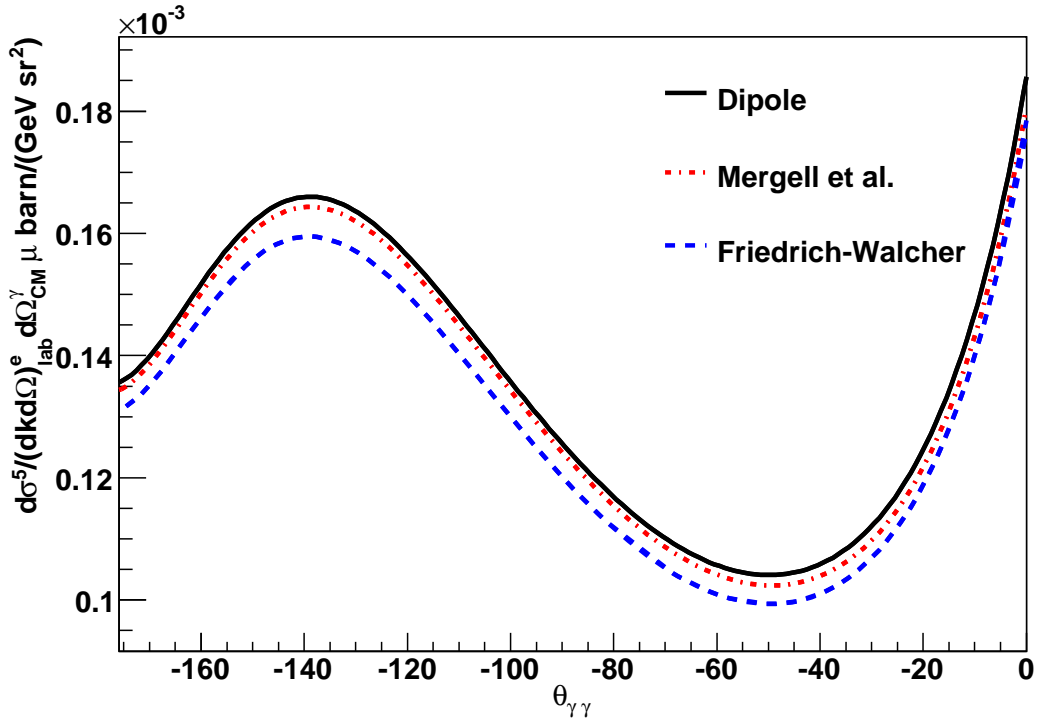


Figure A.1: Effect of different form factor parameterizations on the BH+Born cross section. Solid line (black) Dipole parameterization; Dashed Line (blue) Friedrich-Walcher parameterization; Dash-dotted (red): Mergell et al. parameterization.

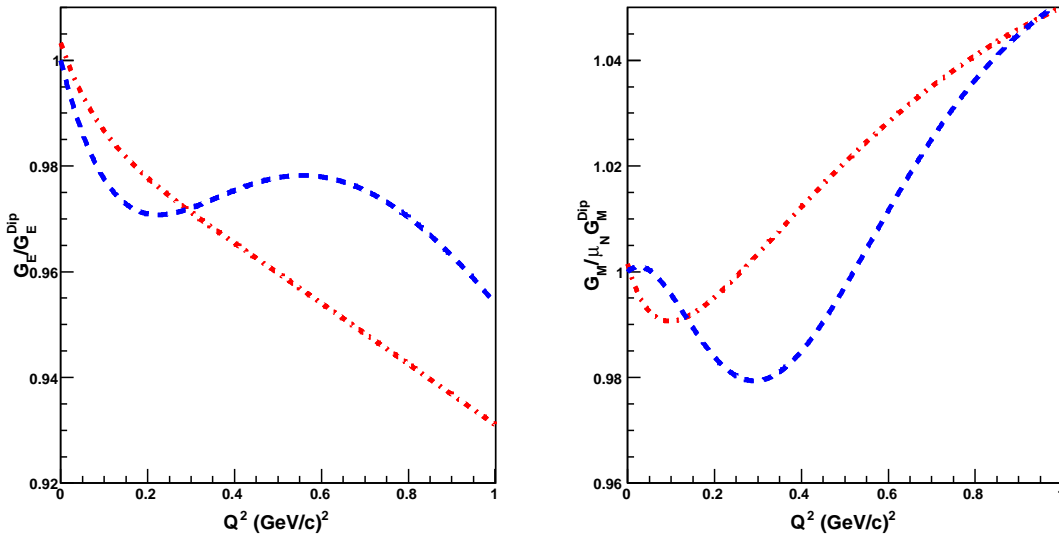


Figure A.2: Electric and magnetic form factors of the proton in 2 different parameterizations and normalized to the Dipole one. Dashed Line (blue) Friedrich-Walcher parameterization; Dash-dotted (red): Mergell et al. parameterization.

Appendix B

Maximum Likelihood Method

The maximum likelihood method belongs to the class of statistical inference methods and it is widely used in many science applications, because of a number of good properties which will be summarized in this appendix.

B.1 Definition of the Method

Let consider a probability distribution characterized by r parameters $\bar{\theta} = \{\theta_1, \theta_2, \dots, \theta_r\}$ and let call a series of N observations $\bar{x} = \{x_1, x_2, \dots, x_N\}$, then one can define the *a posteriori* probability distribution $p(\bar{x}|\bar{\theta})$. The probability density $p_i(x|\bar{\theta})$ is the probability that the i -th event is observed with a value x , *given* a value for the set of parameters $\bar{\theta}$. Supposing that the measurements are independent and each event is distributed according to p , the so called *likelihood function* can be constructed:

$$\mathcal{L} = \prod_i^N p_i(\bar{x}|\bar{\theta}). \quad (\text{B.1})$$

A useful definition which simplifies both analytical and numerical computations is that of the *log-likelihood function*:

$$l(\bar{x}|\bar{\theta}) = \ln \mathcal{L}(\bar{x}|\bar{\theta}) = \sum_i^N \ln p_i(\bar{x}|\bar{\theta}). \quad (\text{B.2})$$

Being the logarithm a monotonic function, the stationary points of the likelihood are the same also in the log-likelihood function.

The *maximum likelihood principle* states that an estimate $\hat{\bar{\theta}}$ of the parameters $\bar{\theta}$ is obtained solving the maximum likelihood equations:

$$\frac{\partial l(\bar{x}|\bar{\theta})}{\partial \bar{\theta}} = 0 \quad \Rightarrow \quad \hat{\bar{\theta}}. \quad (\text{B.3})$$

In particular the stationary points found with the above equations should be maxima, so:

$$\frac{\partial^2 l(\bar{x}|\bar{\theta})}{\partial \bar{\theta}^2} < 0. \quad (\text{B.4})$$

In this way a method for calculating the estimates of parameters of a certain probability distribution, given some measurements \bar{x} is provided. Of course, the distribution followed by the measurements should be known in advance or guessed in some way. The values of the estimates alone are not sufficient: what is needed are also the statistical errors and their properties for understanding how trustable they are as estimators of unknown quantities extracted from a finite sample.

B.2 Properties of the Estimators

Uniqueness

The estimators of the maximum likelihood method are unique. If we choose a function of them $f = f(\bar{\theta})$ and apply the likelihood equations for f we get

$$\frac{\partial l(\bar{x}|\bar{\theta})}{\partial f} = \frac{\partial l(\bar{x}|\bar{\theta})}{\partial \bar{\theta}} \frac{\partial \bar{\theta}}{\partial f} = 0, \quad (\text{B.5})$$

but the last equation is always satisfied because of B.3.

Efficiency

A desirable property for an estimator is *efficiency*. An estimator θ is said to be efficient if its variance $Var[\theta]$ is the smallest possible.

In order to discuss this property, we introduce a quantity called *Fisher information matrix* I of the estimators $\bar{\theta}$:

$$I(\bar{\theta}) = E \left[\left\{ \frac{\partial}{\partial \bar{\theta}} \ln p_i(\bar{x}|\bar{\theta}) \right\}^2 \right], \quad (\text{B.6})$$

where with $E[\]$ the expectation value of the quantity in parentheses is intended.

If $\hat{\theta}$ is an *unbiased* estimator of $\bar{\theta}$, then the following inequality holds

$$Var[\hat{\theta}] \geq \frac{1}{I(\bar{\theta})}, \quad (\text{B.7})$$

and it is known as the *Cramer-Rao-Frechet* inequality, which sets a limit for the efficiency of an unbiased estimator.

Furthermore, as demonstrated e.g. in [74] $\hat{\theta}$ is a minimum variance unbiased estimator if

$$\frac{\partial \ln p_i}{\partial \theta} = I(\theta)(\hat{\theta} - \theta) \quad (\text{B.8})$$

Evidently an estimator has minimum variance if $Var[\hat{\theta}] = \frac{1}{I(\theta)}$ which is the case of the maximum likelihood estimators in the limit of a large number of observations as shown in the next section.

B.3 Asymptotic Properties

Assuming the existence of the derivatives of the likelihood, it can be expanded in powers around the maximum (where the first derivative vanishes)

$$\ln \mathcal{L} = \ln \mathcal{L}(\hat{\theta}) + \underbrace{\frac{\partial \ln \mathcal{L}}{\partial \theta}}_{=0}(\hat{\theta})(\hat{\theta} - \theta) + \frac{\partial^2 \ln \mathcal{L}}{\partial \theta_i \partial \theta_j}(\hat{\theta})(\hat{\theta} - \theta)^2 + \dots = \frac{\partial^2 \ln \mathcal{L}}{\partial \theta_i \partial \theta_j}(\hat{\theta})(\hat{\theta} - \theta)^2 + \dots \quad (\text{B.9})$$

If we consider now the expectation value of the likelihood second derivative and using the useful relation

$$I(\theta) = E \left[\left\{ \frac{\partial}{\partial \theta} \ln p(x|\theta) \right\}^2 \right] = -E \left[\frac{\partial^2}{\partial \theta^2} \ln p(x|\theta) \right], \quad (\text{B.10})$$

under the hypothesis of a large sample we can substitute the expectation value with the sample mean

$$E \left[\frac{\partial^2 \ln \mathcal{L}}{\partial \theta_i \partial \theta_j} \right] \approx \frac{1}{N} \sum_{i=1}^N \frac{\partial^2 \ln \mathcal{L}}{\partial \theta_i \partial \theta_j}, \quad (\text{B.11})$$

finding after substitution

$$\frac{\partial^2 \ln \mathcal{L}}{\partial \theta_i \partial \theta_j} \approx -NI(\theta) = -I_N(\theta). \quad (\text{B.12})$$

If we compare the obtained result with Eq. B.8 and Eq. B.9, this proves that in the large sample limit, the maximum likelihood estimator has minimum variance, it is unbiased and consistent. The method has then many advantages:

- The maximum likelihood estimator is asymptotically efficient (and also normal [74]).
- The histogramation of the dataset is avoided: all the data are used without a decision about the binning.
- All the available data are used and this is especially good in experiments with poor statistics.
- Easy to implement for parameters which are implicitly represented by functions.
- The method is analogous of the least squares fitting in the case where p_i is a gaussian distribution.

B.4 Covariance Matrix

The maximum likelihood is asymptotically normal as the number of samples increases. Comparing Eq. B.9 with the second derivative of a multivariate gaussian distribution, we find

$$\sigma_{ij}^2 = \left(\frac{\partial^2 \mathcal{L}}{\partial \theta_i \partial \theta_j} \right)^{-1} = I(\bar{\theta})^{-1}. \quad (\text{B.13})$$

The covariance matrix results equal to the inverse of the Fisher information matrix. The square roots of the matrix diagonal entries correspond to the mean square roots of the estimators.

Appendix C

Kinematics

C.1 Kinematical Coefficients for the Unpolarized Cross Section

$$\mathcal{M}_0 - \mathcal{M}^{BH+Born} = v_{LL} \left[P_{LL}(q) - \frac{1}{\epsilon} P_{TT} \right] + v_{LT} P_{LT}(q), \quad (\text{C.1})$$

$$v_{LL} = \epsilon K \sin \theta_{\gamma\gamma} (\omega'' \sin \theta_{\gamma\gamma} - \omega' k_T \cos \varphi \cos \theta_{\gamma\gamma}) \quad (\text{C.2})$$

$$v_{LT} = -\epsilon K \sqrt{2\epsilon(1+\epsilon)} ((\omega'' \sin \theta_{\gamma\gamma} \cos \varphi - \omega' k_T \cos \theta_{\gamma\gamma}) + \frac{\tilde{q}_0}{q} (\omega'' \sin \theta_{\gamma\gamma} \cos \theta_{\gamma\gamma} \cos \varphi - \omega' k_T (1 - \cos^2 \varphi \sin^2 \theta_{\gamma\gamma}))), \quad (\text{C.3})$$

with

$$K = \frac{4M e^6 q}{\tilde{Q}^2 (1 - \epsilon)} \sqrt{\frac{2\sqrt{q^2 + m^2}}{\sqrt{q^2 + m^2} + M}},$$

$$\tilde{Q} = [Q]_{q'=0} ; \quad \tilde{q}_0 = -\frac{\tilde{Q}_0}{2M} = M - \sqrt{M^2 + q^2},$$

$$\omega = \left[-q' \left(\frac{1}{pq'} + \frac{1}{kq'} \right) \right]_{q'=0} ; \quad \omega' = \left[q' \left(\frac{1}{k'q'} - \frac{1}{kq'} \right) \right]_{q'=0} ; \quad \omega'' = \omega q - \omega' \sqrt{\tilde{k}'^2 - k_T^2}$$

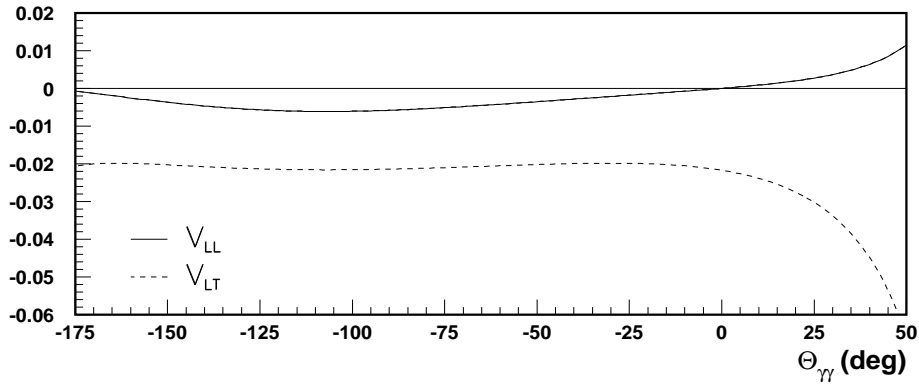


Figure C.1: Unpolarized VCS kinematical coefficients for the MAMI kinematics: $q=600$ MeV, $\epsilon=0.62$, $\varphi=0$.

C.2 Kinematical Coefficients for the Double Polarization Observable

$$R = 2M/\tilde{Q} \quad (\text{C.4})$$

$$\tilde{q}_0 = M - \sqrt{M^2 + q^2} \ ; \ \tilde{Q} = -2M\tilde{q}_0 \quad (\text{C.5})$$

$$\tilde{k}' = \sqrt{\tilde{k}'_0{}^2 - m_e^2}, \quad (\text{C.6})$$

where quantities with a *tilde* are calculated in the limit $q' \rightarrow 0$ and the nucleon form factors G_E and G_M are functions of \tilde{Q}^2 .

The angular dependent coefficients (also plotted in Fig. C.2, C.3, C.4) are:

$$\begin{aligned} v_1 &= \sin\theta(\omega'' \sin\theta - k_T\omega' \cos\theta \cos\phi) \\ v_2 &= -(\omega'' \sin\theta \cos\phi - k_T\omega' \cos\theta) \\ v_3 &= -(\omega'' \sin\theta \cos\theta \cos\phi - k_T\omega'(1 - \sin^2\theta \cos^2\phi)), \end{aligned}$$

$$\begin{aligned} v_1^x &= \sin\theta \cos\phi(\omega'' \sin\theta - k_T\omega' \cos\theta \cos\phi) \\ v_2^x &= -\omega'' \sin\theta - k_T\omega' \cos\theta \cos\phi \\ v_3^x &= -\cos\theta(\omega'' \sin\theta - k_T\omega' \cos\theta \cos\phi) \\ v_4^x &= k_T\omega' \sin\theta \sin^2\phi, \end{aligned}$$

$$\begin{aligned} v_1^y &= \sin\theta \sin\phi(\omega'' \sin\theta - k_T\omega' \cos\theta \cos\phi) \\ v_2^y &= k_T\omega' \cos\theta \sin\phi \\ v_3^y &= k_T\omega' \sin\phi \\ v_4^y &= -k_T\omega' \sin\theta \sin\phi \cos\phi. \end{aligned}$$

C.3 Lorentz Transformations

The Lorentz boost connecting the laboratory and the center of mass frame is defined by

$$\vec{\beta} = \frac{\vec{q}_{lab}}{\nu_{lab} + M} \quad \text{and} \quad \gamma = \frac{\nu_{lab} + M}{\sqrt{s}}. \quad (\text{C.7})$$

In this way, one can calculate the proton energy in the laboratory frame ¹

$$p_{lab}^{\prime 0} = \gamma p^{\prime 0} + \gamma\beta p'_z = \frac{(\nu_{lab} + M)(s + M^2) - q_{lab}(s + M^2)\cos\theta_{\gamma\gamma}}{2s}, \quad (\text{C.8})$$

where the new variable $\theta_{\gamma\gamma}$, the angle between the virtual and the real photon has been introduced. By measuring the proton four-vector in the laboratory frame, it is also possible to know $\theta_{\gamma\gamma}$.

¹ p'_z is the projection along the virtual photon direction of the recoil proton momentum.

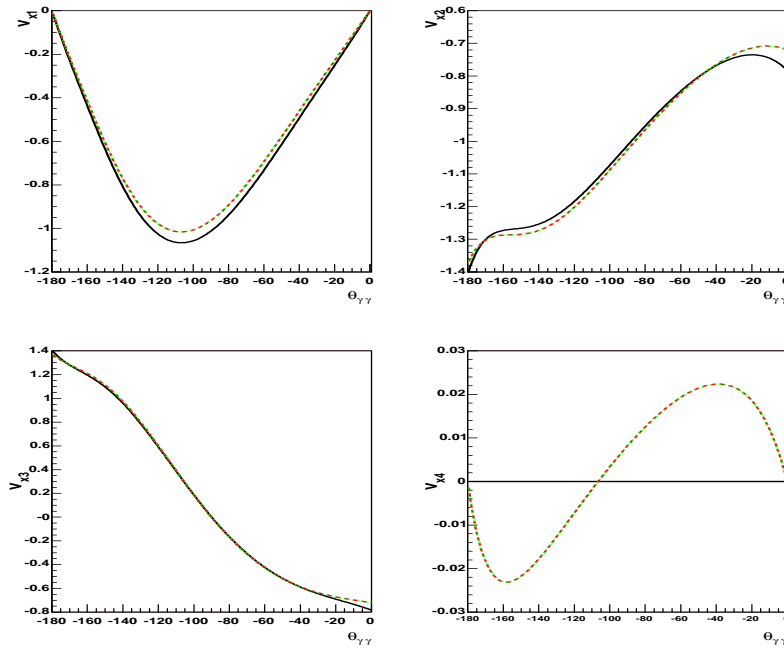


Figure C.2: Angular evolution of the kinematical coefficients for $M(h,x)$. Solid black line: $\varphi = 0$; dashed lines (red and green): $\varphi = \pm 20^\circ$. The out-of-plane behavior doesn't depend on the sign of φ .

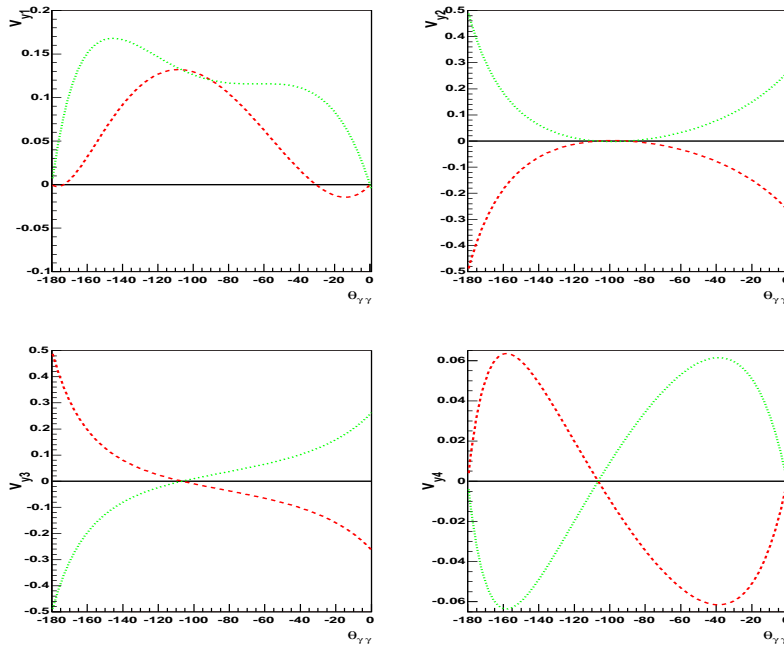


Figure C.3: Angular evolution of the kinematical coefficients for $M(h,y)$. Solid black line: $\varphi = 0$. Dashed line (red): $\varphi = 20^\circ$. Dotted line (green): $\varphi = -20^\circ$. Note, that in an in-plane kinematics this coefficients will vanish, giving $M(h,y)=0$.

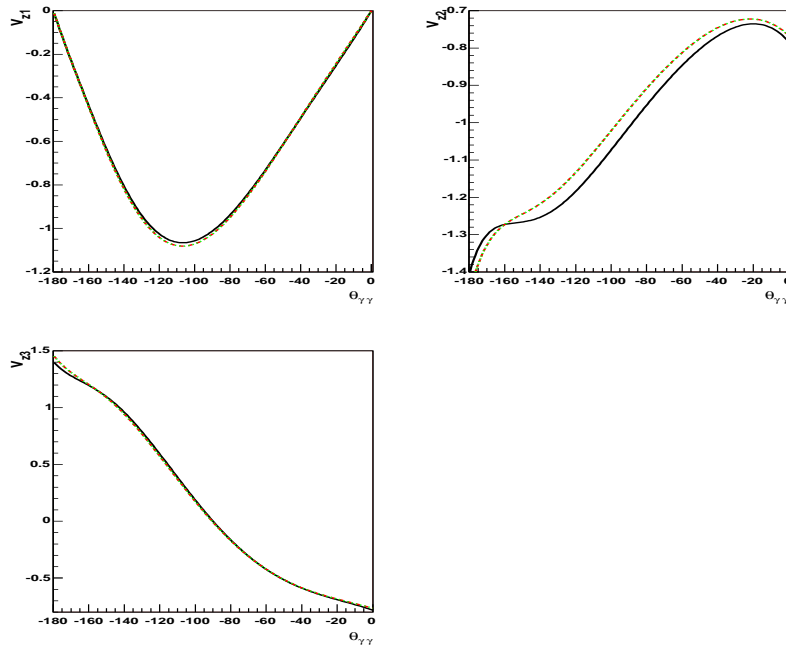


Figure C.4: Angular evolution of the kinematical coefficients for $M(h,z)$. Solid black line: $\varphi = 0^\circ$; dashed lines (red and green): $\varphi = \pm 20^\circ$. The out-of-plane behavior doesn't depend on the sign of φ .

Appendix D

Tables

D.1 Cross Section Data

$\theta_{\gamma\gamma}$	$d\sigma_{exp}^5$ (pb/MeV sr ²)	$\theta_{\gamma\gamma}$	$d\sigma_{exp}^5$ (pb/MeV sr ²)
-131°	0.148 ± 0.002	-95°	0.120 ± 0.002
-122°	0.142 ± 0.002	-86°	0.114 ± 0.002
-113°	0.134 ± 0.002	-77°	0.108 ± 0.002
-104°	0.128 ± 0.002	-68°	0.119 ± 0.002

Table D.1: Cross section data for the April 05 beamtime

$\theta_{\gamma\gamma}$	$d\sigma_{exp}^5$ (pb/MeV sr ²)	$\theta_{\gamma\gamma}$	$d\sigma_{exp}^5$ (pb/MeV sr ²)
-131°	0.149 ± 0.002	-95°	0.118 ± 0.001
-122°	0.140 ± 0.001	-86°	0.110 ± 0.001
-113°	0.135 ± 0.001	-77°	0.106 ± 0.001
-104°	0.126 ± 0.001	-68°	0.109 ± 0.001

Table D.2: Cross section data for the July 05 beamtime

$\theta_{\gamma\gamma}$	$d\sigma_{exp}^5$ (pb/MeV sr ²)	$\theta_{\gamma\gamma}$	$d\sigma_{exp}^5$ (pb/MeV sr ²)
-168.5°	0.150 ± 0.004	-128.5°	0.150 ± 0.003
-160.5°	0.149 ± 0.003	-120.5°	0.138 ± 0.003
-152.5°	0.156 ± 0.003	-112.5°	0.136 ± 0.003
-144.5°	0.152 ± 0.003	-104.5°	0.129 ± 0.003
-136.5°	0.150 ± 0.003	-96.5°	0.122 ± 0.004

Table D.3: Cross section data for the November 05 beamtime

D.2 Rosenbluth Separation Data

Form Factors	Mergell et al.		Friedrich-Walcher	
$\theta_{\gamma\gamma}$	v_{LL}/v_{LT}	$\Delta M_0/v_{LT}$ (GeV ²)	v_{LL}/v_{LT}	$\Delta M_0/v_{LT}$ (GeV ²)
-168°	0.129	-4.698 ± 2.689	0.129	-6.922 ± 2.690
-163°	0.180	0.938 ± 2.407	0.180	-1.464 ± 2.407
-158°	0.228	0.713 ± 2.429	0.228	-1.840 ± 2.429
-153°	0.272	-1.656 ± 2.571	0.272	-4.340 ± 2.571
-148°	0.312	7.269 ± 2.280	0.312	4.511 ± 2.280
-143°	0.348	6.131 ± 2.360	0.348	3.323 ± 2.360
-138°	0.379	9.390 ± 2.234	0.379	6.563 ± 2.234
-133°	0.405	2.336 ± 2.461	0.405	-0.484 ± 2.461
-128°	0.426	9.361 ± 2.149	0.426	6.571 ± 2.149
-123°	0.442	7.963 ± 2.249	0.442	5.220 ± 2.249
-118°	0.453	9.931 ± 2.160	0.453	7.247 ± 2.160
-113°	0.460	5.465 ± 2.369	0.460	2.848 ± 2.369
-108°	0.463	8.314 ± 2.311	0.463	5.770 ± 2.311
-103°	0.462	4.565 ± 2.547	0.462	2.096 ± 2.547
-98°	0.457	2.918 ± 2.688	0.457	0.524 ± 2.688
-93°	0.449	6.681 ± 2.562	0.449	4.362 ± 2.562
-88°	0.438	2.904 ± 2.798	0.438	0.657 ± 2.798
-83°	0.425	-2.672 ± 3.062	0.425	-4.85 ± 3.062
-78°	0.409	-0.201 ± 3.268	0.408	-2.315 ± 3.268

Table D.4: Data used for the Rosenbluth separation for the two form factor parameterizations: Mergell et al. [64] and Friedrich-Walcher [72].

List of Figures

2.1	Experimental results for the Compton cross section	10
2.2	VCS reaction in CM frame	11
2.3	VCS Feynman diagrams	13
2.4	BH+B cross section	15
2.5	Definition of the GPs	17
3.1	Theoretical prediction for the generalized polarizabilities	27
3.2	HB χ PT calculation of $P^{(01,01)1}$	28
3.3	MAMI VCS experiment results	30
3.4	MAMI VCS experiment results 2	30
3.5	Bates, JLab and MAMI experimental results	32
3.6	SSA phase space	34
3.7	SSA DR model prediction for the VCS reaction	34
3.8	SSA sensitivity of the DR Model to the MAID multipoles	34
3.9	SSA for π^0 electroproduction	34
3.10	Experimental electric and magnetic GPs	35
4.1	MAMI accelerators	38
4.2	MAMI floor plan	38
4.3	3 spectrometer setup	39
4.4	Spectrometer detectors	42
4.5	Target	43
4.6	Focal plane proton polarimeter mounted in spectrometer A	44
4.7	Scattering of a proton by a ^{12}C nucleus	45
4.8	FPP coordinate systems	46
4.9	Møller polarimeter	46
4.10	Trigger logic	48
5.1	Precession of the spin components in the dipole case	51
5.2	QSPIN tracks for the proton precession	53
5.3	Reference frames	57
5.4	Parameterization with Euler angles	58
6.1	Parameterization of the analyzing power	61
6.2	Statistical errors and correlations for the polarization	62
6.3	Simulated BH+B polarizations	64
6.4	Simulated BH+B polarizations	65
6.5	Simulated matrix elements of the rotation matrix	68
6.6	Weighted mean of the theoretical BH+B polarization	69
6.7	Simulated polarizations with corrected P_y	69

7.1	Simulated phase space for VCS90 and VCS90b setups	72
7.2	Coincidence and m_{miss}^2	74
7.3	Particle identification	76
7.4	Target spectrum	77
7.5	Target wall events spectrum	77
7.6	Background spectrum	78
7.7	Real photon momentum experimental spectrum	78
7.8	Cross section VCS (April 05)	81
7.9	Cross section VCS (July 05)	81
7.10	Cross section VCSb (November05)	82
7.11	Rosenbluth separation: Mergell form factors	83
7.12	Rosenbluth separation: Friedrich-Walcher form factors	83
8.1	Analyzing power experiments	88
8.2	Analyzing power Fit	91
8.3	Focal plane variables Φ_s and Θ_s	94
8.4	Beam polarization	96
8.5	Proton polarization dependence from beam polarization	97
8.6	Experimental polarizations without constraint	99
8.7	Experimental polarizations with P_z^{CM} fixed	100
8.8	Experimental Polarizations with P_y^{CM} fixed	100
8.9	Effect of the polarizabilities on P_x	101
8.10	Effect of the polarizabilities on P_y	102
8.11	Effect of the polarizabilities on P_z	103
8.12	Effect of the structure functions on the polarizabilities	106
8.13	Likelihood for the P_{LT}^\perp fit	108
8.14	Polarization component P_x^{CM} with the fitted value of P_{LT}^\perp	110
A.1	Effect of different form factors on the BH+Born cross section	116
A.2	Form factor of the proton in different parameterizations	116
C.1	Unpolarized VCS kinematical coefficients	121
C.2	Angular evolution of the kinematical coefficients for M(h,x)	123
C.3	Angular evolution of the kinematical coefficients for M(h,y)	123
C.4	Angular evolution of the kinematical coefficients for M(h,z)	124

List of Tables

2.1	Generalized polarizabilities and EM transitions	18
3.1	Existing experimental results for the cross section measurements	31
4.1	Main parameters for the spectrometers A, B, and C	40
5.1	Variable values used for the spin matrix parameterization	54
7.1	Setups used for the VCS measurement. q_c is the central momentum of the spectrometer.	72
7.2	Cuts for the unpolarized cross section analysis	79
7.3	Rosenbluth separation results	85
8.1	Carbon analyzing power measurements	89
8.2	Elastic kinematics for the three new analyzing power measurements	89
8.3	Measured analyzing power in the three elastic setups.	90
8.4	Fit result for the analyzing power	90
8.5	Polarization analysis cuts	93
8.6	Double polarization observable for the non coincident background in the center of mass frame.	95
8.7	Mean proton polarization reconstructed with different values for the mean beam polarization.	97
8.8	Results for the proton polarizations	98
8.9	Generalized polarizabilities fit with three parameters	105
8.10	Structure function fit with three parameters	107
8.11	Extraction of P_{LT}^\perp	109
A.1	Constants resulting from the FW phenomenological parameterization fit	114
D.1	Cross section data: April 05 Beamtime	125
D.2	Cross section data: July 05 Beamtime	125
D.3	Cross section data: November 05 Beamtime	125
D.4	Rosenbluth separation data	126

Bibliography

- [1] R. Hofstadter, Rev. Mod. Phys. **28** (1956) 214
- [2] F.E. Low, Phys.Rev. **96**, 1428 (1954)
- [3] M. Gell-Mann, M. Goldberger, Phys.Rev. **96** (1954) 1433
- [4] A. Thomas, W. Weise, The Structure of the Nucleon, Wiley-VCH (2000)
- [5] Numerical Recipes in C, William H. Press, B. P. Flannery, S. A. Teukolsky, W. T. Vetterling, Cambridge University Press
- [6] J. Roche *et al.*, Phys. Rev. Lett. **85** (2000) 708-711
- [7] D. Drechsel *et al.*, Chiral Dynamics: Theory and Experiment, Proceedings, Mainz, Germany, 1997. Editors: A. Bernstein, D. Drechsel, Th. Walcher
- [8] M. Schumacher, Progr.Part and Nucl.Phys **55** (2005) 567-646
- [9] S. Ragusa, Phys.Rev.D **47** (1993) 3757
- [10] P.A.M. Guichon *et al.*, Nucl Phys A **591** (1995) 606-638
- [11] B. Pasquini *et al.*, Phys.Rev.C **63** (2001) 025205
- [12] P.A.M. Guichon, M. Vanderhaeghen, Prog.Part. and Nucl. Physics **41** (1998)
- [13] M Vanderhaeghen, Phys.Lett.B **402** (1997) 243
- [14] D. Drechsel *et al.*, Phys.Rev.C **55** (1997) 424
- [15] D. Drechsel *et al.*, Phys.Rev.C **57** (1998) 941
- [16] A. Metz, D. Drechsel, Z. der Physik **A356** (1996) 351
- [17] S.L. Adler, Phys.Rev. **139** B1638 (1965)
- [18] M.L. Goldberger, S.B. Treiman, Phys.Rev. **110**, 1178 (1958)
- [19] M.L. Goldberger, S.B. Treiman, Phys.Rev. **111**, 354 (1958)
- [20] M. Vanderhaeghen, Phys.Lett.**B368** (1996) 13
- [21] S. Scherer, Adv. Nucl. Phys. **27** (2003) 277
- [22] T.R. Hemmert *et al.* Phys. Rev. D **62** (2000) 014013
- [23] Kao *et al.*Phys.Rev.D **70** (2004) 114004
- [24] V. Bernard *et al.*, Nucl.Phys. **B338** (1992) 315
- [25] V. Bernard *et al.*, Phys.Lett. **B319** (1993) 269
- [26] B. Pasquini et al, Eur. Phys J. **11** (2001) 185-208
- [27] D. Drechsel *et al.*, Nucl. Phys. **A645** (1999) 145-174
(<http://www.kph.uni-mainz.de/MAID/maid.html>)

- [28] H. Arenhövel, D. Drechsel, Nucl.Phys. **A233** (1974) 153-163
- [29] A.J.F. Siegert, Phys.Rev. **52** (1937) 787-789
- [30] V. Olmos de Leon *et al.*, Eur.Phys.J.A **10** (2001) 207
- [31] Phys.Rev.Lett., **93** (2004) 122001
- [32] Submitted to Phys.Rev.Lett.; e-Print Archive: hep-ph/0312294
- [33] E.J. Brash, A. Kozlov, S. Li, G.M. Huber, Phys. Rev. C **65** (2002) 051001
- [34] P. Bourgeois *et al.*, Phys.Rev.Lett **97** (2006) 212001
- [35] C. Kao *et al.*, Phys.Rev. **D70** 114004 (2004) or: hep-ph/0408095
- [36] D. Djukanovic, private communication
- [37] P. Bartsch *et al.*, Phys.Rev.Lett 88 (2002) 142001, nucl-ex/0112009
- [38] D. Elsner *et al.*, Eur.Phys.J A27 (2006) 91, nucl-ex/0507014
- [39] I. Bensafa *et al.*, Eur. Phys. J. A 32, (2007) 69-75
- [40] R. Thompson *et al.*, Phys.Rev.Lett. **86**, (2001) 1702
- [41] L. Tiator *et al.*, nucl-th/0310041
- [42] G. Höhler *et al.* Nucl. Phys. **B114** (1976) 505-534
- [43] H. Herminghaus *et al.*, Nucl. Instr. and Meth. (1976) 138
- [44] K.I. Blomqvist *et al.*, Nucl. Instr. and Meth. A 403 (1998) 263-301
- [45] A. Jankowiak, EPJA, Vol. 28 Suppl. 1 (2006), 159
- [46] M. Korn, PhD Thesis, Mainz University (1994)
- [47] P. Bartsch, PhD Thesis, Mainz University (2001)
- [48] Th. Pospischil *et al.*, Nucl.Instr.and Meth. A **483** (2002) 713-725
- [49] Th. Pospischil, PhD Thesis, Mainz University (2000)
- [50] Th. Pospischil *et al.*, Nucl. Instr. and Meth. A **483** (2002) 726-733
- [51] P. Senger *et al.*, Nucl.Instr.Meth. **A 327**, (1993) 393
- [52] V. Bargmann, L. Michel, V.L. Telegdi: Phys.Rev.Lett **2** No.10 (1959) 435-437
- [53] J.D. Jackson, Classical Electrodynamics, John Wiley & Sons, Inc, 1962
- [54] L.T. Thomas, Phil. Mag. **3** 1. (1927)
- [55] G.C. Wick, Ann.Phys (N.Y.) **18**, (1962) 65
- [56] V.I. Ritus, Zh.Eksp.Teor.Fiz. **40**, (1961) 352 or Sov.Phys. JETP **13**, (1961) 240
- [57] V. Dmitrašinovic, Phys.Rev.C **47**, (1993) 2195-2203

-
- [58] M.W. McNaughton *et al.*, Nucl.Instr.and Meth. **241** (1985) 435-440
 - [59] G.V. Jover Mañas G. Jover, Diploma Thesis, Mainz University (2003)
 - [60] E. Aprile-Giboni *et al.*, Nucl.Instr.and Meth. **215** (1983) 147-156
 - [61] H. Fonvieille, private communication.
 - [62] M. Rosenbluth, Phys. Rev. **79** (1950) 615-619
 - [63] P. Janssens, private communication.
 - [64] P. Mergell *et al.*, Nucl.Phys. **A596** (1996) 367-396
 - [65] L. Lyons, Statistics for Nuclear and Particle Physicists, Cambridge University Press (1986)
 - [66] Y.S. Tsai, Phys.Rev. **122** (1961) 1898
 - [67] J.M. Friedrich, PhD Thesis, Mainz University, (2000)
 - [68] W. Heitler, The Quantum Theory of Radiation , Oxford University Press, London, 1954
 - [69] L.W. Mo, Y.S. Tsai, Rev.Mod.Phys **41** 193-205 (1969)
 - [70] Y.S. Tsai, SLAC-PUB-848 Radiative Corrections to Electron Scattering (1971)
 - [71] B.E. Poling *et al.* , The Properties if Gases and Liquids, 4th edition, McGraw-Hill, New York, 1987
 - [72] J. Friedrich and Th. Walcher, Eur. Phys. J. A **17** (2003) 607-623
 - [73] P. Janssens, PhD Thesis, University of Gent, Belgium (2007)
 - [74] S.L. Meyer, Data Analysis for Scientists and Engineers (1992), ISBN 0-9635027-0-0